RADIATIVE TRANSFER MODELLING AND OBSERVATIONS OF CLUMPY, DUSTY ASTROPHYSICAL ENVIRONMENTS

Dissertation

in fulfilment of the requirements for a Doctoral degree
of the Faculty of Mathematics and Natural Sciences
at Kiel University

submitted by

PETER SCICLUNA

Kiel, 2015

First referee: Prof. Dr. S. Wolf
Second referee: Prof. Dr. B. Heber

Date of the oral exaimination: 17.09.2015
Approved for publication: 17.09.2015

Signed Prof. Dr. Wolfgang J. Duschl, Dean

When you're thinking about something you don't understand, you have the very terrible, uncomfortable feeling called confusion; it's a very difficult and unhappy business. So most of the time you're rather unhappy actually with this confusion – you can't penetrate this thing. The confusion (comes) because we're all some kind of apes trying to put two sticks together – trying to reach the banana. And we can't quite make it – the idea. I get this feeling all the time. So, I always feel stupid. But every once in a while, the two sticks go together and I can reach the banana.

— Richard P. Feynman

ABSTRACT

This thesis explores selected aspects of cosmic dust through a series of case studies of different dusty environments, in particular those where the dust distribution is clumpy.

Cosmic dust plays a key role in a number of physical processes: it allows stars to lose mass, adding heavy elements to the interstellar medium; it helps regulate the formation of sun–like stars; it allows the formation of complex molecules in space; and perhaps most importantly of all, it gets turned into planets, plants, and even people. However, it must be studied indirectly, through the detection of stellar photons that have interacted with interstellar dust, or by observing photons emitted by dust which is heated by stars. As a result, it is crucial to understand the interactions of photons with dust, and their propagation through dusty environments; this necessitates radiative transfer modelling.

This thesis explores the influence of the geometrical distribution of dust on observations of the extinction of starlight by dust, which is one of the main methods for constraining the properties of dust. Modelling work shows that geometrical effects in clumpy environments compromise efforts to constrain dust properties in embedded or extragalactic environments, but that diffuse interstellar extinction measurements are unaffected.

It also considers the possibility that stars in a clumpy molecular cloud might interact with the dense clumps, which is found to be a surprisingly probable occurrence. This is shown to result in the possible accretion of a sufficient supply of material to form a protoplanetary disc, opening the possibility of a second epoch of planet formation, with a diverse range of potential consequences for young planetary systems.

Results of simultaneous modelling of both components of the binary young–stellar–object VV Corona Australis are presented, which show that both discs have similar inclinations, but rather large scale heights. Based on the model results, an age of 3.5 Myr is derived for the system, and stellar masses of $1.7\,M_\odot$; in combination with near–infrared spectroscopy, this suggests an accretion rate of $4 \times 10^{-8}\,M_\odot\,yr^{-1}$ for the primary.

Finally, the results of a high–contrast imaging and polarimetric study of the dusty mass–loss envelope of the nearby extreme red supergiant VY Canis Majoris are presented, along with a new radiative transfer model of the envelope. The radiative transfer model reveals the presence of at least $6 \times 10^{-3}\,M_\odot$ of dust, implying that the star has ejected at least $1\,M_\odot$ in the last 1000 yr. Polarimetric imaging reveals the presence of dust grains ~ 50 times larger than dust in the interstellar medium; grains of this size are likely to survive the eventual supernova of VY CMa provided it does not occur within the next 5000–10000 yr. This suggests that pre–supernova mass loss can make a significant contribution to the dust content of galaxies in the early universe.

ZUSAMMENFASSUNG

In dieser Dissertation werden ausgewählte Aspekte kosmischen Staubs aus einer Vielzahl klumpiger Staubverteilungen untersucht, unter Zuhilfenahme mehrerer Fallstudien.

Kosmischer Staub spielt eine wichtige Rolle in einer Reihe von physikalischen Prozessen: Er ermöglicht Sternen durch Abgabe schwerer Elemente an das interstellare Medium Masse zu verlieren, er hilft, durch Regulierung, bei der Entstehung sonnenähnlicher Sterne, er ermöglicht die Bildung von komplexen Molekülen im All aber vor allem ist er die Grundlage der Entstehung von Planeten, Pflanzen und sogar Menschen. Allerdings kann Staub nicht direkt untersucht werden. Ein Nachweis ist durch stellare Photonen möglich, welche mit interstellaren Staub interagiert haben oder auch durch thermische Strahlung von Staub, der durch den Stern aufgeheizt wurde. Infolgedessen ist es wichtig die Wechselwirkungen von Photonen mit Staub und deren Ausbreitung in staubigen Umgebungen zu verstehen. Zu diesem Zweck wird Strahlungstransportmodellierung angewendet.

Diese Arbeit untersucht den Einfluss geometrischer Verteilungen von Staub auf Beobachtungen von Staubextinktion von Sternenlicht. Dies ist eine der wichtigsten Methoden für die Bestimmung von Staubeigenschaften. Die Ergebnisse der Modellierungen zeigen, dass geometrische Effekte in klumpigen Umgebungen das Bestimmen von Staubeigenschaften in eingebetteten oder extragalaktischen Umgebungen unmöglich machen. Diffuse interstellare Extinktionsmessungen sind davon allerdings nicht betroffen.

Weiterhin wird die Möglichkeit untersucht, dass Sterne, welche in einer klumpigen Molekühlwolke eingebettet sind, mit sehr dichten Klumpen wechselwirken könnten. Dabei finden diese Wechselwirkungen überraschend häufig statt. Dies kann durch Akkretion ausreichender Masse zur Bildung einer protoplanetaren Scheibe führen. Falls dadurch eine zweite Planetenenstehungsepoche ausgelöst wird, ergäben sich vielfältige mögliche Konsequenzen für das junge Planetensystem.

Die Ergebnisse der gleichzeitigen Modellierung beider Komponenten des jungen Binärsterns VV Corona Australis werden vorgestellt. Diese zeigen, dass beide Scheiben eine ähnlich kleine Inklination und große Skalenhöhen besitzen. Aus der Modellierung ergibt sich ein Alter des Systems von 3,5 Myr und jeweils eine Sternenmasse von $1{,}7\,M_\odot$. Zusammen mit den Ergebnissen der Nah-Infrarot-Spektroskopie kann auf eine Akkretionsrate von $4 \times 10^{-8}\,M_\odot\,yr^{-1}$ für die primäre Komponente geschlossen werden.

Schließlich werden die Ergebnisse einer Hochkontrastaufnahme und polarimetrischen Untersuchung der staubigen Massenverlustshülle des nahen roten überriesen VY Canis Majoris vorgestellt. Ebenfall wird ein neues Strahlungstransportmodell für die staubige Massenverlustshülle vorgestellt. Dieses zeigt, dass das System mindestens $6 \times 10^{-3}\,M_\odot$ Staub beinhaltet. Um diese Menge zu erreichen, muss der Stern in den letzten 1000 Jahren mindestens $1\,M_\odot$ Material ausgeworfen haben. Polarimetrische Beobachtungen offenbaren das Vorhandensein von Staubkörnern, welche $\sim$ 50-mal größer sind als Staub im interstellaren Medium. Körner dieser Größe könnten wahrschein-

lich eine Supernova von VY CMa überleben, sofern diese nicht innerhalb der nächsten 5000-10000 Jahren ausgelöst wird. Dies deutet darauf hin, dass Massenverlust von Überriesen vor ihrer Supernova einen wesentlichen Beitrag zum Staubgehalt in Galaxien des frühen Universums liefern kann.

CONTENTS

LIST OF FIGURES

LIST OF TABLES

ACRONYMS

AGB Asymptotic Giant Branch

ALMA Atacama Large Millimetre/sub-millimetre Array

AO Adaptive Optics

CASA Common Astronomy Software Applications

CI Classical Imaging

CSM Circumstellar Medium

DIT Detector Integration Time

ESO European Southern Observatory

IDL Interactive Data Language

IMF Initial Mass Function

IRDIS InfraRed Dual-band Imager & Spectrograph

ISM Interstellar Medium

MIDI MID-infrared Interferometer

PSF Point-Spread function

RGB Red Giant Branch

RSG Red Supergiant

SED Spectral Energy Distribution

SMA Sub-Millimetre Array

SPHERE Spectro-Polarimetric High-contrast Exoplanet REsearch

UT Unit Telescope

VLT Very Large Telescope

VLTI Very Large Telescope Interferometer

XAO eXtreme Adaptive Optics

ZIMPOL Zurich IMaging POLarimeter

1 INTRODUCTION

A light–hearted beginning.

"Our bodies are made of star-stuff"
– Albert Durrant Watson
"You are all stardust."
– Lawrence M. Krauss

Mankind has always asked the question *'Where did we come from?'* The search for our origins has spawned a multitude of scientific[1] fields, posing questions which have fascinated humanity along the way.

In many senses, the question of origin is one of the fundamental problems of modern astronomy, and is that which drives our need to explore cosmology, stellar evolution, and the formation of stars and planets. Our current scientific paradigm typically recasts the question in terms like *'Given that the universe originally contained only hydrogen and helium[2], how did the stuff we're made of get here?'*, then leaves the details to biologists.

We know that stars derive their energy from nuclear fusion in their cores, and hence must be the source of the heavy elements that make up the planet Earth and its population. But how did this material get from the cores of stars to our corner of the universe?

The answer lies in the life-cycle of stars and dust; evolved stars eject large amounts of material, including dust, into space near the ends of their lives, which floats around space for some time before being incorporated into a new generation of stars and planets, and eventually returned to the interstellar medium again. The continual stirring of the interstellar medium by supernovae ensures that material is well mixed, and generates the turbulence that triggers the next round of star formation.

Dust plays a number of key roles in the development of life. By allowing interstellar gas to cool, it promotes the formation of Sun–like stars, whose planets are able to host life. At the same time, by providing a surface on which chemical reaction can take place, it provides pathways for the formation of pre-biotic molecules that may eventually form lifeforms; the carbon in our bodies either comes from or has interacted with cosmic dust. Planets themselves form from dust, as it accumulates and agglomerates into earth–sized bodies in young solar systems. That dust, and all the other elements that are required for life, was released into the interstellar medium by red giants and supernovae, but must survive in interstellar space to be incorporated into the clouds that forms stars. The question of origin is, therefore, really a question of the origin and evolution of cosmic dust.

1 and not-so scientific
2 well, more or less

However, because space is so vast, it is impossible to directly study dust grains outside our solar system. Therefore, we must rely on indirect methods to study interstellar dust. This is most often done by studying the light absorbed, emitted or scattered by interstellar dust to determine its properties, and is intimately tied up with our ability to accurately model the interactions of dust with light. From this, we have been able to learn about the size, shape, and composition of dust in a variety of environments, from the mass-loss envelopes and planet-forming discs of nearby stars to the interstellar medium of distant galaxies in the early universe. Nevertheless, a multitude of questions remain.

This thesis aims to contribute to the field by presenting a series of case studies related to dusty environments in the local universe, both from a theoretical and an observational perspective. These studies cover a number of topics concerning star formation, evolved stars, and the interstellar medium.

Firstly, some relevant background material concerning astrophysical dust and modelling techniques is presented in chapter 2. This reveiws the properties that govern the interactions between dust and light, and introduces the techniques used to model these interactions in later chapters. It then reveiws the important literature concerning the properties of interstellar dust, its importance to the star-formation process and its formation in the envelopes of evolved stars.

Next, chapter 3 presents the results of detailed studies on the wavelength dependence of the extinction of starlight in clumpy inter- and circumstellar media. This aims to explore potential systematic effects related to scattering by dust grains and their influence on extinction, which is one of the key ways in which we learn about dust. We show that, while these effects are important for galactic studies of young or evolved stars or for extragalactic sources, they present no barrier to understanding dust in the local interstellar medium.

This thesis then presents two studies in star and planet formation, where dust plays a key role. Chapter 4 applies numerical models to investigate the role of late-time accretion as a mechanism to re-form a circumstellar disc to explain observations of "old" young stars. As well as explaining the numbers of observed stars, this mechanism may present a second chance for planet formation or have a significant impact on the evolution of an existing planetary system. Thereafter, chapter 5 applies numerical radiative transfer techniques to aid in interpreting photometric and high-resolution interferometric observations of the enigmatic binary young-stellar object VV Corona Australis. Comparison to a large grid of models allows an exploration of the properties of the central stars and their discs, constraining the evolutionary state of the system. This also allows for the determination of a series of targeted observational priorities that will allow future modelling attempts to include further physical effects.

Then, chapter 6 explores the interpretation of high-contrast imaging & polarimetic observations of the inhomogeneous mass-loss envelope of the extreme red supergiant VY Canis Majoris. New observations from the novel extreme adaptive optics imager SPHERE provide the most detailed view of the envelope to date, and demonstrate that it is possible to derive the size of dust grains in similar environments from these observations. Three-dimensional radiative transfer modelling is used to reproduce the emission of the envelope, placing the most robust constraints on the dust mass to

date. Based on these results, the possible appearance of the eventual supernova and the fate of the dust in the envelope is evaluated.

Finally, chapter 7 summarises the conclusions of this work, followed by an outlook for future studies of cosmic dust. Targets for the multitude of new and upcoming astronomical instruments are highlighted, along with the most pressing concerns for future modelling efforts.

2

DUST IN ASTRONOMY

Although dust makes up only a tiny portion of the mass of the universe[1]*, dust dominates the heating and cooling of interstellar matter, as it is highly efficient in absorbing the ultraviolet, optical and near-infrared radiation emitted by stars, which it then re-radiates in the mid- and far-infrared.*

This interstellar dust plays a key role in the formation of stars and planets, but is itself produced by stars as they approach the end of their lives, once again playing a critical role by driving mass-loss processes. However, by absorbing and scattering photons emitted by stars, dust interferes with our ability to observe these processes, meaning that images and spectra taken of dust-dominated environments require careful interpretation, often with the aid of radiative transfer modelling.

This chapter gives an introduction to astrophysical dust and its interactions with light (2.1), how this is used in radiative transfer modelling (2.2) along with a brief overview of the stellar life-cycle, focussing on the role of dust in stellar astrophysics and its effect on astronomical observations (2.3).

2.1 THE INTERACTION BETWEEN LIGHT AND DUST

This section briefly discusses the properties of dust, providing the information necessary to understand how dust affects astronomical observations and stellar evolution (2.3) and the required inputs for radiative transfer modelling (2.2). This discussion is primarily based on the excellent review by Krügel (2008), which the interested reader is encouraged to peruse. A large quantity of material must be of necessity reduced to its most salient points, and derivations abbreviated to their results and consequences; further details can also be found in the literature, for example Voshchinnikov (2004). Throughout this section, it is assumed that dust grains are compact, homogeneous spheres unless otherwise indicated; results for other cases may be found in the aforementioned reviews.

2.1.1 *Dust cross-sections*

The probability of interaction between a photon and a dust grain can be described in terms of the grain's *cross-sections*. In these interactions, the photon may be *scattered*, in which only the direction of the photon changes, or the photon may be *absorbed*, in which case its energy is added to the internal energy of the grain – under equilibrium conditions, the grain will quickly emit this energy in the form of new photons, such that we may consider (absorption + re-emission) as a single interaction in which the frequency of the radiation has changed, the importance of which will become clear in section 2.2.

1 Of the matter in the interstellar medium, no more than 1% of it is in the form of dust, while the interstellar medium makes up only a small portion of the baryonic matter in our Galaxy.

To define the cross-sections, we begin by considering the scattering of a plan monochromatic wave with frequency ν (or wavelength λ) and flux F_0 by a single dust grain. The distribution of the scattered flux $F(\theta, \phi)$ must depend some properties of the grain which we will encapsulate with $L(\theta, \phi)$, along with F_0/r^2, where r is the distance between the observer and the particle, such that

$$F(\theta, \phi) = \frac{F_0}{k^2 r^2} L(\theta, \phi) \tag{1}$$

where $k = 2\pi/\lambda$ is the wavenumber of the wave, introduced to ensure that L is dimensionless.

We now define the scattering cross-section C^{sca} such that

$$\int F(\theta, \phi)\, d\Omega = F_0 C^{sca}$$

, i.e. $F_0 C^{sca}$ is the total energy scattered into all directions per unit time, which gives

$$C^{sca} = \frac{1}{k^2} \int_0^{2\pi} d\phi \int_0^{\pi} L(\theta, \phi) \sin\theta d\theta, \tag{2}$$

resulting in the dimension of length squared.

Similarly, the absorption cross-section C^{abs} is defined such that $F_0 C^{abs}$ is the total energy absorbed by the particle per unit time. As energy is removed from the incoming wave *either* by absorption or by scattering, the total cross-section for attenuation (referred to by astronomers as *extinction*) is evidently $C^{ext} = C^{sca} + C^{abs}$. This determines the total amount of energy removed from the incoming wave.

It is also usual to define the *albedo* as the fraction of energy removed from the wave by scattering i.e.

$$A = \frac{C^{sca}}{C^{ext}}. \tag{3}$$

Based on the cross-section of a single particle, it is sometimes useful to define several other quantities, which may be a more appropriate way of measuring the interaction probability. If C is the cross-section of a single particle, it is common to define the *efficiency* $Q = C/(\pi a^2)$ where a is the particle radius. Hence, the efficiency is the ratio of the actual cross-section to the geometrical cross-section, and applies similarly to extinction, scattering and absorption.

In some cases, the *volume coefficient* or cross-section per unit volume is more useful, and is defined $K = C n_d$, where n_d is the number density of dust grains. Similarly, the *mass coefficient* is the cross-section per unit mass of dust, $\kappa = C n_d \left(\rho_d \frac{4}{3}\pi a^3\right)$, where ρ_d is the mass density of a single grain.

2.1.2 *The angular dependence of scattering*

In the previous section, $L(\theta, \phi)$ was introduced to describe the angular dependence of scattered radiation. We now define a $\tilde{\Phi}(\theta, \phi)$ as $L(\theta, \phi)$ normalised such that

$$\int_{4\pi} \tilde{\Phi}(\theta, \phi)\, d\Omega = 4\pi, \tag{4}$$

which we call the phase function. This phase function now encapsulates the probability density function (p.d.f.) of the new directions of scattered photons.

For spherical grains, the dependence of the phase function on ϕ drops out due to the rotational symmetry of the scenario, and we take this opportunity to re-cast $\tilde{\Phi}$ as a function of $\cos\theta$ to create $\Phi(\cos\theta)$ normalised such that

$$\frac{1}{2}\int_{-1}^{+1} \Phi(\cos\theta)\, \mathrm{d}\cos\theta = 1, \tag{5}$$

which we will also call the phase function.

Sometimes one wishes to parametrise the *degree* of the anisotropy of the scattered radiation with a single number. If is common to use the *asymmetry factor* g, which is defined as the expectation value of the cosine of the scattering angle

$$g = \langle\cos\theta\rangle = \frac{1}{2}\int_{-1}^{+1} \Phi(\cos\theta)\cos\theta \mathrm{d}\cos\theta. \tag{6}$$

Grains which primarily scatter forwards have positive g-factors, with the extreme case of $g = 1$ meaning that scattered photons do not in fact change direction. Conversely, negative g-factors indicates backward scattering, with $g = -1$ indicating pure reflection. However, while isotropic scattering has $g = 0$, it is not necessary that $g = 0$ indicates isotropic scattering, as any phase function that is symmetric with respect to $\cos\theta = 0$ will have an expectation of 0, e.g. that of Rayleigh scattering.

2.1.3 *Polarisation*

As a transverse wave, electromagnetic radiation is *polarisible*; that is, the electric field can be made to oscillate coherently in a preferred plane or rotate with a particular frequency and chirality. When the electric field has a preferred plane, the wave is described as *linearly polarised*, while rotating waves are *circularly polarised*; the superposition of these two effects produces *elliptical polarisation*. The strength of the preference is quantified by the *degree of polarisation* p; when the electic fields of all waves oscillate in the same direction, $p = 100\%$. For convenience, the degree of linear polarisation p_l and the degree of circular polarisation p_c are usually distinguished. For linear polarisation, the preferred plane is characterised by the *polarisation angle* γ, measured relative to some reference direction, while the chirality of circular polarisation is indicated by the sign of p_c.

THE STOKES FORMALISM As astronomers can generally only measure the flux, and not the amplitude, of incoming light, it is common to describe the polarisation state of light relative to a particular reference frame through the *Stokes vector* $\vec{S}$, which consists of the Stokes parameters I, Q, U and V. I measures the total intensity of the light, Q and U measure the intensity in linear polarisation in directions parallel to and at 45° from the reference direction respectively, while V measures the sense and intensity of circular polarisation.

From these four parameters, the degrees and angles of polarisation given above can be computed as follows

$$p_l = \frac{\sqrt{Q^2 + U^2}}{I^2}, \tag{7}$$

$$\gamma = \frac{1}{2}\tan^{-1}\left(\frac{U}{Q}\right), \tag{8}$$

$$p_c = \frac{V}{I}. \tag{9}$$

POLARISATION BY SCATTERING AND THE MÜLLER MATRIX The electric field of a photon being scattered by a dust grain is deformed, resulting in polarisation. This process is typically described using Müller calculus, in which the outgoing Stokes vector is calculated by multiplying the incoming Stokes vector with the Müller matrix M

$$\vec{S}' = M(\theta, \phi) \times \vec{S}. \tag{10}$$

In the case of scattering by spherical grains, the dependence of M on ϕ disappears and many of the components of M vanish, leaving only four different values

$$\begin{pmatrix} I' \\ Q' \\ U' \\ V' \end{pmatrix} = \frac{1}{k^2 r^2} \begin{pmatrix} M_{11} & M_{12} & 0 & 0 \\ M_{12} & M_{11} & 0 & 0 \\ 0 & 0 & M_{33} & M_{34} \\ 0 & 0 & -M_{34} & M_{33} \end{pmatrix} \begin{pmatrix} I \\ Q \\ U \\ V \end{pmatrix}, \tag{11}$$

where the dependence $M_{ij}(\theta)$ has been omitted for clarity. It should immediately be clear that if the incoming ray is unpolarised ($Q = U = V = 0$) then the polarisation state of $\vec{S}'$ depends only on M_{11} and M_{12}. Indeed, the degree of linear polarisation can be calculated directly from

$$p_l = \left|\frac{M_{12}}{M_{11}}\right|. \tag{12}$$

The reader should also note that $M_{11}(\theta)$ is identical to the scattering phase function $\tilde{\Phi}(\theta)$ defined above. The polarisation angle is usually perpendicular to the scattering plane (the plane between the incoming and outgoing rays) except in the case of very large particles, where it may switch to be parallel to the scattering plane.

2.1.4 *Radiation pressure*

Special relativity shows that photons carry momentum $p = E/c$ as well as energy, and hence when a photon interacts with a dust grain there must be some transfer of momentum from photon to grain.

In the case of absorption, the entire momentum of the photon must be deposited in the grain. However, the grain will soon isotropically emit photons with the same total momentum, so the absorption only causes a net change in the momentum of the grain if the radiation field heating the grain is anisotropic – otherwise the momenta of the absorbed and emitted photons cancel. For maximally anisotropic (plane-parallel) illumination, this leads to the well-known result that on average, each photon deposits its entire momentum.

For scattering, on the other hand, the anisotropy of the outgoing photons also plays a role. Hence, each photon on average contributes momentum $p(1-g)$; typical interstellar dust grains are efficient forward scatterers, and the momentum imparted by scattered photons is therefore only a fraction of that incident upon the grain.

2.1.5 *Calculating dust properties*

Having described the key properties of dust relevant to astronomical observations, this information can now be used in two ways. Firstly, one may wish to use astronomical observations to learn something about interstellar dust. Secondly, one might seek to clarify the influence of dust on observations of other astronomical objects in order to improve their interpretation. In both cases, it is important to *model* the dust, to produce quantities that can be successfully compared. In order to do so, one needs a means to calculate the dust cross-sections, Müller matrix, etc.

The basis of such calculations are measurements of the bulk optical properties of the materials to be used. These are usually referred to as *optical constants*[2], in the form of dielectic functions $(\epsilon_1(\lambda), \epsilon_2(\lambda))$ or the complex refractive index $m = n + ik$. Throughout this thesis, refractive indices are preferred to dielectric functions.

Having chosen a set of optical constants, one must choose a method by which to calculate the properties of one's dust model. Arguably the simplest method is Mie calculus (Mie, 1908), which calculates the interactions of a homogeneous sphere of radius a with radiation to derive the cross-sections and Müller matrix. This is the preferred method in this thesis, and the key inputs are the optical constants and the *size parameter*

$$x = \frac{2\pi a}{\lambda}, \tag{13}$$

where λ is the wavelength for which the calculations are to be performed. Because a single grain will typically exhibit a number of resonances covering very small wavelength ranges, it is common to calculate a distribution of sizes to smooth these out.

Although a number of other methods exist (e.g. the Discrete Dipole Approximation, DeVoe 1964; a Distribution of Hollow Spheres, Bohren and Huffman 1983), Mie calculus is preferred here due to its simplicity and widespread use. For a thorough exploration of different methods for modelling dust, the interested reader should refer to Bohren and Huffman (1983).

2.2 RADIATIVE TRANSFER

Astronomical observations depend on the collection of photons from distant sources – in effect, it is extremely-remote sensing. As such, in order to correctly interpret observations, understanding the propagation of photons through the intervening material is essential (Krügel, 2008). As such a complex problem is inherently non-linear, computational solutions are often required; this enables thorough investigations of radiative transfer effects, the role of optical depth and scattering on observations (Krügel, 2008). Astrophysical dust is particularly problematic as, as discussed in the previous chapter, it effectively absorbs starlight and re-emits it in the infrared, as well

2 which are, in fact, wavelength dependent

as scattering and polarising the radiation. The techniques described in this chapter are tailored to dusty radiative transfer, but much of the formalism is the same when one wishes to explore the balance of photo-ionisation or gas heating.

2.2.1 *The equations of radiative transfer*

Interstellar dust attenuates and intensifies light rays propagating through it. Attenuation is caused by *extinction* of the ray, that is the absorption or scattering of photons, removing them from the ray; meanwhile, the additional intensity is contributed by thermal emission or the scattering of photons from other directions into the direction of the ray.

Hence, if a ray with incident intensity I_ν travels a distance ds, its intensity is modified such that

$$\frac{dI_\nu}{ds} = -K_\nu^{ext} I_\nu + \epsilon_\nu, \tag{14}$$

where K_ν^{ext} is the extinction cross-section per unit volume at frequency ν and ϵ_ν is the *source term*; that is, the additional intensity contributed by emission or scattering. For dust at temperature T and scattering from incoming rays $\tilde{I}_\nu$ the source term is given by

$$\epsilon_\nu = K_\nu^{abs} B_\nu(T) + \frac{K_\nu^{sca}}{4\pi} \int_{4\pi} \Phi_\nu(\alpha)\, \tilde{I}_\nu \, d\Omega, \tag{15}$$

where $B_\nu(T)$ is the Planck function at temperature T, α is the angle between I and $\tilde{I}$, Φ is the scattering phase function of the dust, and the integral is performed over 4π steradians of solid angle.

It is often more helpful to recast these equations in terms of a dimensionless property telling us something about the optical properties of the medium. Hence we define the *optical depth*

$$\tau_\nu = \int K_\nu \, ds = \int n_d C_\nu \, ds \tag{16}$$

where τ might be $\tau^{ext,abs,sca}$ for extinction, absorption or scattering respectively[3], C_ν is the cross-section of a single dust grain and n_d is the number density of dust grains. The reader should note that, as shown by the final part of Eq. 16, $\tau = s/\langle l \rangle$, i.e. the ratio of the path-length to the mean-free path.

Now, by defining the *source function* $S_\nu = \epsilon_\nu / K_\nu^{ext}$ we can re-write Eq. 14 as

$$\frac{dI_\nu}{d\tau_\nu} = -I_\nu + S_\nu, \tag{17}$$

from which we can see that the balance between I and S tells us whether the intensity increases or decreases with increasing optical depth.

The primary objective of radiative-transfer modelling is to solve equation 17 using numerical methods to determine I_ν and S_ν at all points in the model. The solution can then be used to calculate interesting properties for comparison to astronomical observations, such as images, spectral energy distributions, or polarisation states.

3 where τ is given without qualification, the reader can assume that it refers to the extinction optical depth unless stated otherwise.

2.2.2 *Monte Carlo methods*

The above equations can be solved in a number of different ways, depending on the problem to be solved (Krügel, 2008). Sometimes, the problem can be solved analytically, and an iterative solution of the coupling between the radiation field and dust temperatures can be performed (Krügel, 2008). However, in many cases, such as when the problem lacks simple symmetry, analytical methods are unable to reach a solution (Krügel, 2008), necessitating a numerical solution. However, the studies in later chapters concern intrinsically three–dimensional problems, such as inhomogeneous dust clouds, and must correctly account for anisotropic scattering; in problems with more than 1 dimension, direct numerical integration of equation 17 becomes both exceedingly complex and prohibitively expensive.

In such situations, the method of choice is a probabilistic one (Krügel, 2008). So-called "Monte Carlo" solutions exploit the proliferation of computational power over recent decades, and the availability of CPU cycles and the skill of the programmer in control of them are the only restrictions on its ability to solve complex radiative-transfer problems (Whitney, 2011). Monte Carlo methods – which draw their name from the connection between the Principality of Monaco and gambling – have been exploited in a wide range of fields.They rely on sampling randomly from the probability distribution functions of the underlying variables of the system and propagating them through the equations that govern the system to explore the distribution of outcomes. In essence, the method exploits the fact that, if a quantity x is drawn from a distribution X, then the distribution of the values of $f(x)$ can be approximated by repeatedly drawing values from X, and performing the operation $f(x)$ upon every value in the sample. Their strength lies in their flexibility; once an algorithm has been defined to attack a particular class of problems, it does not usually need to be adapted to solve other, similar problems – in the case of radiative transfer, this means that an algorithm that solves one 3 dimensional problem can solve any 3 dimensional problem based upon the same physics, without regard for the details of the geometry, and usually the only difference between 1D and 3D Monte Carlo codes is the definition of the spatial grid. Furthermore, it will always arrive at a solution[4], and its runtime can be controlled by limiting the number of samples – albeit at the expense of precision (Whitney, 2011). Indeed, a great variety of complex physical problems have been investigated using these methods (e.g. Wolf et al., 1999; Ercolano et al., 2003; Indebetouw et al., 2006; Woitke, 2006; de Looze et al., 2012; Heymann and Siebenmorgen, 2012), even those that couple radiative transfer with a multitude of other physical effects (Harries, 2015).

The basis of Monte Carlo radiative transfer is the random sampling of the properties of the radiation field and its interactions with matter (Whitney, 2011). By breaking the radiation field into monochromatic radiation packets (commonly referred to as "photons") and following their interactions with matter distributed on a grid (in effect a random walk), then for a statistically significant set of photons we arrive at a self-consistent solution to the problem in question.

For each source of radiation (with luminosity L), some number N photons are randomly generated with fixed energy $\varepsilon = L\Delta t/N$ – their direction is determined

4 Although this does not prevent the solution from being unphysical; the caveat "Garbage in, garbage out" applies.

by two uniform random numbers $\xi_i \in [0, 1)$, where the index i indicates the ith random number. To ensure that the random directions are uniformly distributed in 3 dimensions, the direction must be chosen from the probabiltiy distribution $P(\Omega)\,d\Omega = P(\cos\theta, \phi)\,d\cos\theta d\phi$. This implies that the z-component of the photon's direction must be sampled uniformly in $\cos\theta$ i.e. $z = \cos\theta = 2\xi_1 - 1$, and the azimuth of the photon's direction is determined $\phi = 2\pi\xi_2$ and then converted to provide x–y coordinates from $x = \sin\theta\cos\phi$ and $y = \sin\theta\sin\phi$.

The photon then propagates in this direction until an interaction occurs. The optical depth that the photon must travel to reach the next interaction is calculated from $\tau = -\ln\xi_i$, as eq.17 implies that $P(\tau)\,d\tau = e^{-\tau}d\tau$ (Whitney, 2011). This can then be converted to a physical path-length s using the number density of the ith cell n_i and cross-sections C_ν of the intervening medium using $s = \tau/n_i C_\nu$. The interaction may be either an absorption or a scattering event, determined using a random number and the albedo; if $\xi_i \leqslant C_\nu^{sca}/C_\nu^{ext}$ then the interaction is scattering.

In this case, only the direction of the photon changes; in the case of isotropic scattering, the same algorithm is used to choose a new direction as was used to choose the initial direction of the photon. Otherwise, the new direction must be sampled directly from the scattering phase function $\Phi(\theta)$, either by using the phase-function derived from Mie calculus (Mie, 1908) or using an approximation such as the Henyey-Greenstein function (Henyey and Greenstein, 1941). If one is interested in calculating polarisation, then the Stokes vector of the photon must also be updated at each scattering event using Eq. 11.

On the other hand, if an absorption occurs, the internal energy of the cell U_i is increased by ε, and the photon is re-emitted with a new direction determined in the same manner as the initial direction and a new wavelength chosen as follows. First the temperature of the dust in the cell must be determined using

$$\int C_\nu^{abs} B_\nu(T)\,d\nu = \frac{U_i}{4\pi n_i V_i}, \tag{18}$$

where V_i is the volume of the cell. The photon is then re-emitted with the lowest frequency ν' for which

$$\int_0^{\nu'} C_\nu^{abs} \frac{dB_\nu}{dT}\,d\nu \geqslant \xi \int_0^{\infty} C_\nu^{abs} \frac{dB_\nu}{dT}\,d\nu. \tag{19}$$

based on the method of Bjorkman and Wood (2001). Alternatively, the internal energy may be sampled using the path-lengths of all photons crossing the cell, as described by Lucy (1999). The internal energy is then sampled using

$$U_i = \frac{\varepsilon}{\Delta t} \sum C_\nu^{abs} l. \tag{20}$$

Because this method of estimating the absorption rate uses information from *every* photon crossing a cell, rather than just those that are absorbed in the cell, it results in a much more robust estimate of the internal energy of the cell, and hence the dust temperature. Alternatively, the same statistical significance can be achieved with significantly fewer photons, and hence shorter run-time.

After numerous interactions, the photons leave the model, and the frequency distribution of the emergent packets can be converted into a spectrum of the emergent

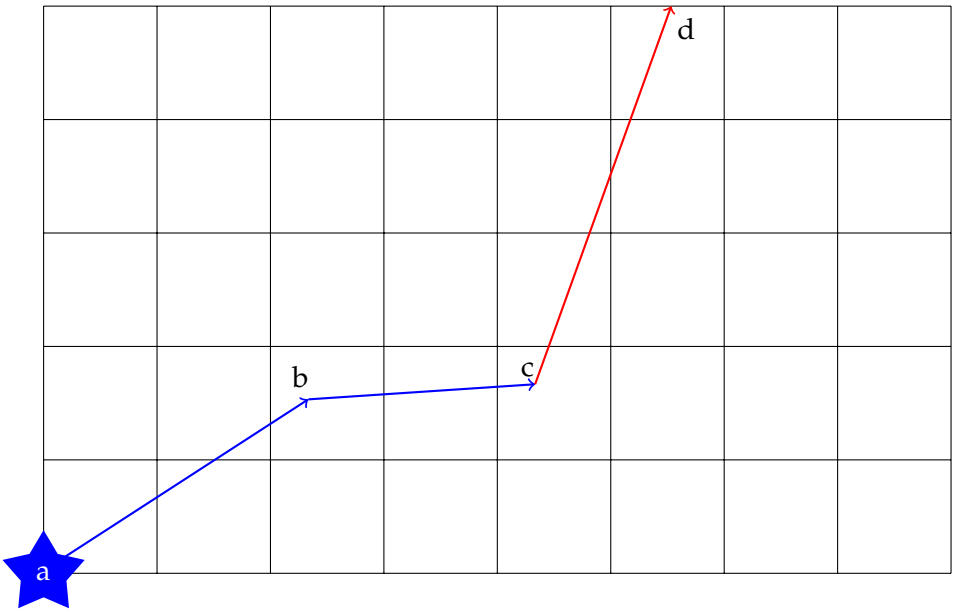

Figure 1: A schematic showing the way in which a Monte Carlo photon interacts with the dust, updating the properties of the grid as it goes. At *a*, the photon is emitted from the source, with its frequency determined by the properties of the source. The photon proceeds in its initial direction until *b*, where it is scattered onto a new path. At *c*, the photon is absorbed, increasing the internal energy of the dust in the cell. The photon is then re-emitted at a longer wavelength with a new direction. Finally, at *d* it escapes the grid.

radiation field for comparison to observations. Alternatively, the final directions of individual photons can be projected onto a grid of pixels to produce images, although the number of photons required to do so is prohibitive for realistic observations.

It is therefore common to exploit *ray tracing*, where Eq. 17 is solved along a series of parallel[5] rays projected through the model grid, with each ray corresponding to a single pixel in the image plane. The image usually consists of a square or rectangle of $n_x \times n_y$ pixels, each of area $\delta x \times \delta y$, centred at the position $[x_0, y_0, z_0]$ in the coordinate system of the Monte Carlo model. A ray is started from pixel (i, j) along a path normal to the surface of the image, which then steps through each cell of the model grid along its path until it exits the grid. Along this path, it accumulates the total intensity contributed by each cell by solving Eq. 17.

For each cell, the source function is given by

$$S_\nu^e = \left(1 - \exp\left[-\tau_\nu^{cell}\right]\right) B_\nu(T)$$

for the dust emission; a method for calculating the source function for scattering S_ν^s is given in the following section. This must then be reduced to account for the extinction of all the previous cells along the ray, by multiplying with $e^{-\tau}$, where τ is the optical depth from the edge of the cell to the image, and is increased after

5 This method is not restricted to computing parallel rays, and can in principle be adapted to any geometry. However, this description will focus on this particular case as it is the easiest to describe and the one most often applicable to astronomically relevant simulations, which typically seek to compare to observations conducted in the far field. For an example of a different geometry, see chapter 3, which uses divergent rays to simulate near-field observations.

each cell by τ^{cell}. This effectively treats the source function of each cell as part of the incident intensity to all previous cells along the ray's path.

If the model is assumed to be at a distance D from the observer, the flux density contributed by each cell to the pixel is

$$F_\nu = \frac{\delta x \delta y}{D^2} \left(S_\nu^e + S_\nu^s\right) e^{-\tau}, \tag{21}$$

which is summed over all steps of the ray's path.

It is important to note that these methods do not explicitly conserve energy except in the limit $\delta x \delta y \to 0$. Great care must therefore be taken to ensure that the spatial sampling of the model (i.e. the number of rays) is sufficiently high to capture all features of the model, and that any features appearing in images are real and not artefacts of the ray-tracing algorithm.

2.2.3 *The "Peel-off" technique*

Originally developed by Yusef-Zadeh et al. (1984) for the speedy creation of high signal-to-noise ratio scattered-light images based on Monte Carlo radiative-transfer simulations, this technique has proven both robust and extensible. The procedure focusses on using the probability of a photon reaching the observer after an interaction to calculate its contribution to the image or spectrum. The description here concentrates on determining the source function for scattered light, but the method has also been applied to provide an alternative to ray tracing when generating re-emission maps or SEDs.

Consider a photon which is in the process of being scattered by dust, coming from a direction $\hat{s}$. To determine the probability of it being scattered in the direction of the observer ($\hat{s}_{obs}$), one must first determine the angle through which the photon would have to be scattered, $\alpha = \cos^{-1}\left(\hat{s} \cdot \hat{s}_{obs}\right)$. This scattering angle can then be inserted into the scattering phase function $\Phi_\nu(\alpha)$ to find the probability of scattering in this direction.

If the photon were scattered into this direction, the probability of it escaping to reach the observer along this path would be

$$P_{esc} = \exp\left[-\tau_\nu^{ext}\left(\hat{s}_{obs}\right)\right], \tag{22}$$

where $\tau_\nu^{ext}\left(\hat{s}_{obs}\right)$ is the extinction optical depth integrated along the line-of-sight towards the observer. It therefore follows that the contribution of this scattering event to the observation is

$$I = \varepsilon \Phi_\nu(\alpha) P_{esc}. \tag{23}$$

One can consider this as the contribution of the scattering event to the source function ($\varepsilon \Phi_\nu(\alpha)$) attenuated by the line-of-sight optical depth.

This method may be implemented in two ways:

1. during the Monte Carlo simulation, or
2. by passing the source function to a ray tracing routine.

In the first case, the contribution to the image plane must be evaluated at each scattering event, which entails integrating the optical depth towards the observer many times, slowing down the Monte Carlo simulation itself and requiring that the entire calculation be repeated if the location of the observer was incorrect or if a new orientation is to be considered.

The second option, on the other hand, involves storing the position of each scattering event and the incoming direction of every scattered photon. This information is then passed to the ray tracer, which calculates S_ν^s for each cell, and includes it in the algorithm given in 2.2.2. This provides efficiency in that $\tau_\nu^{ext}(\hat{s}_{obs})$ is computed fewer times, and flexibility in that the images can be recalculated from any direction once the Monte Carlo simulation is complete. However, this comes at the expense of storing a potentially very large quantity of data.

The description given here only considered the contribution to the intensity, but the method has also been extended to include the polarisation induced by scattering (Gordon et al., 2001).

2.3 THE ROLE OF DUST IN THE STELLAR LIFE-CYCLE

With the discussion of the previous sections in mind, it is now possible to describe the influence of interstellar dust on astronomical observations and stellar evolution, and what these can teach us about interstellar dust itself.

2.3.1 *The diffuse interstellar medium*

Although the space between stars may look empty, it is not – it is in fact filled with diffuse gas, and approximately 1% (by mass) dust. The effect of this dust is subtle, but over astronomical distances the cumulative effect is sufficient to have a noticeable dimming and reddening effect on the light of stars, an effect known as *interstellar extinction*, and was first identified by Trumpler (1930) from the distance-dependent reddening of stars.

Extinction is the result of the absorption and scattering of stellar photons by the interstellar dust grains; due to the wavelength dependence of the optical properties of typical astronomical dust grains, shorter (UV-optical) wavelength photons are more likely to be absorbed or scattered than those at longer wavelengths, resulting in a ubiquitous "reddening" of distant stars. This reddening has been extensively studied to determine the properties of the dust, as the wavelength-dependence of extinction must be determined by the wavelength-dependence of the optical properties of the dust grains (e.g. Weingartner and Draine, 2001; Draine, 2003a; Voshchinnikov, 2004, 2012; Siebenmorgen et al., 2014).

The aforementioned studies have taught us a great deal about the properties of interstellar dust. Mathis et al. (1977, hereafter MRN) have shown that simple power-law distributions of grain sizes along the lines of

$$n(a)\,da \propto a^{-q}\,da \tag{24}$$

is able to explain the wavelength dependence of interstellar extinction, where a is the grain radius, $n(a)$ is the number density of grains with radius a, and the power-law index q has a typical value of 3.5 in the diffuse ISM, and minimum and maxi-

mum grain sizes $a_{min} = 10\,\mathrm{nm}$ and $a_{max} = 300\,\mathrm{nm}$ respectively, which has become known as the MRN distribution. It is now typically assumed that the grains in the ISM are composed of a combination of amorphous silicates, usually with stoichiometry $Mg_xFe_{(2-x)}SiO_4$, and either amorphous or graphitic carbon.

In the near-infrared, optical and ultraviolet, the extinction curve is featureless, except for a single bump at $\lambda \approx 2175$Å, often referred to as the "2200Å feature" or "extinction bump". This wavelength coincides with a strong resonance that arises as a surface mode in small ($a \leqslant 300$Å) graphite particles; this feature is therefore believed to be formed by absorption by small graphite grains (so called *very small grains* or vsgs).

At longer, mid-infrared, wavelengths other features appear, in particular strong, ubiquitous absorption (or emission) at $\sim 9.7\mu$m and $\sim 18\mu$m. As these coincide with a strong resonance in the optical properties of amorphous silicates (due to the stretching of Si–O bonds and O–Si–O bending respectively) and SiO_4 tetrahedra are among the most stable structures that can form from cosmically abundant materials, the features are often described as "the silicate features" and are taken as evidence that silicates comprise a significant portion of interstellar dust.

However, the wavelength-dependence of extinction is observed to vary across the sky (e.g. see Fig. 2 and Fitzpatrick and Massa, 2007). In particular, towards dense clouds and star-forming regions (see below) extinction at short wavelengths is weaker, and the 2200Å feature is generally weaker. If the wavelength-dependence of extinction is explained by the properties of dust, then this implies the presence of different dust in different directions.

As there is little room for radical variations in dust composition in the diffuse ISM, it is expected that these variations are the result of changes in the size of grains. Indeed, dust models show that these variations can be explained well enough by grain-growth processes, which are expected to be more efficient toward denser regions of the ISM. Larger grains absorb less efficiently (per unit mass) at shorter wavelengths, resulting in the flattening of the extinction curve. Meanwhile, grain growth would reduce the population of the very small grains responsible for the extinction bump, simultaneously weakening the feature when the extinction curve flattens.

Extinction is also observed towards extragalactic sources, allowing the examination of dust as a function of metallicity and, for sufficiently distant sources, as a function of cosmic time. The nearest well-studied extragalactic systems are the two Magellanic Clouds, whose extinction curves have been studied for several decades (e.g. Howarth, 1983; Prevot et al., 1984). The metal content of both of these satellites of the Milky Way is significantly lower and the dust properties also appear to be significantly different. Both galaxies have systematically stronger extinction in the UV, and significant differences in the extinction bump; the Large Magellanic Cloud has a weaker bump (Howarth, 1983), while the Small Magellanic Cloud has none at all (Prevot et al., 1984)! This has generally been explained in terms of a reduced average grain size and a reduced abundance of carbon, although it has also been suggested that radiative transfer effects may play a role in generating stronger UV extinction (Krügel, 2009).

At greater distances, extinction has also been studied towards bright galaxies such as starbursts (e.g. Calzetti et al., 1994) and active galactic nuclei (AGN) (e.g. Maiolino et al., 2001; Lyu et al., 2014). These show significant flattening of the extinction curve

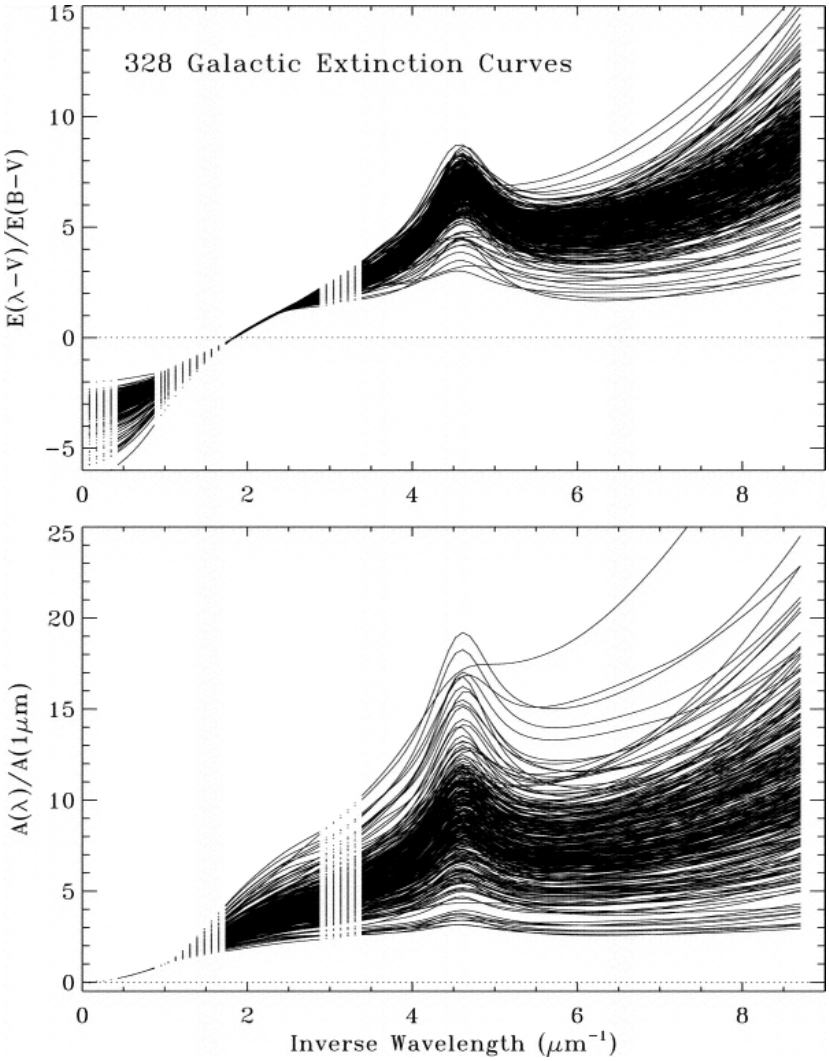

Figure 2: Observed variations in the diffuse galactic extinction curve. Reproduced from Fitzpatrick and Massa (2007), who measured extinction curves from the UV to the near infrared for 328 stars in the galactic plane.

Figure 3: Near-infrared (*left*) and visible light (*right*) views of NGC 6334 or the Cat's Paw Nebula, a large galactic star-forming region. As a result of the thick obscuration, substantially more stars are visible in the infrared, and the clumpy structure of the dust distribution is more obvious. *Image credit:* ESO/J. Emerson/VISTA

and the weakening or absence of the extinction bump; however in these cases it cannot necessarily be attributed to grain growth, and is likely to be an artefact of scattering effects in a clumpy medium (see chapter 3).

In chapter 3 we will return to the properties of interstellar extinction, and examine how the spatial distribution of dust and inhomogeneities influence the wavelength dependence of extinction.

2.3.2 *Star and planet formation*

In some regions, the density of the ISM increases, and the effect of extinction there produces spectacular dark clouds. However, beyond simply looking spectacular, these clouds are the birthplaces of stars, and by extension the source of life. They are home to complex chemical interactions, making them rich in organic molecules, earning them the name *molecular clouds*.

Dust plays a number of key roles in the star-forming processes in molecular clouds. As well as shielding the interior of the cloud from harsh UV radiation which would otherwise destroy the molecules that give the clouds their name, it enhances the formation of complex chemicals by providing a large surface area on which reactions can take place. Furthermore, dust allows the gas in the molecular cloud to cool, facilitating the fragmentation of the cloud under the influence of gravity, encouraging the formation of low-mass, solar-like stars.

Because dust enables efficient radiative cooling, it facilitates the deposition of volatiles to form ices. This results in substantial grain-growth as ice mantles collect on grain surfaces. These effects have been observed in a number of ways – initially by the change in the extinction curve towards stars located in or behind molecular clouds (e.g. Mathis, 1990, and references therin) and later by the detection of ice absorp-

tion features in near-infrared spectroscopy (e.g. Olofsson and Olofsson, 2011). The presence of ice mantles may aid further grain growth, by making the grain surfaces stickier, reducing the chances of grains bouncing off each other during collisions.

The ISM is inherently turbulent on many scales (Padoan et al., 1997), and this is equally true of molecular clouds. As a result, star–forming regions are clumpy and filamentary, with a relatively low volume filling factor of dense gas.

Molecular clouds are eventually destroyed by two processes. The formation of stars gradually consumes the cloud as it is accreted and integrated into cores, discs and protostars. Eventually, once a sufficiently large population of stars has formed, feedback from the stars in the form of radiation pressure, ionisation and wind momentum begins to expel material from the cloud, dominated by the most massive stars (Dale et al., 2012). As a result, molecular clouds are typically destroyed within a few Myr of the onset of star formation.

When the fragments within molecular clouds collapse to become protostars, the conservation of angular momentum causes the formation of a rotationally supported circumstellar disc (e.g. Shu et al., 1987), and dust once again dominates the thermal balance. This disc evolves viscously as it transfers angular momentum outwards, resulting in the accretion of material onto the central (proto-)star and the expansion of the disc (see Armitage, 2011, and references therein). The dust and gas in these discs are the building blocks of planetary systems. In particular, any earth–like planets will be created via the agglomeration of refractory and volatile (dust and ices, respectively) materials into ever larger bodies. An understanding of the dust in protoplanetary discs can therefore elucidate the formation of our own world.

The disc intercepts the radiation of the central (proto-)star, heating the dust to temperatures much higher than would be achieved if viscosity were the only form of energy transport taking place; this results in strong, optically thick mid- and far-infrared emission, often referred to as an infrared excess (e.g. Dullemond et al., 2007). This emission also extends to longer wavelengths, where it is commonly assumed to be optically thin, although this may not be the case (). The dust in the disc also scatters the stellar emission at short wavelengths, providing a different means to directly study the disc. The study of this radiation is therefore key to understanding the physics of planet formation and the early stages of stellar evolution, as it is one of the few tracers that can be directly observed.

As the disc evolves, the relative importance of the dust emission and scattering compared to the stellar radiation changes, following the evolutionary scheme of Lada and Wilking (1984) & Andre et al. (1993) as illustrated in Fig. 4. At first, only the emission from the cold dust is visible, meaning that the core can only be studied at the longest wavelengths. This optically thick core is referred to as a "Class 0" object. However, as material is either accreted onto the nascent protostar or ejected through outflows, the optical depth decreases sufficiently for warmer regions of the envelope and disc to become visible. Such a "Class I" object is dominated by the viscous heating of the disc, evidenced by the strong silicate absorption, which is caused by the cold dust in the outer envelope absorbing the emission of the hot dust in the inner disc. However, the emission from the protostar itself also becomes visible at this point. When the envelope has almost completely dissipated, the object moves into "Class II"[6], at which point the energy balance is dominated by the central star,

6 Often referred to as the Classical T Tauri phase.

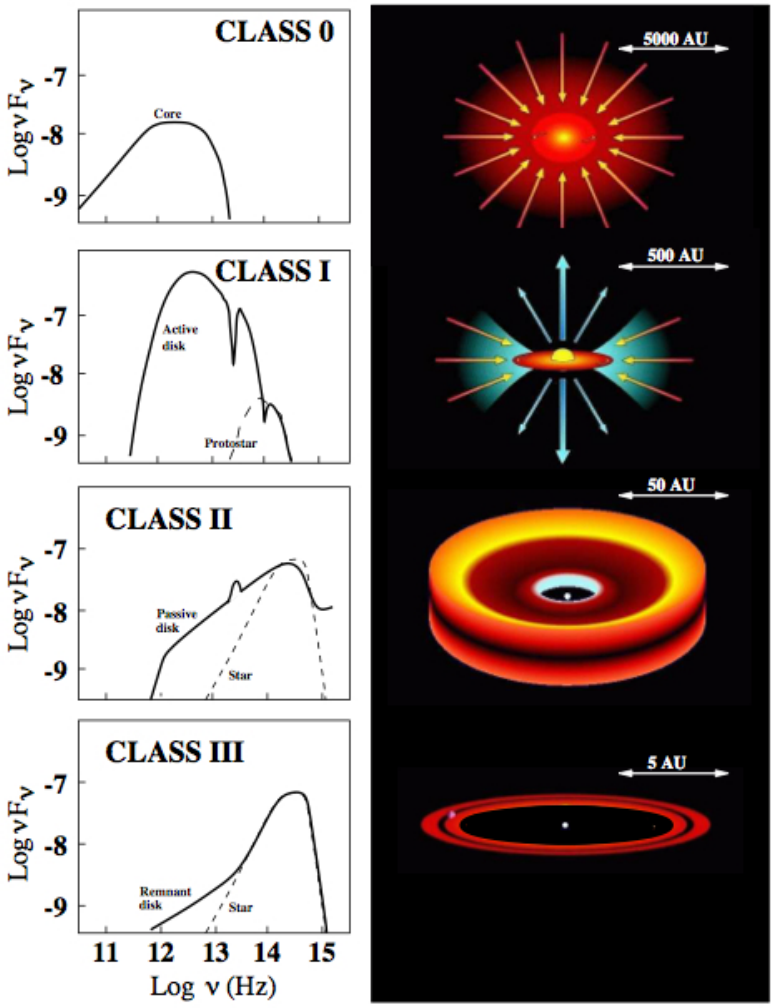

Figure 4: The temporal evolution of a young stellar object from an envelope dominated protostar (Class 0) to a Weak–lined T Tauri object (Class III), possibly the host of a debris disc. Reproduced from Isella (2006)

and depending upon inclination the star is either clearly visible with strong infrared excess from the disc (face-on), or only the disc emission is detectable (edge-on). It is assumed that this is the stage at which terrestrial planet formation takes place, although gas giants may have already formed by this point (Armitage, 2010). During this stage, the indications of accretion onto the star are clearly visible in the form of a UV–continuum excess, along with a number of spectral lines (Hartmann, 2009). When the disc has mostly evaporated or been turned into planets, the star moves into the "Class III" or weak–lined T–tauri phase. The disc is now probably limited to a debris disc similar to our solar system's asteroid belt or Edgeworth–Kuiper belt, and the stellar emission lines are now related to stellar activity rather than accretion (Walter et al., 1988). This phase may be preceeded by a short–lived transitional phased in which the disc is rapidly dispersed, referred to as a "transition disc" (e.g. Espaillat et al., 2014, and references therein).

Protoplanetary discs are, by astrophysical standards, extremely dense and turbulent, resulting in frequent collisions between dust grains. This results in rapid grain

growth, with grains growing to at least mm sizes (Testi et al., 2014), a critical part of the planet formation process. This growth is traced in a number of ways. As mentioned above, the silicate bands are ubiquitous features of interstellar dust, and they are also seen toward protoplanetary discs. However, the shape and relative strength of these features is determined by the composition and size of the grains, with larger grains generally showing broader, weaker features (e.g. Bouwman et al., 2001). This has be used to explore the size and crystallinity of warm dust, probably in the regions where terrestrial planet formation is on going, and it has been found that large, crystalline grains are a common feature of discs (e.g. Bouwman et al., 2001). Indeed, high resolution studies have even found that the average size and crystallinity of grains is higher in the inner regions of the disc (van Boekel et al., 2004). However, for grain sizes larger than $\sim 5\,\mu m$ the silicate features almost disappear (Bouwman et al., 2001), limiting the applicability of this method.

Tracing grain growth to larger sizes relies on the behaviour of the dust emission in the optically thin limit[7]. For long wavelengths, this is usually characterised by a simple power law with $F_\nu \propto \lambda^{-\alpha}$, which is related to the efficiencies of the grains $Q_{abs} \propto \lambda^{-\beta}$ as $\alpha = 2 + \beta$ (Beckwith et al., 2000). The value of β is a strong function of the distribution of grain sizes; for ISM dust $\beta \sim 1.7$, but when the size parameter of the largest grains approaches 1 the value of β falls (Beckwith et al., 2000). Therefore, by observing at long wavelengths where the disc emission is optically thin (i.e. $\lambda \gtrsim 0.5\,mm$), one can probe the presence and distribution of grains at these large sizes. Such observations have recently become feasible, and are now showing that grains with sizes $\sim 1\,mm$ are common in protoplanetary discs (e.g. Rodmann et al., 2006; Ricci et al., 2010).

While the small grains present in the ISM couple extremely strongly to the gas motions, large grains decouple of the gas, allowing them to settle towards the mid-plane of the disc. At the same time, they start to experience drag from the gas, transferring angular momentum from the dust to the gas, resulting in the dust grains spiralling inwards. As the density of large grains increases through these processes, the probability of collisions between large particles increases, encouraging further growth. In models of terrestrial planet formation and in the Core-accretion model of giant planet formation this is a key phase in the formation of planetary embryos.

The study of dust around young stars is therefore crucial to understanding the formation of planets. By studying the prevalence of accretion and IR excess as a function of cluster age, Fedele et al. (2010) derived a disc dispersal timescale of $\sim 3-5\,Myr$, a key constraint on the planet formation time scale.

We will return to this topic in chapters 4 & 5. Chapter 4 discusses the possibility of a star that has evolved sufficiently to lose its initial circumstellar disc might pass through a dense clump within its parent molecular cloud before the cloud has dispersed. We then consider the possibility that it might accrete material from the clump and form a "second generation" disc, potentially providing a second chance for planet formation. Chapter 5 then presents new observations and detailed radiative transfer modelling of the nearby but enigmatic binary YSO VV Corona Australis. We explore whether the combination of mid-infrared interferometric observations, which probe the inner regions of the discs, with the global information carried by

7 I.e. when it is completely determined by the absorption efficiencies.

the SED is sufficient to constrain the properties of the circumstellar discs and the evolutionary state of the central stars.

2.3.3 *The late stages of stellar evolution*

As discussed above, dust plays a key role in star formation. However, the early universe was devoid of the heavy elements required for dust formation, and these had to be formed by stellar fusion and dispersed by supernovae, leaving something of a causal dilemma.

When stars of solar mass or higher approach the end of their lives, they expand dramatically and their surfaces cool to become Red Giants[8], or in the case of particularly massive stars, Red Supergiants (Ekström et al., 2012). During this stage, stellar pulsations, turbulence, convection, magnetic fields or some combination of them result in material being lifted above the stellar photosphere to create an extended atmosphere (e.g. Arroyo-Torres et al., 2015). This atmosphere is cool enough for dust grains to form, which then enhances the cooling of the atmosphere, allowing further dust formation in a runaway manner (Woitke, 2006).

This dust then forms a dense circumstellar envelope, often clumpy. Once again, the dust couples effectively to the stellar radiation, resulting in strong infrared excess emission (van Loon et al., 2005). However, this process also imparts momentum to the dust grains, and the resulting radiation pressure is sufficient to accelerate the grains to escape velocity. The grains then drag the atmospheric gas molecules along, driving an outflow (van Loon et al., 2005). Since the parameters that control dust formation are usually variable, this often results in the formation of a series of detached dust shells. The presence, size, shape, spacing and other properties of the shells or other structures in the envelope are determined by the mechanisms initiating the mass loss, and can be used to infer key attributes of the mass-loss processes (e.g. Kerschbaum et al., 2010).

It is therefore interesting to study the mass-loss and dust formation mechanisms themselves to understand the enrichment of the ISM with metals[9] and dust. However, this is complicated by the thick obscuration from the circumstellar dust shell. Hence, radiative transfer modelling must be used in order to correctly interpret observations.

By studying the dust in these shells we can about the initial composition of the materials that contribute to interstellar extinction, providing additional constraints for dust models. Many of the refactory materials that form dust in these outflows have spectral features in the mid-infrared, and hence enhanced emission or absorption at the wavelengths of these features (e.g. Verhoelst et al., 2009, and Fig. 5). By studying the mid-infrared spectra of mass-loss giants, and fitting the emission features with relevant compositions it is possible to disentangle the contributions from several dust species (see Fig. 5).

This has been done for a number of different environments. The chemistry, and hence materials available to form dust, of evolved stars is dominated by the relative abundances of Carbon and Oxygen. Oxygen is more abundant throughout the uni-

8 These are divided into the Red Giant Branch (RGB) and AGB stars. The AGB phase occurs after the RGB phase for stars between about 0.8 and $8\,M_\odot$. For most stars, the majority of the mass loss (and hence dust production) discussed below occurs on the AGB.

9 In astronomy, all elements except Hydrogen and Helium are considered metals.

verse, so all stars initially have a C/O ratio $\leqslant 1$, and are hence referred to as "Oxygen rich". When stars first being producing dust on the AGB their chemistry is, therefore, dominated by oxygen, leading to the formation of metal oxides and, crucially, the ubiquitous Mg–Fe silicates which, unlike ISM silicates, show signs of crystallisation (Waters et al., 1996). However, stars on the AGB undergo sporadic phases of Helium–shell fusion, known as thermal pulses. These pulses result in increased convection from the Hydrogen and Helium shells to the stellar surface, dredging up fusion products (Carbon and Oxygen) and S-process elements from the core and shells. For stars in a certain range of masses this dredge up may eventually change the C/O ratio such that the chemistry in the dust-formation zone is dominated by Carbon. The envelopes of Carbon stars are therefore the sources of the amorphous carbon and graphite in the ISM, although they also show evidence for complex chemistry and more complex dust species including SiC, FeS, or MgS (Hony et al., 2003).

Massive stars, on the other hand, remain oxygen–rich throughout their entire evolution. The dust produced by RSGs is, therefore, broadly similar to that of O–rich AGB stars. However, there are key differences; RSG envelopes show a greater diversity of silicates, including Ca–Al silicates similar to those found in meteorites, and they also show strong evidence for some featureless dust species, which is often attributed to metallic Fe, although chromospheric activity may photodissociate enough CO to enable Carbon dust formation (Verhoelst et al., 2009).

Evolved stars convert a significant fraction of their mass into dust (see, e.g. Villaume et al., 2015, and references therein, or alternatively chapter 6 of this work), and are expected to be the primary sources of dust in the universe, although supernova remnants are also observed to produce dust (e.g. Gall et al., 2011; Wesson et al., 2015). This dust is injected into the ISM, and eventually forms molecular clouds which then go on to form new stars, planets, and potentially life-forms, as discussed above. An individual AGB star may eject up to 80 % of its mass before forming a white dwarf, injecting 0.005–0.05 $M_\odot$ of dust[10] into the ISM depending on the initial mass of the star (Ekström et al., 2012). Integrating over the stellar mass function, and accounting for the length of the period of mass loss, one finds that $\lesssim 0.1\,M_\odot\,yr^{-1}$ of dust is injected into the galactic ISM (e.g. Gehrz, 1989).This is dominated (up to 50 %) by the contribution of a relatively small number of Carbon stars and so–called OH/IR stars[11]. Less than ~10 % comes from massive stars, with the remainder produced by the large population of O-rich AGB stars. Similar studies have been performed for the Magellanic Clouds (e.g. Matsuura et al., 2009) and have found a total of $\sim 10^{-4}\,M_\odot\,yr^{-1}$ for the LMC, somewhat less than might be expected given its lower mass compared to the Milky Way (~ 0.01); this is attributed to its lower metallicity. Also as expected given the lower abundance of metals, the dust budget is more heavily dominated by Carbon stars, as the conversion from O-rich to C-rich happens earlier in an AGB star's evolution.

Large quantities of dust are also observed in other galaxies, even in the very early universe. Although the lower-mass, more-numerous AGB stars may contribute the majority of dust in the Milky way, observations of dust in high-redshift galaxies argue that the massive, short-lived stars that become RSGs must produce substantial quantities of dust (0.1–1 $M_\odot$) in order to pollute the high-z ISM with the amounts of

10 Assuming a typical gas–to–dust ratio of 200

11 Massive O-rich AGB stars with very high mass–loss rates

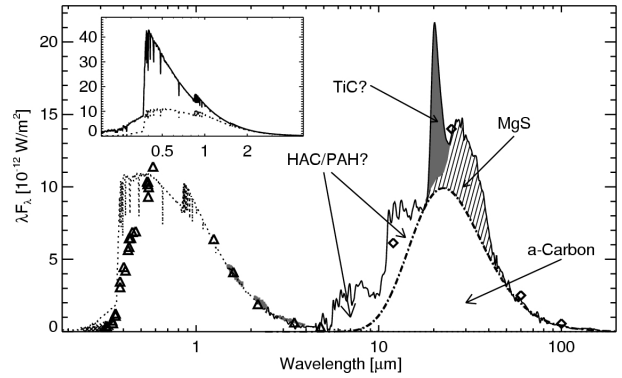

(a)

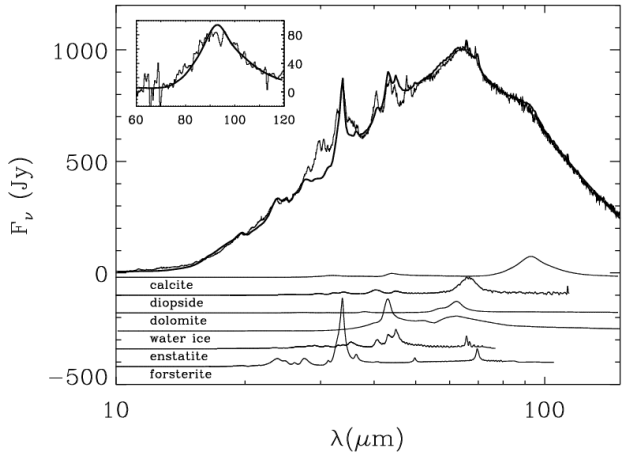

(b)

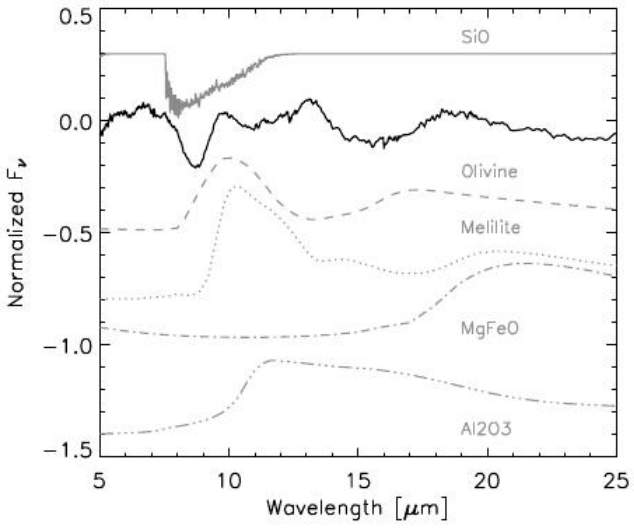

(c)

Figure 5: Examples of the mid-infrared spectral features of evolved stars. *Top:* The spectrum of the C-star HD 56126 highlighting several emission features (reproduced from Hony et al. 2003). *Middle:* The spectrum of the (more evolved) O-rich planetary nebula NGC 6302, showing the dust components required to fit the emission (reproduced from Kemper et al. 2002). The dust was produced during the O-rich AGB phase. *Bottom:* The spectral features of several dust species commonly assumed to form in the envelopes of RSGs (reproduced from Verhoelst et al. 2009).

dust observed (e.g. Rowlands et al., 2014, and references therein), as very few low–mass stars will have evolved off the main sequence by this point. Whether this dust is formed while the stars are RSGs or from the material ejected in supernovae is still a matter of debate.

Supernovae are, by definition, energetic events which produce both hard radiation and shocks in abundance, potentially destroying any grains near the supernova either in the shocks or through sublimation. The contribution of RSGs to galactic dust budgets therefore depends on the time between dust formation and the supernova[12] and how resistant the grains are to these destructive processes. The resistance of dust grains to destruction is a function of the grain size, structure and composition, with larger grains being destroyed less efficiently; they survive sublimation more easily because they are cooler in the same radiation field and survive longer at the same temperature (Waxman and Draine, 2000) and the increased size makes them more robust again shocks (Gall et al., 2014). As a result, determining the size of grains produced by RSGs is key to understanding their contribution to interstellar dust, both in the local universe and at high redshift.

In Ch. 6 we will return to these topics. We will examine the circumstellar envelope of the dustiest and most luminous nearby RSG, VY Canis Majoris, using radiative transfer modelling and high–contrast imaging & polarimetry to explore the morphology of the ejecta, the mass–loss history of the star and the distribution of grain sizes in the envelope. Based on this, we explore the survivability of the dust in the event of a supernova.

12 Or the distance travelled by the grains in that time.

3

EXTINCTION IN CLUMPY MEDIA

The dust content of the universe is primarily explored via its interaction with stellar photons, which are absorbed or scattered by the dust, producing the effect known as interstellar extinction. However, due to the physical extension of the observing beam, real observations may detect a significant number of dust-scattered photons. This may result in a change in the observed (or effective) extinction, with a dependence on the spatial distribution of the dust and the spatial resolution of the instrument. We investigate the influence of clumpy dust distributions on the effective extinction toward both embedded sources and those seen through the diffuse ISM. We use a Monte Carlo radiative transfer code to examine the effective extinction for various geometries. By varying the number, optical depth and volume filling factor of clumps inside the model for spherical shells and the diffuse ISM we explore the evolution of the extinction curve and effective optical depth. Depending on the number of scattering events in the beam, the extinction curve is observed to steepen in homogeneous media, and flatten in clumpy media. As a result, clumpy dust distributions are able to reproduce extinction curves with arbitrary $R_{V,\mathrm{eff}}$*, the effective ratio of total-to-selective extinction. The flattening is also able to 'wash out' the 2175 Å bump, and results in a shift of the peak to shorter wavelengths. The mean* $R_{V,\mathrm{eff}}$ *of a shell is shown to correlate with the optical depth of an individual clump and the wavelength at which a clump becomes optically thick. Similar behaviour is seen for edge-on discs or tori. However, at grazing inclinations the combination of extinction and strong forward scattering results in chaotic behaviour. Caution is therefore advised when attempting to measure extinction in e.g. AGN tori or toward SNIa or GRB afterglows. In face-on discs, the shape of the scattered continuum is observed to change significantly with clumpiness, however, unlike absorption features, individual features in the scattering cross-sections are preserved. Finally, we show that diffuse interstellar extinction is not significantly modified by scattering on distance scales of a few kpc.*

Material in this chapter is adapted from:
P. Scicluna & R. Siebenmorgen; accepted for publication in A&A.

3.1 INTRODUCTION

The presence and nature of dust in the universe can be explored by observing both the thermal radiation it emits, and its influence on stellar photons which it absorbs and scatters to produce extinction. Both of these methods sample different dust populations, with emission being most sensitive to the hottest dust components along the entire line-of-sight, while extinction is sensitive to the full column of dust between the observer and the extinguished source. Therefore, the wavelength dependence of interstellar extinction can be interpreted in terms of the wavelength dependence of the probability for dust and radiation to interact, i.e. the dust cross-sections. Extinction is observed to vary on different galactic lines of sight (e.g. Fitzpatrick and Massa 1990, 2007, hereafter FM07), and extragalactically (Howarth, 1983; Prevot et al., 1984;

Calzetti et al., 1994). Hence, attempts are frequently made to analyse the composition of dust on given lines-of-sight by fitting the extinction curve using extinction cross-sections for likely mixtures of materials and particle sizes. One must, therefore, ensure that all possible biases and systematic effects are accounted for in the treatment of extinction.

One key and often overlooked bias is the real angular extent of the observing beam in which extinction measurements are made. Since the observations are not made using a pencil beam, there is a non-zero probability of detecting scattered light (Mathis, 1972; Krügel, 2009), both increasing the total detected flux and altering the wavelength dependence of extinction. It is also possible that an in-homogeneous dust distribution will present paths with different optical depths, with the relative covering fractions of the different phases influencing the detected flux.

In galactic observations of the diffuse ISM the impact of scattering is typically assumed to be negligible, an assumption that we will consider more carefully in Sect. 3.4.3. Nevertheless, in regions where dust and stars are well mixed or where the physical size of the observing beam is large compared to the structure of the dusty medium, the fraction of scattered light can become significant. This may occur in more distant galactic star-forming regions (Natta and Panagia, 1984) or for stars embedded in a compact (compared to the resolution) envelope or disc, i.e. dust enshrouded (young or evolved) stars (Voshchinnikov et al., 1996; Wolf et al., 1998; Indebetouw et al., 2006). Similarly, inhomogeneity and scattering effects also become significant in extragalactic astronomy (Bruzual A. et al., 1988; Calzetti et al., 1994; Witt and Gordon, 2000), where an entire star-forming complex can comfortably fit within a single resolution element.

As a result, unresolved observations of such systems must correctly account for these effects or they will derive significantly different extinction laws that do not necessarily indicate any change in the physical nature of the dust grains. Such effects can include both steepening (Krügel, 2009) and flattening (Natta and Panagia, 1984) of the extinction curve, under- or overestimation of stellar luminosities, or even negative extinction depending on the distribution of the dust and the size of the aperture (Krügel, 2009).

This chapter makes use of numerical radiative transfer models to investigate the effect of scattering and clumpiness on extinction. Section 3.2 reviews the relevant theory and previous findings, and Sect. 3.3 outlines the computational methods we employ. The remainder of the paper then investigates these effects with particular attention paid to circumstellar shells, discs and the diffuse ISM.

3.2 EFFECTIVE EXTINCTION

Following Krügel (2009), the interstellar extinction law is defined as

$$\frac{\tau(\lambda)}{\tau_V} = \frac{K_{ext}(\lambda)}{K_{ext}(V)} \tag{25}$$

where τ is the optical depth and K_{ext} the extinction cross-sections of dust, for observations with infinite resolution. The so called *true extinction* is therefore influenced only by the column density of extinguishing material (i.e. ISM dust) along the line of sight

and the wavelength dependence of its interactions with light. Using the other standard definitions for colour excess $E(B-V) = A(B) - A_V$ and $E(\lambda - V) = A(\lambda) - A_V$, where A denotes the extinction in magnitudes, one arrives at

$$k(\lambda - V) = \frac{E(\lambda - V)}{E(B-V)} \tag{26}$$

which is the traditional form of the extinction law in terms of colour excess. This then naturally leads to the definition of the ratio of total-to-selective extinction

$$R_V = -k(0 - V) = \frac{\tau_V}{\tau_V - \tau(B)}. \tag{27}$$

As a result, the broadband behaviour of the extinction curve can be described to first order by this quantity, R_V, and hence so can the dust properties. By finding combinations of dust grains whose cross-sections reproduce the observed R_V one can therefore hope to understand the composition of dust along a particular line of sight.

In order to do this, one must suppose some dust constituents, typically some combination of silicon and carbon bearing species, which may be in distinct grain types (e.g. separate carbon and silicate bearing grains) or mixed together (composite grains). One must also choose a grain geometry (e.g. spherical, spheroidal, fractal etc.) and whether the grain densities are homogeneous or porous. Then, by assuming a size distribution of the particles, one can compute the extinction cross-sections, albedo, phase function, etc. for the dust model and compare the wavelength dependence of these properties to those observed for interstellar dust. For a more detailed discussion of the processes involved in fitting the extinction curve, please refer to the literature (e.g. Weingartner and Draine, 2001; Draine, 2003a; Voshchinnikov, 2004, 2012; Siebenmorgen et al., 2014).

However, in real observations a number of effects can complicate the picture. Firstly, although the extinction cross-sections are defined as

$$K_{ext} = K_{abs} + K_{sca} \tag{28}$$

in general scattering is not isotropic, meaning that observationally there is a degeneracy (Voshchinnikov, 2002) between the albedo $\omega = K_{sca}/K_{ext}$ and the anisotropy parameter

$$g = \langle \cos(\theta) \rangle = \int p(\cos(\theta)) \cos(\theta) \, d\cos(\theta) \tag{29}$$

where $p(\cos(\theta))$ is the probability density function of the scattering angle θ, which parametrises the expectation of the scattering direction, with 1 corresponding to pure forward scattering and -1 to pure back-scattering.

Furthermore, in real astronomical observations, the aperture or beam in which the extinction is measured is not a pencil beam and has some physical extension, determined by the resolution. Ergo, unresolved structure within the beam can alter the observed extinction by for example

- partially occulting the source;

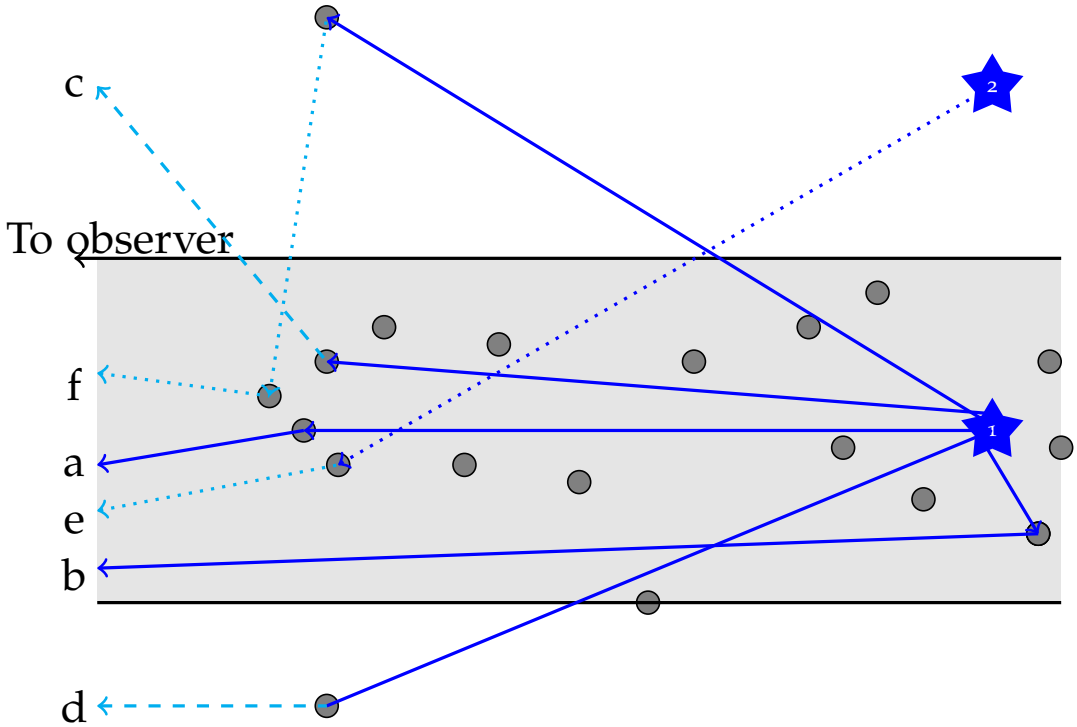

Figure 6: Scattered photons may still be observed on the detector. The grey shaded region between the two black lines indicates the volume swept out by the observing beam of the telescope as it extends into space. Photons (light and dark blue lines) that arrive at the detector at the end of this region (marked 'To observer') will be observed as though they originated at the star. The grey circles represent a distribution of dust along the line of sight toward the star being observed. The dark full lines show the contributions we consider here: 'undeflected' photons (a) which are forward scattered and do not leave the beam, and photons which are back-scattered (b) into the beam. The pale dashed lines (c,d) show cases where the scattering event leads to the photon leaving the observing beam. Finally, the dotted lines (e,f) represent cases that may contribute to observations, but occur with significantly lower probabilities and are hence not considered in this chapter.

- inhomogeneities biasing observations toward low-τ paths;
- scattering light into the beam;

which can combine with the aforementioned degeneracy. Figure 6 depicts this in cartoon fashion for sources in the far field.

When the extinguished source and the observer are roughly equidistant from the extinguishing material, this effect is negligible (Krügel, 2009), but is increasingly significant the shorter the physical distance between the star and the attenuating matter. It naturally follows that this effect is most significant for embedded objects and extragalactic observations.

To account for this, previous authors (see e.g. Krügel, 2009) have defined the *effective* optical depth and extinction curve i.e.

$$\frac{\tau_{\mathrm{eff}}(\lambda)}{\tau_{\mathrm{V,eff}}} \neq \frac{K_{\mathrm{ext}}(\lambda)}{K_{\mathrm{ext}}(V)}, \tag{30}$$

where $\tau_{\rm eff}$ is the optical depth one derives from the observations; i.e. the negative of the logarithm of the ratio of the observed flux to the flux that *would be observed in the absence of dust*

$$\tau_{\rm eff} = -\ln\frac{F_{\rm obs}}{F_{\rm o}}. \tag{31}$$

From this follows the definitions of $R_{V,\rm eff}$ as in equations 25 to 27 with $\tau_{\rm eff}$ instead of τ. This is similar to the definition of attenuation optical depth $\tau_{\rm att}$ used in e.g. Witt and Gordon (2000), but noticably different from the definitions of $\tau_{\rm eff}$ used in Witt and Gordon (1996) and Wolf et al. (1998) and $\tau_{\rm att}$ in Fischera and Dopita (2005), which exclude the contribution from scattered photons.

It should also be clear that unlike τ, $\tau_{\rm eff}$ is a function not only of the source and its dust distribution, but also of the aperture in which it is observed (Krügel, 2009). Krügel (2009) also highlights that $\tau_{\rm eff}$ is never larger than τ, and that it can even be negative (e.g. in a reflection nebula). When the dust distribution is homogeneous, $\tau_{\rm eff}$ depends only on τ, the dust composition and the aperture, while for inhomogeneous media the spatial distribution of dust and the viewing angle are clearly also important (Wolf et al., 1998).

3.3 MONTE CARLO MODELS

As the exploration of the effective extinction necessitates accurate radiative transfer modelling in inhomogeneous media, we must use Monte Carlo methods.

We use an implementation originally described in Krügel (2008), and significantly expanded upon in Siebenmorgen and Heymann (2012) and Heymann and Siebenmorgen (2012). The code allows for an arbitrary choice of geometry, dust composition, and illumination source, and includes anisotropic scattering. The radiative transfer problem is solved by launching packets of radiation from the source and following their interactions with the surrounding dust distribution.

The dust distribution consists of a Cartesian grid of densities and temperatures. The interactions of the radiation packets are then computed based on the method in Krügel (2008) which employs the 'immediate temperature update' method of Bjorkman and Wood (2001). This method has been extended to include the Lucy (1999) algorithm for the dust temperatures in optically thin regions to reduce the uncertainty in the dust temperatures, and to include anisotropic scattering by sampling scattering angles from the Henyey-Greenstein (HG) phase function (Henyey and Greenstein, 1941)

$$p\left(\cos\left(\theta\right)\right) = \frac{1}{4\pi}\frac{1-g^2}{\left(1+g^2-2g\cos\left(\theta\right)\right)^{3/2}}, \tag{32}$$

where g is the anisotropy parameter (Eq. 29) derived from Mie calculus (Mie, 1908; Bohren and Huffman, 1983). This can be re-arranged to give

$$\cos\left(\theta\right) = \frac{1}{2g}\left[1+g^2-\left(\frac{1-g^2}{1+g\left[2P-1\right]}\right)\right] \tag{33}$$

where $P = \int p\left(\cos\left(\theta\right)\right) \mathrm{d}\cos\left(\theta\right)$ is the cumulative probability distribution, from which the scattering angle can be sampled directly. As this function contains a singularity

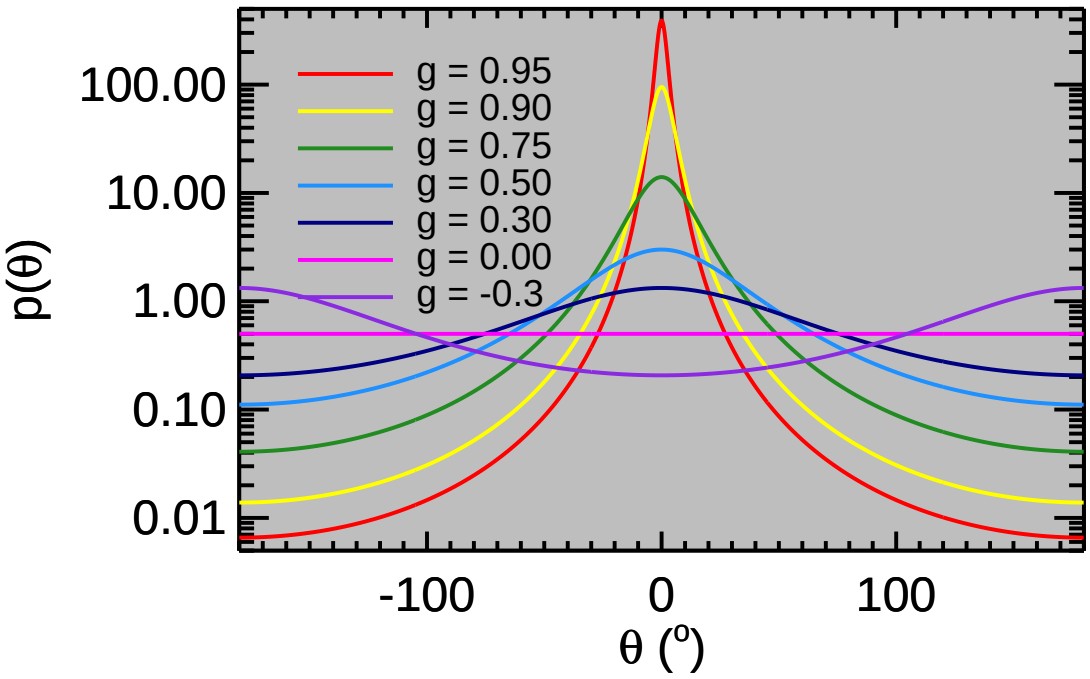

Figure 7: Probability density function of the Henyey-Greenstein phase function as a function of scattering angle for a representative range of g-factors. $\theta = 0°$ indicates that the outgoing direction of the scattered photon is identical to that of the incoming one, while $\theta = \pm 180°$ implies a reversal of direction (back scattering).

for $g = 0$ it is necessary to catch these cases and explicitly interpret them as isotropic scattering. Figure 7 shows probability density functions $p(\theta)$ for the HG function over a representative range of the g parameter.

The importance of anisotropic scattering can be seen in Fig. 8, which shows a difference image comparing the same disc model viewed in scattered light using either the HG function or a pseudo-isotropic approximation, in which the scattering cross-sections are reduced by $K'_{sca} = (1 - g)\, K_{sca}$, which effectively divides the scattering into an isotropically scattered component and a forward scattered (unscattered) component, which works well for $0 \leqslant g \ll 1$ and $g = 1$ but becomes increasingly poor as $|g| \to 1$. It is clear that the HG function shows a completely different distribution of scattered flux, with the near-side of the disc significantly brighter and the far-side darkened.

Since the Monte Carlo method is able to follow the packets explicitly, $\tau_{\rm eff}$ can be directly computed for all wavelengths, and hence $R_{V,\rm eff}$, simply by counting how many packets emerge from the cloud at a given wavelength.

A number of apertures can be defined on the basis of viewing angle or physical location. As photon packets exit the model grid, they are added to the statistics for the relevant apertures. Effective extinction curves are thus built up by computing the number of photons within the aperture and comparing to the number that would have been detected in the absence of dust (Eq. 31).

The code, including anisotropic scattering, is parallelised using the OpenMP API for use on shared memory machines. When only interested in the influence of scattering and extinction by dust on the ultraviolet, optical and near infrared, the code can

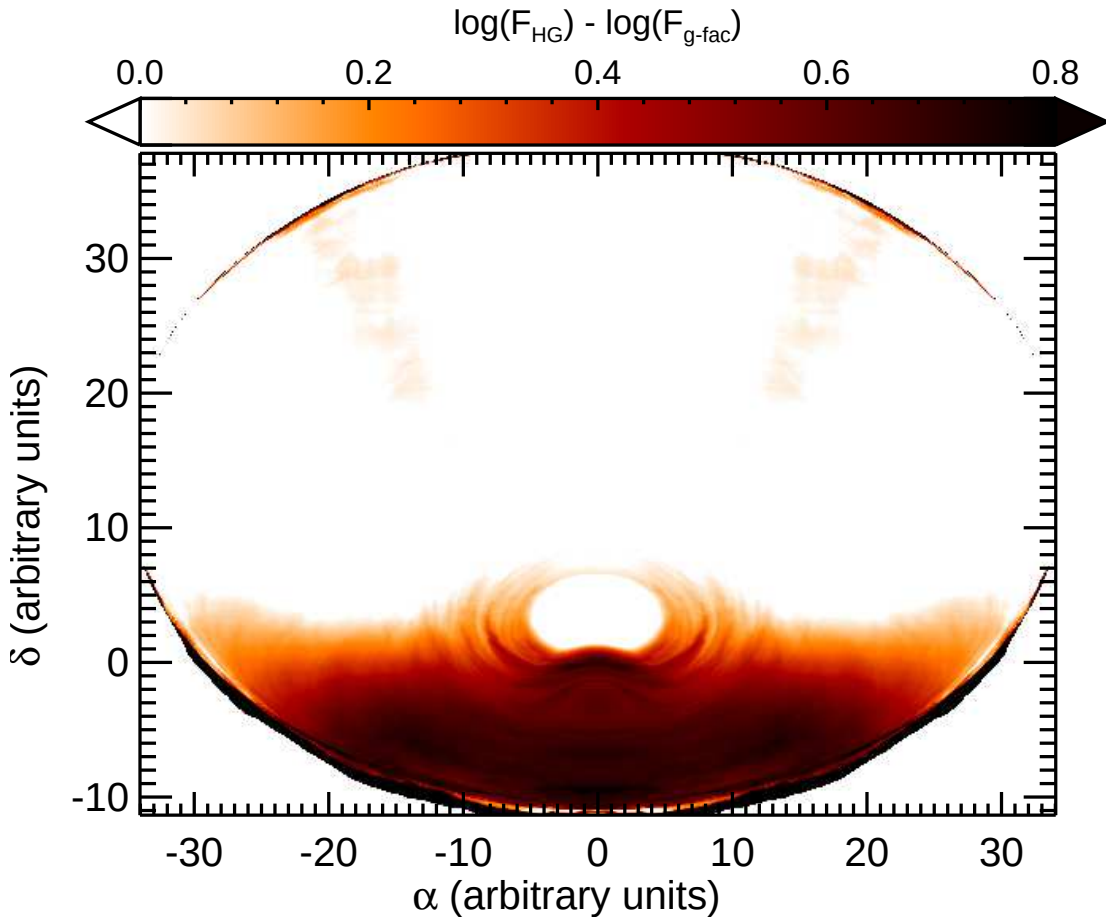

Figure 8: Difference image between the V-band scattered flux computed assuming the HG phase-function (F_{HG}) and a pseudo-isotropic one (F_{g-fac}), computed for a dust disc with a half-opening angle of 30° viewed from an angle of 45° from the rotation axis using a combination of amorphous carbon and silicate dust. The region of the disc at $\delta \leqslant 0$ is the near-side of the disc. The HG function reproduces the strength of forward scattering much more effectively, with differences between the two methods of up to an order of magnitude, although the integrated scattered flux is the same using both methods.

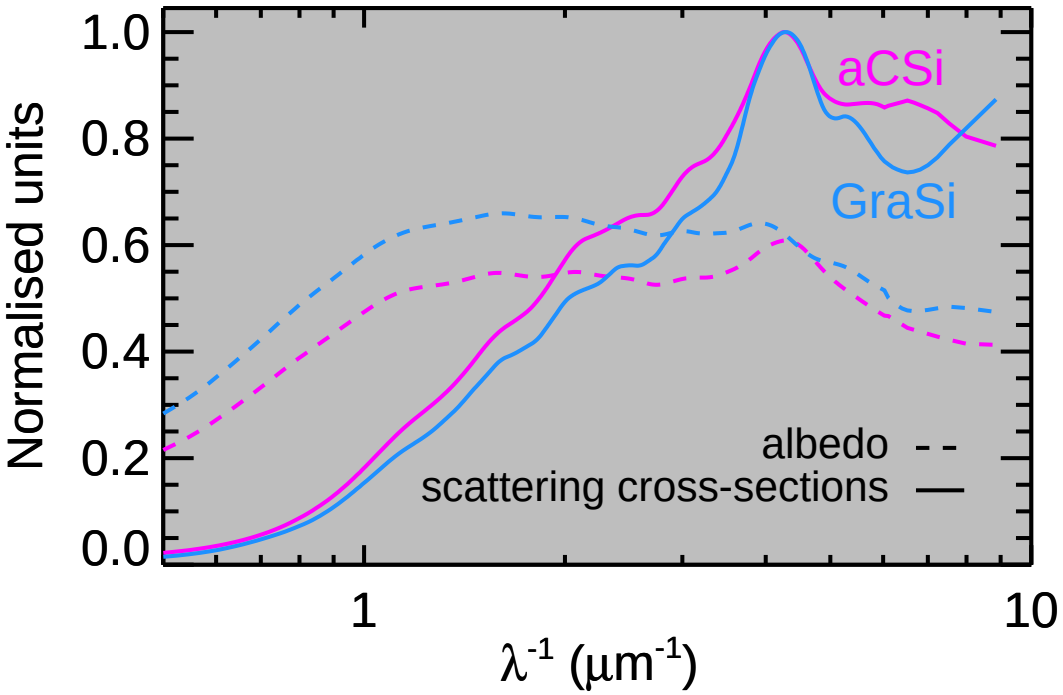

Figure 9: Normalised scattering cross-sections (full lines) and albedo (dashed lines) as a function of wavelength for both dust models. While the albedo is rather flat, the cross-sections show a strong peak between $200 - 250$ nm.

be further optimised by neglecting dust emission. In this case all photon packets absorbed by the dust are discarded and the runtime of the code is decreased by a factor of four. Nevertheless the models remain computationally intensive, and although the physical scale of the apertures in which the extinction is computed are correct, it is necessary to overestimate their angular extent to develop sufficient statistics without the runtime becoming infeasible.

In these studies we consider the so-called MRN grain size distribution ($dn(a) \propto a^{-q}\, da$, $q = 3.5$ Mathis et al. (1977)) of silicate and amorphous carbon. Since we are looking for changes caused by the dust geometry, the precise dust model chosen is not important. Two dust models are used depending on the conditions to be explored:

- amorphous carbon and silicates (aCSi), using optical constants from Zubko et al. (1996) and Draine (2003b), respectively;
- graphite and silicates (GraSi), using optical constants from Draine (2003b).

Both models consist of carbonaceous grains with radii between 16 nm and 130 nm and silicate grains between 32 nm and 260 nm. The bulk density of the dust grains is 2.5 g cm^{-3}, and the carbon-to-silicate abundance ratio is 6.5. The scattering cross-sections of both models peak around 250 nm (see Fig. 9).

High signal-to-noise images can be generated by post-processing the output of the radiative transfer simulations by using a ray-tracer. Scattered light images require that the position, frequency and direction of photonsbefore a scattering event are

stored. Then this information is read into the ray-tracing algorithm, and used to calculate the angle between the incident photon and the observing direction

$$\cos\theta = \hat{\vec{\ell}} \cdot \hat{\vec{\ell}} \tag{34}$$

where $\hat{\vec{i,\ell}}$ indicate the incoming and observer direction unit vectors, respectively. The probability to scatter the photon packet into the viewing direction is then determined from the scattering phase-function (Eq. 32), and this fraction of the packet is added to the ray. This is similar to the so called "peel-off" technique (Yusef-Zadeh et al., 1984). Emission images are computed by integrating the emission determined from the dust temperatures, cross-sections and optical depth along the line of sight. Both routines include a correction for the attenuation caused by the line-of-sight optical depth. In the case of a very small aperture (e.g. simulated observations of extinction in the diffuse ISM) the same signal-to-noise ratio can be achieved in a much shorter time by exploiting this capability to integrate over all scattering events.

While astronomical ray-tracing applications usually only consider models in the far field, allowing them to use parallel rays, models of the ISM need to consider photon scattering along the entire line-of-sight. Hence, perspective-projection ray tracing (e.g. Appel, 1968) must be applied to capture the effect of the beam widening as the distance from the observer increase; the direction of a ray now depends upon its position on the detector, and all rays are divergent. This requires an update to the prescription in Heymann and Siebenmorgen (2012).

In order to determine the deflection of each ray, one must first know the field-of-view required from the image. This is calculated from the inverse tangent of the projected size of model and the distance to the object e.g. for a cuboid where the long (z) axis is parallel to the central ray

$$\theta_{FOV} = 2\tan^{-1}\left(\frac{\Delta x}{D}\right) \tag{35}$$

where Δx is the length of the x-axis of the model and D is the distance from the observer to the object. This ensures that the entire model fits into the image at the location of the object.

The deflection between adjacent pixels is then given by $\delta\theta_{pix} = \theta_{FOV}/n_{pix}$ for a square image with $n_{pix} \times n_{pix}$ pixels. The direction of the ray launched from each pixel can then be found by rotating the direction of the vector joining the detector to the object by integer multiples of $\delta\theta$.

Because the rays are divergent, the size of each pixel becomes a function of the distance from the detector along the ray. If d is the distance the ray has travelled so far, then the pixel area $A(d) = (d\delta\theta)^2$. This value must be substituted for the constant value of the pixel size A in Eq. 17 of Heymann and Siebenmorgen (2012). The algorithm is otherwise identical to standard parallel-projection ray-tracing methods.

The Monte Carlo code is used to calculate the temperature structure and distribution of scattering events in the model cloud and then calculate images at all the wavelengths of interest ($\lambda < 3\mu m$) with the ray–tracer. In an analogous manner to real observations, these images are then compared to identical images of dust-free simulations, and the effective optical depth and extinction curve are calculated (Eq. 31).

Table 1: Clumpy shell model parameters

Parameter		Values	Note
Inner radius	R_{in}	12	AU
Outer radius	R_{out}	120	AU
Dust mass	M_d	1.8, 5.5	10^{-7} $M_\odot$
Optical	τ_V[a]	1.0, 3.1	aCSi
depth	τ_V	0.9, 2.9	GraSi
Clump	N_{cl}	0[b], 500, 1000, 2000,	
number		3000, 5000, 10000	

[a] Optical depths of the homogeneous shells of the respective dust masses.
[b] 0 corresponds to a homogeneous shell.

3.4 RESULTS

3.4.1 *Influence of clumps on extinction in circumstellar shells*

In order to study the influence of clumps on the effective extinction curve, the results of this treatment must first be benchmarked by comparing them to examples as found in the literature. Therefore, the effective extinction curves for clumpy spherical shells are computed, similar to those treated by Wolf et al. (1998). In this case each clump occupies one cell of the model grid. This grid consists of a cube containing $[nx, ny, nz] = [60, 60, 60]$ cells of equal size. The shell is completely described by its inner and outer radii R_{in} and R_{out}, the number of clumps N_{cl} and the total dust mass in the shell M_d. The range of parameters used is included in Table 1.

The N_{cl} clumps are distributed randomly throughout the volume of the shell by selecting cubes from the model grid; selected cubes will contain dust, and non-selected cubes remain empty[1]. The total mass of the shell is then normalised to the input value. As a result, one has a distribution of identical clumps of a given total mass.

As the clumps are randomly distributed, a large range of random seeds[2] must be explored for each model to be able to extract average behaviour, and to quantify the variations that could be seen between otherwise identical shells. As changing the distribution of clumps and changing the angle from which a clumpy shell are equivalent, the variations between models with different seeds can also be interpreted in terms of a change in the location of the observer relative to a fixed axis. An example of the density distribution of these shells can be seen in Fig. 10. For comparison, homogeneous shells are computed where R_{in}, R_{out}, and M_d are the same as in the clumpy cases. mass is fixed, models with fewer clumps have clumps of higher optical depths, which lie in the range $0.1 \leqslant \tau_{cl} \leqslant 30$, where τ_{cl} is the optical depth at V

1 To avoid the possibility of infinite loops for high N_{cl}, if the same cell is selected a second time, it will have its density doubled; if it is selected again it will then have triple the density, *et cetera*.

2 The random seed is the state used to initialise the random number generator's output. By changing this value between different models by significantly more than the number of random numbers required we obtain nearly independent streams of pseudo-random numbers.

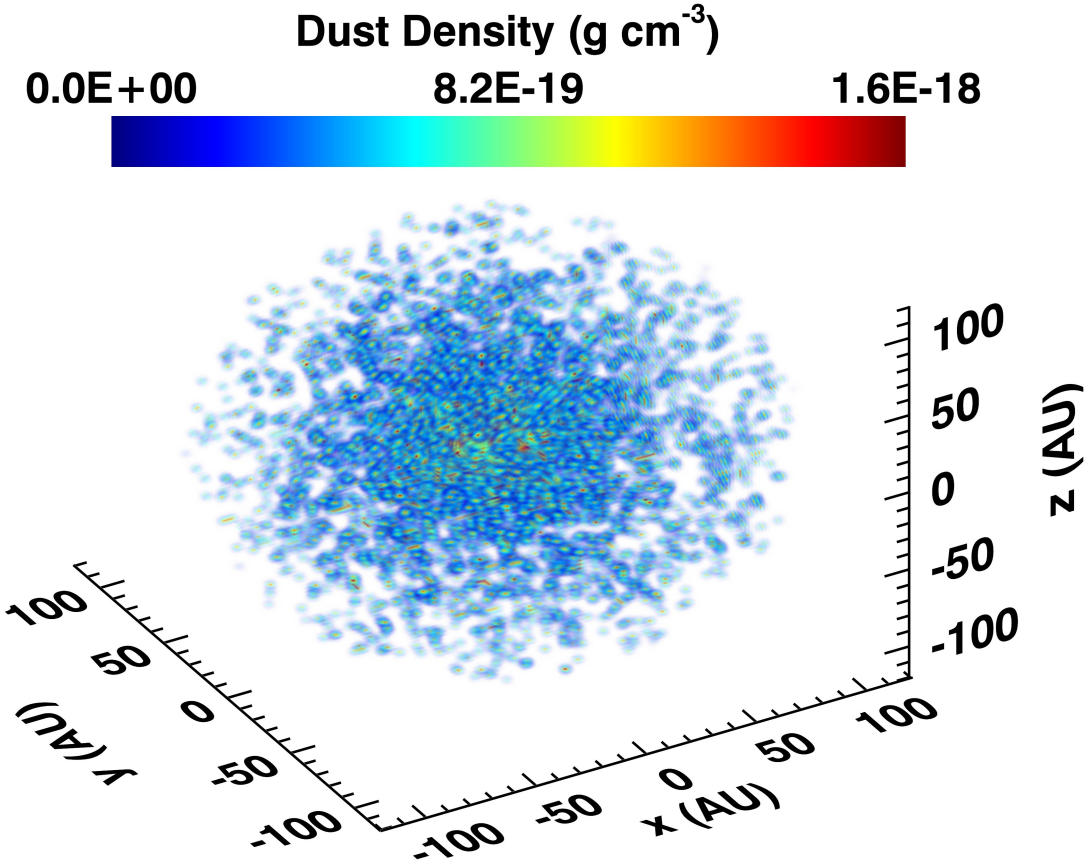

Figure 10: An example of the dust distribution in a clumpy shell shown in the 3D model volume. The source is located at the origin. While the colour indicates the dust density at a point, the opacity of the colours is related to the total column density. Upon close inspection it is clear that neighbouring clumps may connect to form filamentary structures.

band between two opposite faces of a clump. The extinction curves are computed by treating each face of the model cube as a large aperture (see Sect. 3.3), and are shown in Figs. 11–12.

As in Wolf et al. (1998), this model shows that shells that consist of optically thick clumps have generally flatter extinction curves than that given by the dust cross-sections, and in the most extreme cases the extinction curve can become completely grey (Figs. 11–12), in accordance with Natta and Panagia (1984). Furthermore, the homogeneous shells (and those with optically thin clumps) have extinction curves that are significantly steeper than that one would derive from the cross-sections, similar to the findings of Krügel (2009). When using the GraSi dust model to include the 2175 Å extinction bump, we see, as Natta and Panagia (1984), that as τ_{cl} increases, not only does the extinction curve flatten, but as in Natta and Panagia (1984), the feature is weakened and eventually flattened out (Fig.13).

However, the reader should note that in no case does the *shape* of the feature agree with the input dust cross-sections, regardless of whether the cross-sections are parametrised in terms of $K_{ext} = K_{abs} + K_{sca}$ or $K_{ext} = K_{abs} + (1 - g)\, K_{sca}$. In particular,

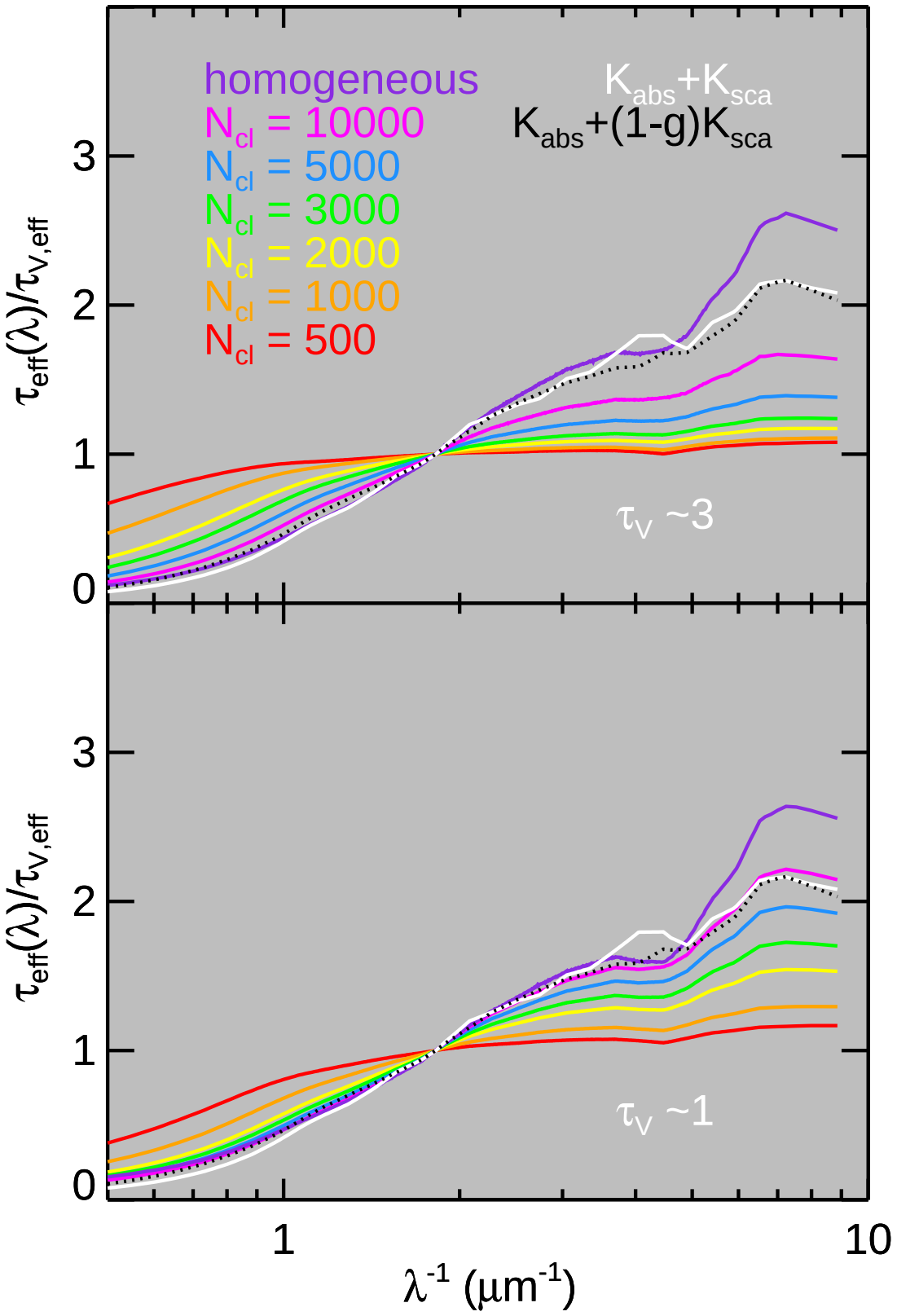

Figure 11: Effective extinction curves for clumpy circumstellar shells as a function of N_{cl} using the aCSi model. The line colours correspond to the models indicated in the top left. As the number of clumps decreases, the clumps become more optically thick and the effective extinction curve flattens. The white solid line shows the input dust cross–sections, and the black dashed line the same after a reduction in the scattering efficiencies by $(1 - g)$.

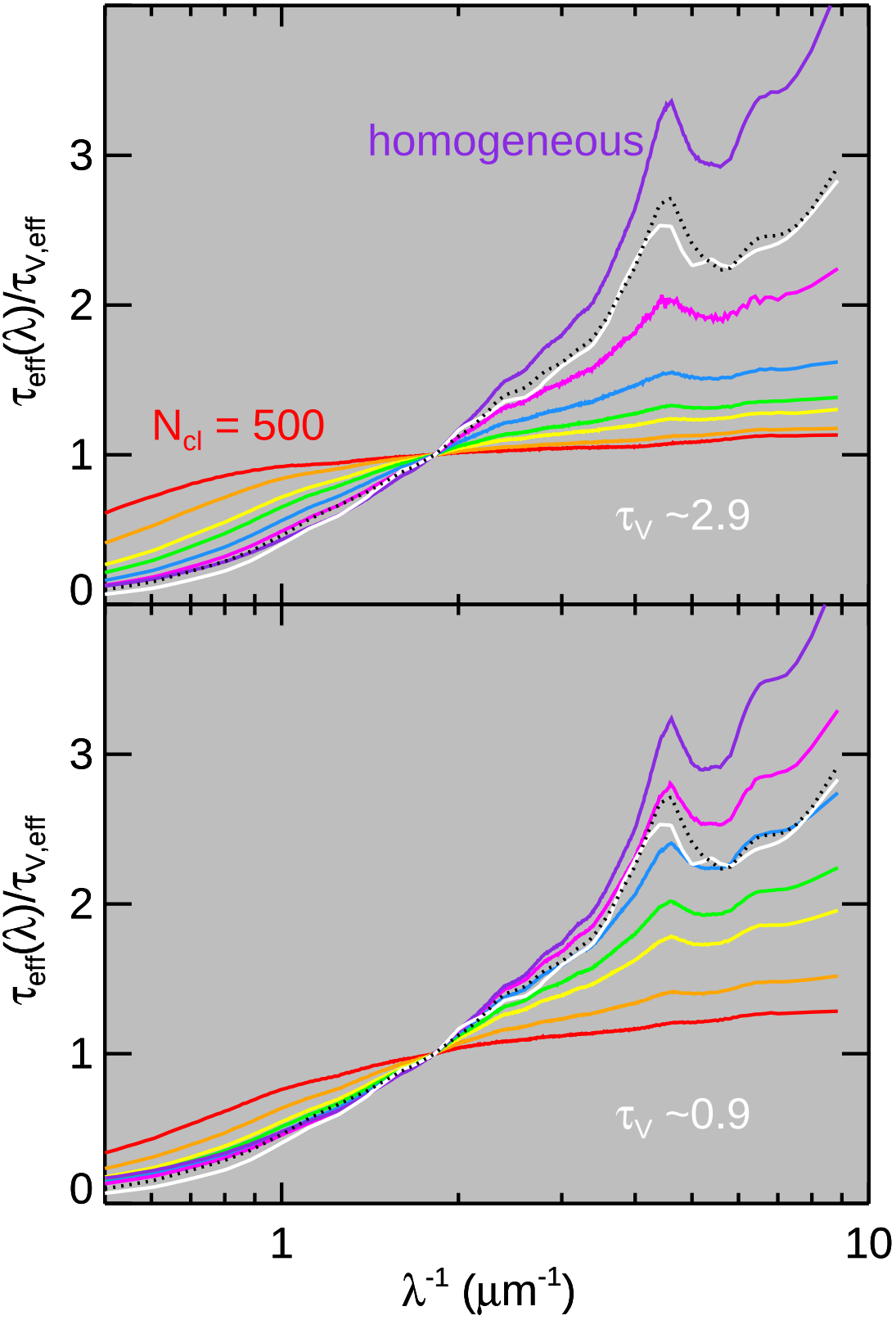

Figure 12: As in Fig. 11 using the GraSi model. The same effects occur with both dust models. In addition it is clear that the 2175Å feature is suppressed as the clump optical depth increases.

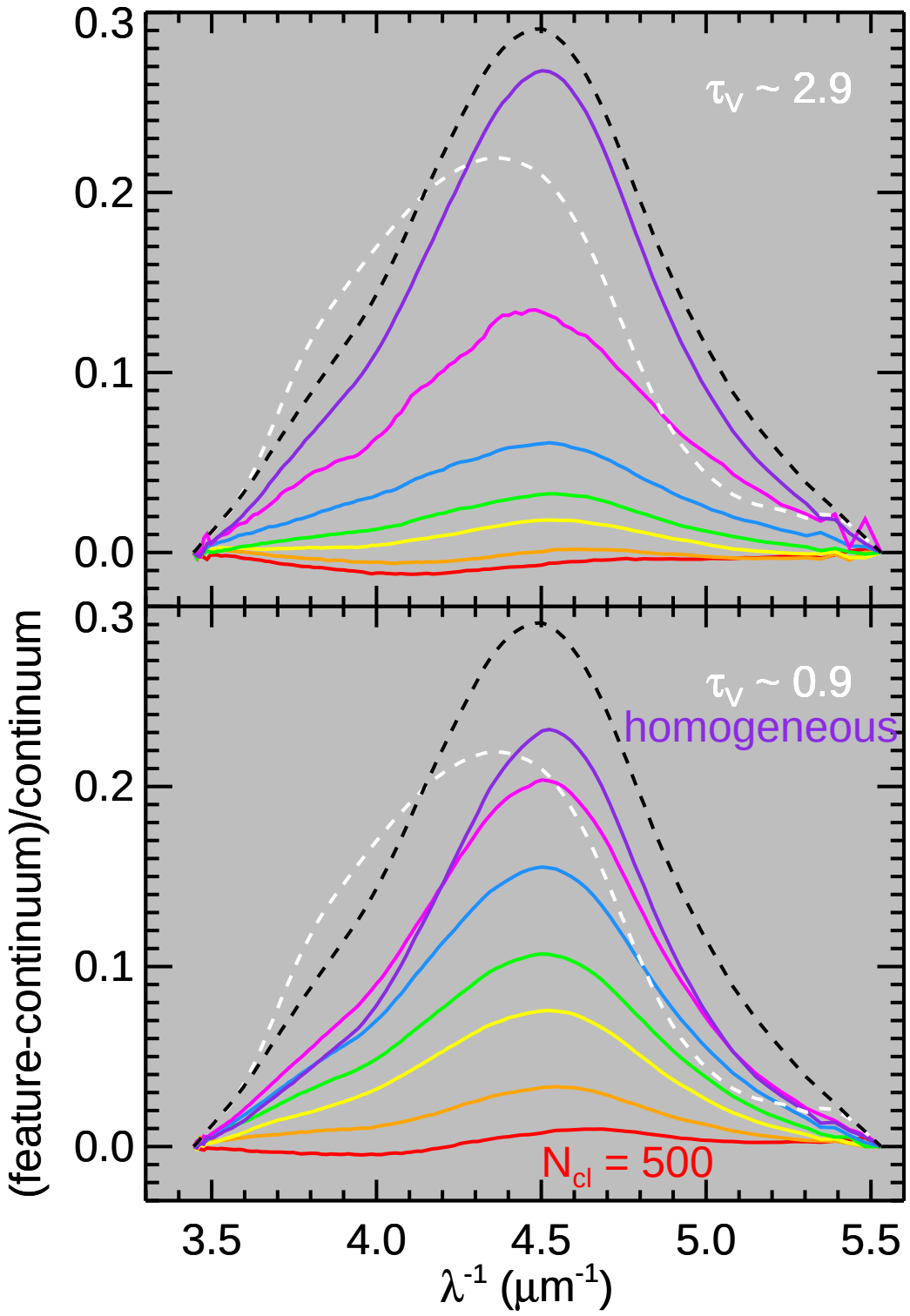

Figure 13: Fractional strength of the 2175Å feature of the effective exctinction curves shown in Fig. 12 (colours as in Fig. 11). On top of the suppression of the feature, it is apparent that the shape of the feature is different from that given by the input dust cross-sections.

the wavelength of the peak of the feature shifts, generally to shorter wavelengths, although there is no clear trend with N_{cl}.

Finally, the wavelength dependence of the extinction at $\lambda \geqslant 1\mu m$ tends toward parallel power-laws i.e. with the same gradient but offset in $\tau_{eff}/\tau_{V,eff}$ (Natta and Panagia, 1984). This may indicate that other indicators of extinction are preferable to those given in the V-band, e.g. normalised to the JHK or even L bands, provided that one is confident that the dust is sufficiently cold to neglect dust emission in these bands. Alternatively, one may be able to use the wavelength at which the infrared extinction deviates from a power-law to infer the optical depth of clumps in the medium. The wavelength at which this deviation occurs appears to be related to the optical depth of the clumps, with more optically thick clumps showing power-law behaviour at longer wavelengths where they become optically thin.

A number of differences exist between these models and those in the literature. Wolf et al. (1998) integrated the emergent flux over 4π steradians while we bin the extinction curve into directional apertures; as clumpiness naturally introduces some directionality to the shell, averaging over all directions neglects this. Contrary to the models of Natta and Panagia (1984), which treated the extinguishing medium as a clumpy screen, the use of a shell geometry results in the inclusion of back-scattering, which requires that directionality be included. Krügel (2009) on the other hand tailored their models to low optical depth clumps, neglecting the high clump optical depth cases included here.

3.4.2 *Light scattering by clumpy discs*

Having ensured that we reproduce the literature results concerning extinction in clumpy media which arise due to scattering, it may be of interest to consider the influence of clumpiness on the observation of scattered light itself.

To investigate this, models in which the view of the source is unobstructed are required, so that the stellar contribution can be easily subtracted to leave only the scattered photons. Hence, circumstellar disc models are used, constructed in a similar manner to the circumstellar shells in Sect. 3.4.1, but allowing dust only within a given opening angle of the equator; regions above this are dust free. Their inner and outer radii are chosen to approximately match those observed for the Vega outer debris disc (80 and 200 AU, respectively) and include $0.1M_{\oplus}$ of dust using the aCSi model. The number of clumps and the opening angle of the disc, α, are treated as free parameters. One such example can be seen in Fig. 14. The effective extinction is then measured for an observer seeing the disc face-on but unresolved.

As the observer's view of the star is unobstructed, the effective optical depth is negative for all wavelengths, due to the addition of the scattered photons to the stellar emission. The wavelength dependence of this negative extinction(= scattered flux) can be interpreted to yield information concerning the scattering properties of the dust. However, as seen in Fig. 15, the presence of clumpy structure alters the wavelength dependence of the scattered light, making the deduction of the scattering properties an unreliable process. Although Fig. 15 shows only one disc opening angle (in this case 45°), the same behaviour is seen for all opening angles between 5 and 45°.

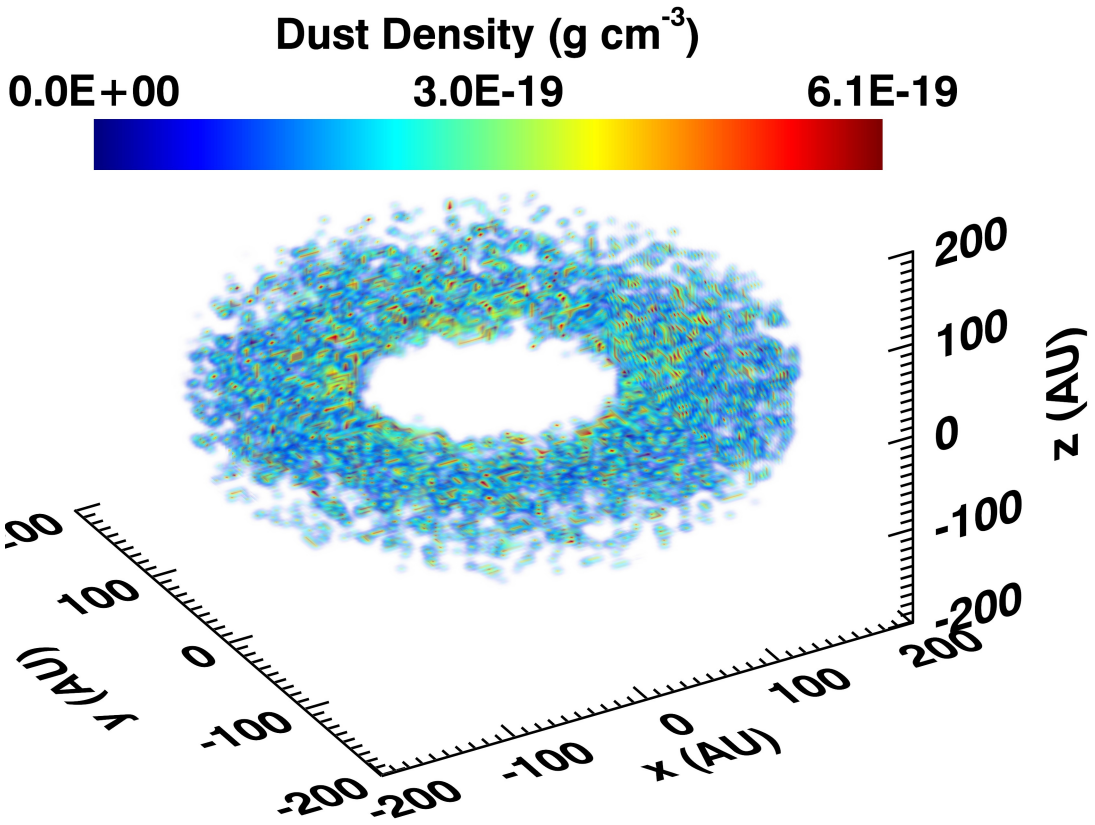

Figure 14: Similar to Fig. 10 but showing an example of the dust density distribution in a clumpy disc model.

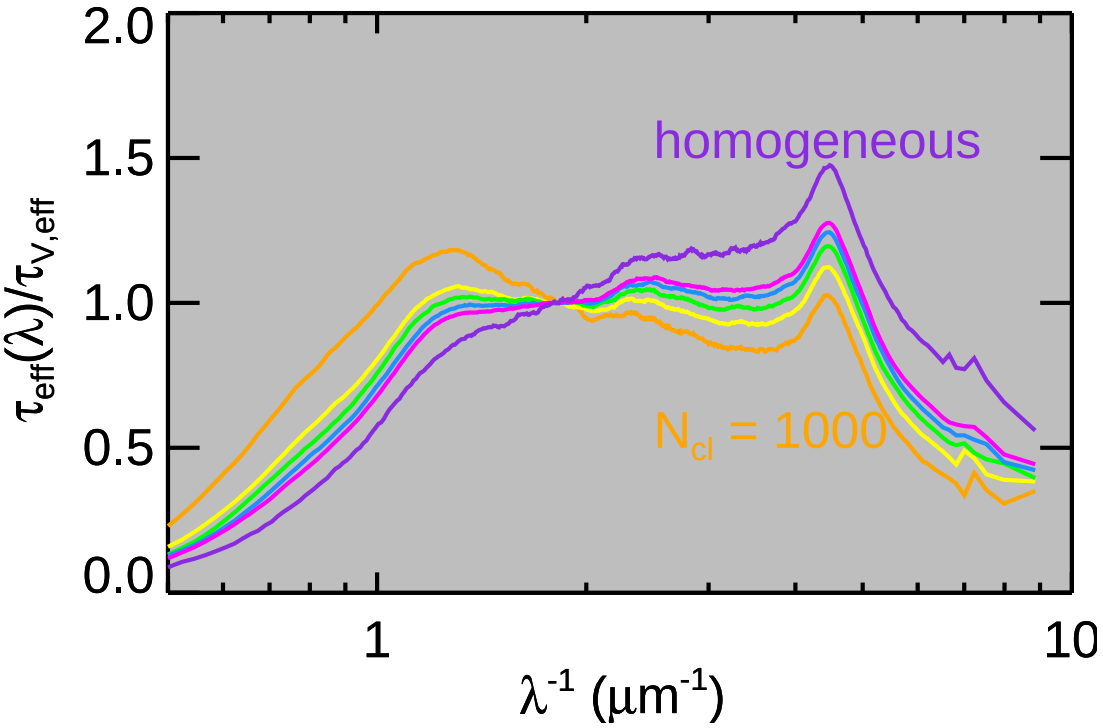

Figure 15: Effective extinction curves of face-on discs with an opening angle of 45°, computed for aCSi dust. The colours are again the same as in Fig. 11. The feature at ~ 4 – 5—m^{-1} does not change while the continuum scattering shows significant changes in the optical and UV.

It is clear that as the clumps become increasingly optically thick, the scattered light in the UV continuum is suppressed compared to the optical. The strong peak at ~ 2000 Å that is visible in Fig. 14 should not be confused with the 2175 Å extinction bump. It is created by scattering, coincides with the maximum of K_{sca} (see Fig. 9) and is not affected by the UV absorption. Therefore the feature is unaffected by the optical depth of the clumps. Conversely, because of stronger absorption in the optical and UV, the scattered flux in the NIR domain is enhanced relative to the optical. Due to their clumpy structure, there may be unobstructed sight-lines to regions deep within the disc. Clumps at such locations can then scatter photons into the observer's line-of-sight, but before escaping may encounter further clumps. Since the clumps are optically thick at shorter wavelengths, they would preferentially absorb optical/UV photons, while the NIR photons have a significantly higher escape probability. Since the strength and wavelength of the aforementioned scattering peak are functions of the size and chemical composition of the dust grains (see e.g. Hofmeister et al., 2009) and highly model dependent, it may be possible to infer the degree of clumpiness of a disc with sufficiently precise measurements of the integrated scattered flux at NIR, optical and UV wavelengths, and comparing the shape of the scattered continuum to any features observed.

If the relative enhancement of infrared scattering continues at wavelengths as long as 5µm then it may represent a source of contamination to the observations of "core-shine" (Steinacker et al., 2010), which are used to infer the presence of large grains in molecular cloud cores. Steinacker et al. (2010) report excess scattered flux in

Spitzer/IRAC (Fazio et al., 2004) bands 1 and 2 (at 3.6 and 4.5μm, respectively) toward dense regions ($A_V \geqslant 10$), while the longer wavelength bands show only absorption in the most dense parts of the clouds. In principle, it is possible that dense clouds consist of many small, dense clumps that are not resolved in the observations, and if so the effective scattering behaviour would be modified, resulting in the apparent increase in infrared scattering.

Similarly to Sect. 3.4.1, one can also explore the effect of extinction when the star is viewed through the disc. Different optical paths through the disc will have radically different covering fractions of clumps, with paths through the mid-plane fully covered and lower covering fractions when the disc is viewed at lower inclination angles.

As expected, the extinction curve through an edge-on clumpy disc exhibits the same behaviour as that for a clumpy shell (e.g. Siebenmorgen et al., subm.). This remains the same as long as the entire beam is within the disc (i.e. approximately when $i \geqslant 90 - \alpha$). However, for grazing and near-grazing inclinations, the behaviour of the extinction curve becomes chaotic, due to the complexity of the scattered radiation field. This effect is a major concern for studies of extinction towards e.g. AGN tori, where the extinction seen through the torus will bear little resemblance to the wavelength dependence of the dust properties. These results specifically indicate that studies which infer large grains in the circumnuclear medium (e.g. Maiolino et al., 2001; Lyu et al., 2014) have to consider the possibility of significant contamination from radiative transfer effects.

3.4.3 *Extinction in a clumpy diffuse ISM*

The ISM is believed to be a highly turbulent, inhomogeneous medium with structure on all scales in both the dense and diffuse phases (e.g. Vazquez-Semadeni, 1994; Padoan et al., 1997; Passot and Vázquez-Semadeni, 1998). It is therefore interesting to consider whether the effect of clumps on extinction as described above in Sects. 3.4.1 and 3.4.2 also influence extinction in the diffuse galactic ISM.

The previous two subsections have examined scenarios in which star and dust are co-located relative to the observer, but to examine the influence of scattering on extinction in the diffuse galactic ISM it is interesting to consider scenarios where the dust is distributed along the entire line-of-sight between the observer and the star.

To explore this, the ISM is modelled as a cuboid viewed along its long axis. This cuboid is homogeneously filled with dust, such that the optical depth in V-band from the observer to the star ranges from 0.3 – 20. Since this reproduces typical ISM optical depths, the interaction probability for each radiation packet is small. As a result, large numbers of packets must be computed ($\sim 10^9$) to achieve good statistics. To include the influence of back scattered as well as forward scattered photons, 5% of the model volume is behind the star as seen from the observer. The extinguished star is assumed to be at a distance of 100 pc, however as this is a resolution dependent effect the model space can be uniformly rescaled to greater distances. The model cuboid is scaled so that the cross-section is $50''$. We then solve the radiative transfer and generate images of both the scattered and emitted radiation by ray-tracing as outlined in Sect. 3.3. From the images we extract a $5'' \times 5''$ aperture in order to

Table 2: Clumpy ISM model parameters

Parameter		Values	Note
Dust mass	M_d	0.0058, 0.007, 0.009, 0.0115, 0.035, 0.058, 0.07, 0.09, 0.115, 0.35, 0.58	$M_\odot$
Optical depth	τ_V[a]	0.16, 0.2, 0.25 0.3, 1.0, 1.6, 1.9, 2.5, 3.2, 9.7, 16	GraSi
Clump number	N_{cl}	10, 50, 100, 500	–

[a] Optical depths (measured in the V band) of the homogeneous models of the respective dust masses.

approximately match the diffraction limited resolution of IUE, which remains the major source of UV data for extinction.

Contrary to the clumpy screen models of Fischera and Dopita (2005, 2011) the effect of back-scattering is included by embedding the source within the dust column. Instead of a homogeneous density distribution, clumps are distributed randomly throughout the model space with fixed volume filling factor f_V ~1.5% (Wolfire et al., 2003, Eq. 27) so that the free parameters are the total dust mass and clump number. The clump radii R_{cl} are calculated from the number and filling factor of clumps, such that all the clumps within each model are identical i.e.

$$R_{cl} = \left[\frac{3\, f_V \times x \times y \times z}{4\pi\, N_{cl}}\right]^{1/3} \tag{36}$$

where x, y, z are the dimensions of the model cuboid. As the clumps are randomly distributed, the random seed is once again varied to explore the parameter space created by the variations in the positions of the clumps.

Three different simple descriptions of the clumps are considered in these geometries:

1. Spherical clumps (1-phase) i.e. $\rho(R) = \rho_{cl}$ for $R \leqslant R_{cl}$, 0 elsewhere;
2. as above but with the clumps embedded in a diffuse medium (2-phase) i.e. $\rho(R) = \rho_{cl}$ for $R \leqslant R_{cl}$, $10^{-4}\rho_{cl}$ elsewhere;
3. Pressure-constrained isothermal clumps with

$$\frac{\rho(R)}{\rho_0} = \frac{1}{1 + \left(\frac{R}{R_{cl}}\right)^2} \tag{37}$$

to give a smoothly varying density distribution;

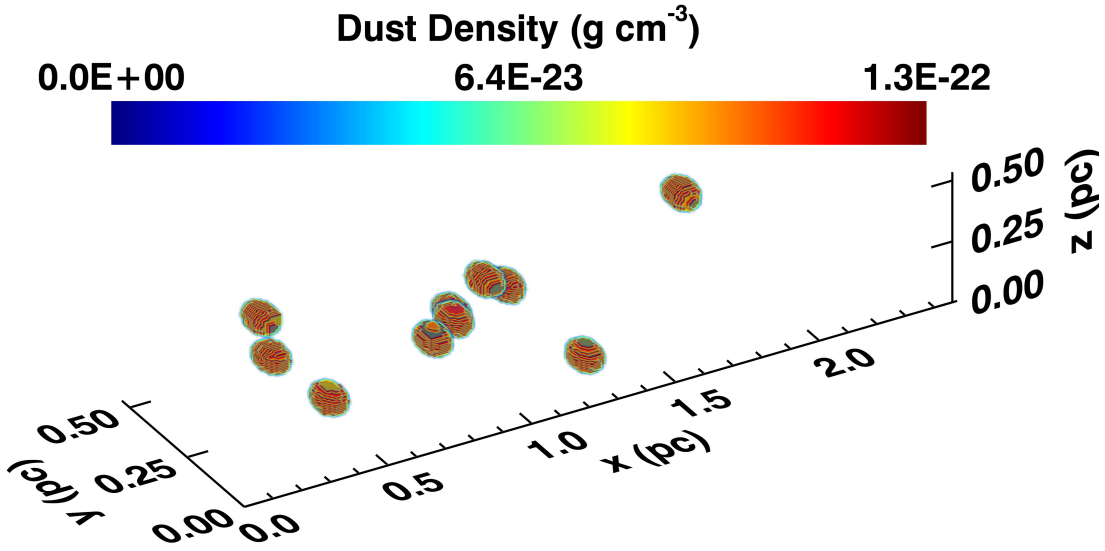

Figure 16: Example section from a 1-phase clumpy density distribution. The 2-phase distributions appear identical albeit with the intraclump space filled with a diffuse medium 10^{-4} times less dense than the clumps. This figure is constructed in a similar manner to Figs. 10, 14, but the source is no longer within this section of the model due to the extreme length of the cuboid. In the ISM models, the source is not placed at the centre, but at a point 95% of the length of the model cuboid. This section is that closest to the observer.

examples of which can be seen in Figs. 16, 17.

The results from the clumpy ISM models can be seen in Fig. 18. With the exception of a small fraction of outliers, the effect of clumpiness on extinction is negligible except at high optical depth. This suggests that on lines of sight that avoid the galactic centre, the effect of scattering can be neglected, and extinction can be reliably be used as a probe of the properties of interstellar dust, as expected from Panek (1983). The fact that the OB stars typically used to measure extinction tend to clear a large volume (several pc) surrounding them of interstellar matter through wind and radiation pressure further reduces the probability that interstellar extinction is significantly modified by scattering on distance scales of a few kpc.

3.5 DISCUSSION

From Sect. 3.4.1 it is clear that if the dust is concentrated in optically thick clumps, the extinction curve is artificially flattened. This has been previously highlighted by Natta and Panagia (1984), however, they did not attempt to derive a relationship between the flattening of extinction and the clump properties.

Figure 19 demonstrates the relation between this increase in the V-band optical depth of the clumps and $R_{V,\mathrm{eff}}$, using the results from Sect. 3.4.1 for both dust models.

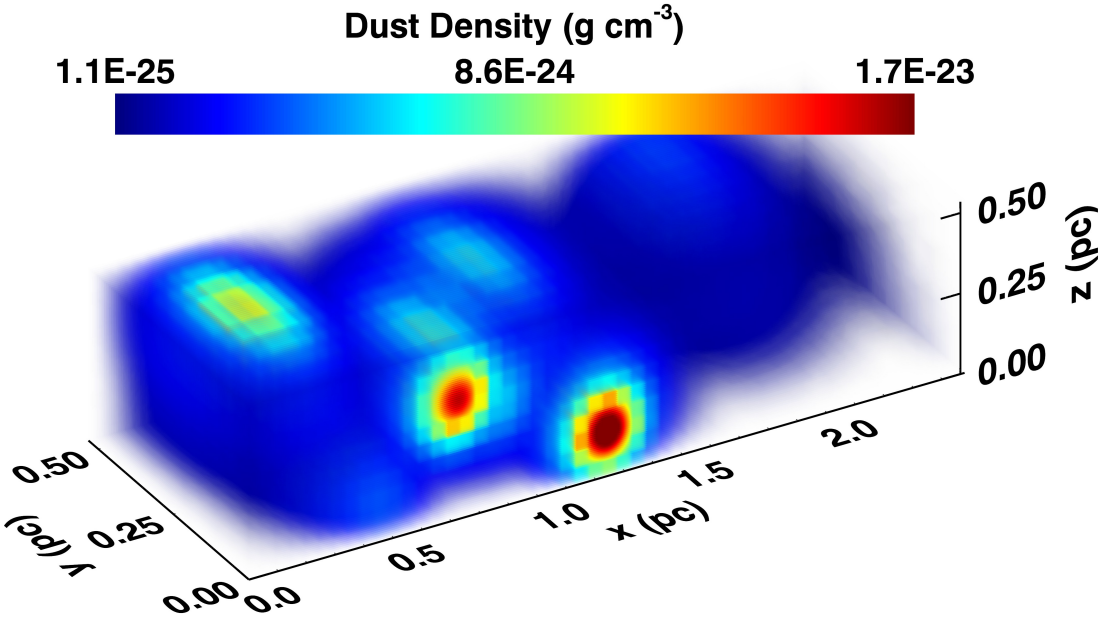

Figure 17: As in Fig. 16 but showing an example section from a pressure-constrained clump density distribution.

While it is clear that both dust models follow similar trends, they appear to form two separate sequences. The separation between these sequences is typically a few tens of percent.

Since the optical depth at an arbitrary wavelength is not directly related to the extinction curve, this should be transformed to a quantity that is. As the changes in the shape of the extinction curve result from wavelength-dependent optical depth effects, the quantity λ_{crit} is introduced, which is defined as the wavelength for which $\tau_{cl}(\lambda_{crit}) = 1$. When the change in R_V is plotted against this critical wavelength (Fig. 20) the two dust models overlap. The gradient is rather shallow for $\lambda_{crit} \leqslant 600\,\mathrm{nm}$ but steepens dramatically beyond this. As $R_{V,eff}$ is related to the B- and V-band optical depths, it stands to reason that clumps that are optically thin or only marginally optically thick to these wavelengths would only weakly affect the shape of the extinction curve, while clumps that are optically thick at even longer wavelengths will have a much stronger effect.

If the true R_V of the dust can be determined independently of the extinction measurements, then it is in principle possible to use the relation between $R_{V,eff}$ and λ_{crit} to infer the structure of the medium.

It is important to note that all the effects described in this paper will become more significant as the distance between the object and the observer increases, as structure will be ever more poorly resolved. Therefore, extragalactic observations are particularly susceptible, and even more so at high redshift. This means that studies that use AGN (e.g. Maiolino et al., 2001) or, in particular GRBs (Zafar et al., 2011) to probe dust properties must be especially careful to consider the role of radiative transfer effects.

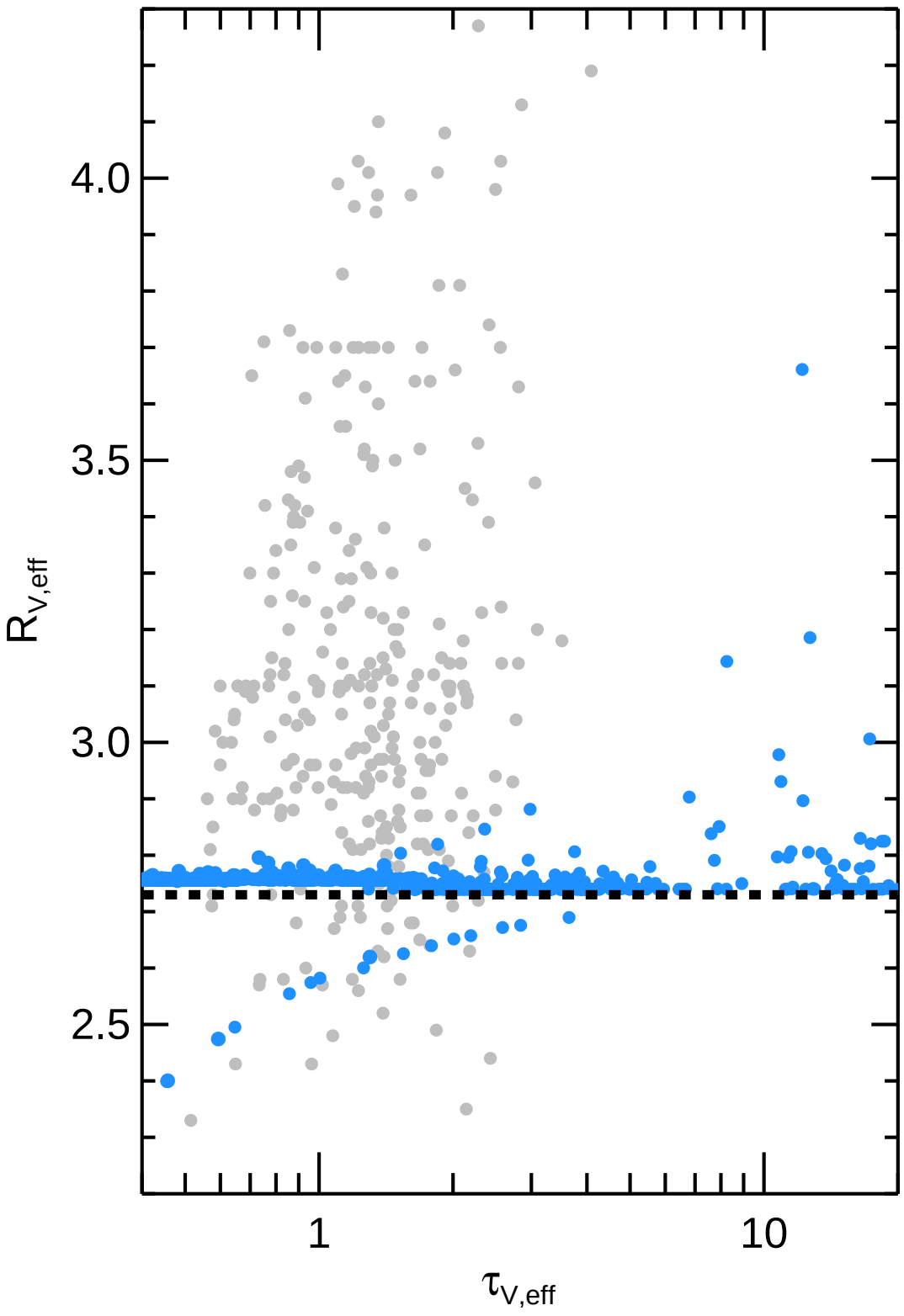

Figure 18: The range of $R_{V,eff}$ produced by clumpy ISM models. The models are indicated by filled blue circles. These are compared with the observed values of R_V reported in FM07 (gray full circles). The thick black dashed line indicates the R_V of the dust cross-sections. Except for a small fraction of outliers, which increases toward large optical depth, clumpiness has little effect on typical interstellar extinction curves.

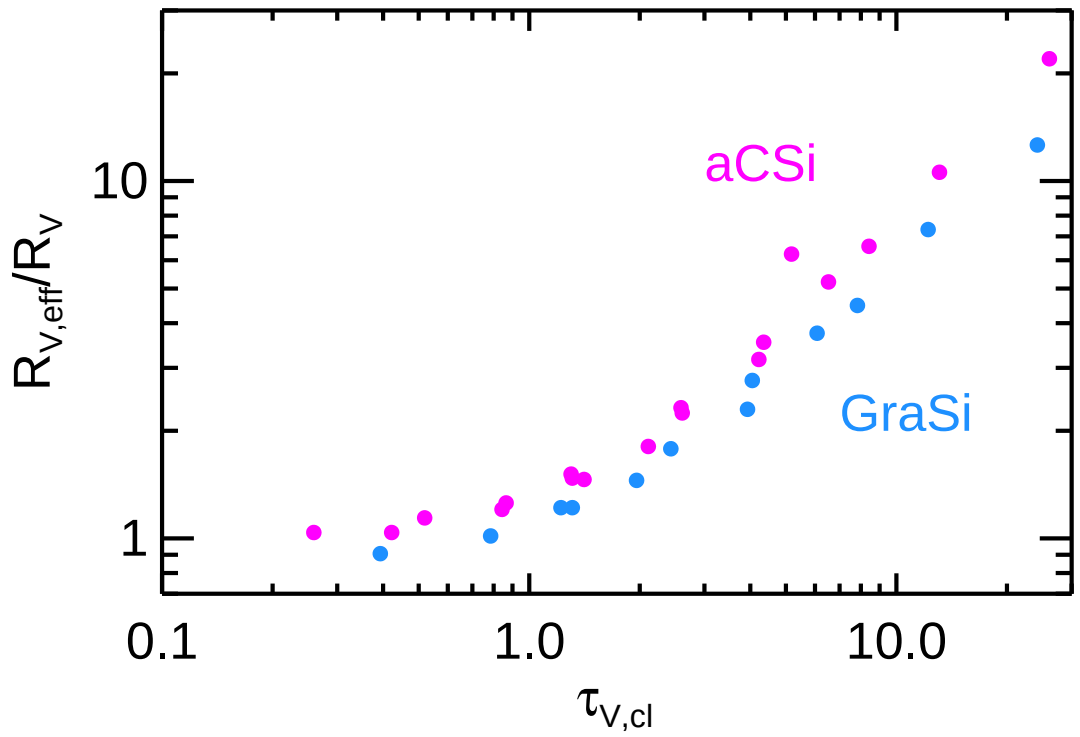

Figure 19: Evolution of the effective extinction curve in clumpy shells with the optical depth of the clumps for both dust models. While the two models show generally the same behaviour, there remains an offset (~ 20%) between the two.

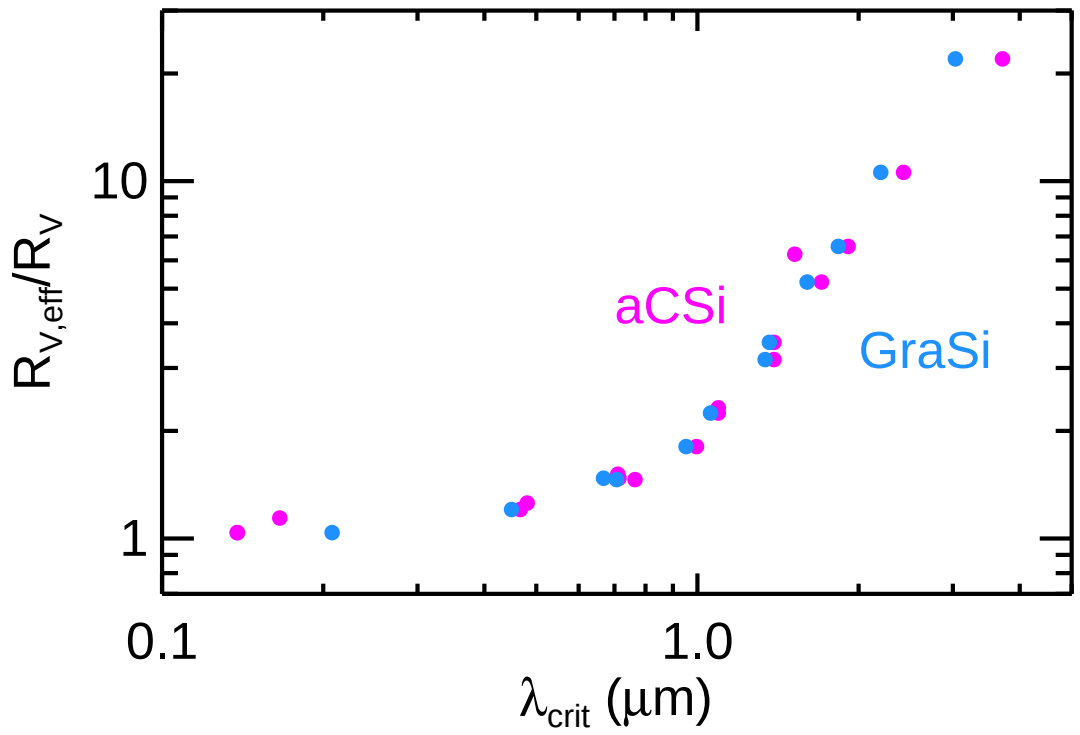

Figure 20: As in Fig. 19, but now comparing R_V to λ_{crit}, the wavelength at which $\tau_{cl} = 1$. The two previously disparate curves are now reconciled.

3.6 SUMMARY

Clumpy media and the collection of scattered light can fundamentally alter the observed extinction curve, which can significantly hinder the accurate interpretation of observations. In clumpy media the changes in the shape of the extinction curve are related not to the optical depth of the clumps but rather to the critical wavelength for which $\tau_{cl}(\lambda_{crit}) = 1$. If the true R_V is known, it is in principle possible to infer the structure of the medium from this relationship. Furthermore, there is a shift in the wavelength of the peak of the 2175 Å feature towards shorter wavelengths.

Similarly, the observed scattering behaviour of dust can be markedly different if the scattering medium is clumpy rather than homogeneous. More optically thick clumps lead to a suppression of the optical and UV scattered flux in the continuum, while scattering features are unaffected, potentially providing a means by which to constrain the structure of a scattering medium.

This chapter has shown that the collection of scattered photons represents a major challenge to measurements of extinction towards embedded objects, particularly in other galaxies e.g. AGN or GRBs, where large-scale structure is unresolved. As a result, there is not necessarily a 1:1 link between the extinction curve and the wavelength dependence of dust cross-sections.

4

OLD PRE-MAIN-SEQUENCE STARS - DISC REFORMATION BY BONDI-HOYLE ACCRETION

Young stars show evidence of accretion discs which evolve quickly and disperse with an e-folding time of ~ 3Myr. This is in striking contrast with recent observations that suggest evidence for numerous > 30 Myr old stars with an accretion disc in large star-forming complexes. This chapter considers whether these observations of apparently old accretors could be explained by invoking Bondi-Hoyle accretion to rebuild a new disc around these stars during passage through a clumpy molecular cloud. A simple Monte Carlo model to explore the capture of mass by such systems is combined with a viscous evolution model to infer the levels of accretion that would be observed. This reveals that a significant fraction of stars may capture enough material via the Bondi-Hoyle mechanism to rebuild a disc of mass $\gtrsim$ 1 minimum-mass solar nebula, and $\lesssim$ 10% accrete at observable levels at any given time. A significant fraction of the observed old accretors may be explained with the proposed mechanism. Such accretion may provide a chance for a second epoch of planet formation, and have unpredictable consequences for planetary evolution.

Material in this chapter is adapted from:
P. Scicluna, G. Rosotti, J.E. Dale & L. Testi; A&A, 566:3L, June 2014.

4.1 INTRODUCTION

Circumstellar discs form around protostars as a result of angular momentum conservation during gravitational collapse (e.g. Shu et al., 1987). In the early phases of star formation, disc material loses angular momentum and is accreted onto the central star. The most direct observational signature of the presence of a protoplanetary disc is the excess emission, on top of the expected naked stellar photosphere, at infrared and millimetre wavelengths, in the ultraviolet and in optical/infrared emission lines. The long wavelength emission is produced by a dusty disc, heated by internal dissipation processes or reprocessing of stellar radiation (e.g. Dullemond et al., 2007). The short wavelength excess and the optical/infrared emission lines are thought to be produced by the disc-star interaction as matter accretes onto the star or is ejected in a wind/jet (Hartmann, 2009). Strong observational evidence shows that both the inner dusty disc and accretion onto the central star quickly disappear during the early stages of pre-main-sequence evolution; the fractions of stars with near infrared excess and with accretion signatures decay with an e-folding time of 2-3 Myr (Fedele et al., 2010; Hernández et al., 2007). This disc dissipation timescale, even considering the possible revision by Bell et al. (2013), sets a stringent constraint on the timescales for planet formation.

Recent work has challenged this paradigm. Sensitive, wide field Hα surveys of large star-forming complexes in the Magellanic Clouds and our own Galaxy have revealed a population of pre-main-sequence stars that appear to be older than 10 Myr but still show prominent Hα emission and/or infrared excess (Beccari et al., 2010; De

Marchi et al., 2013a, 2011a,c, 2013b). Although some of these old accretor candidates in nearby star-forming regions have been shown to be misclassified young stellar objects (Manara et al., 2013), it is difficult to believe that this is the case for all the candidates; these populations of old accretors are not as centrally condensed as the young stellar clusters in the same fields (e.g. De Marchi et al., 2011b). If the line emission is interpreted as due to accretion as in young pre-main-sequence stars, the implied accretion rates are similar to those derived at early ages, and typically higher than nearby transitional discs[1]. These findings are hard to understand in a framework in which the primordial disc is still the reservoir of accreting material at such old ages; even one disc of age $> 30\,\mathrm{Myr}$ implies an initial population $> 10^5$ (assuming exponential decay with an e-folding timescale of 3 Myr).

This chapter explores the possibility that the old accretors do not have a primordial disc, but a disc that they re-accreted after the primordial disc had dissipated. Previous studies (Moeckel and Throop, 2009; Padoan et al., 2005; Throop and Bally, 2008) have investigated the influence of Bondi-Hoyle accretion on pre-main-sequence mass-accretion rates and the protoplanetary disc at earlier phases, during the initial evolution of the disc-star system within the progenitor cloud. Here we investigate the possibility that a star older than 5–10 Myr happens to travel through a clumpy molecular cloud, typically unrelated to that in which the star formed, and is able to accrete enough material to form a new accretion disc.

4.2 MODELLING

4.2.1 *Bondi-Hoyle accretion*

Hoyle and Lyttleton (1939), Bondi and Hoyle (1944) and Bondi (1952) proposed a mechanism by which objects can capture matter from the interstellar medium. A massive object moving through the ISM causes a perturbation, pulling material toward the object. As the capture of material is roughly symmetrical with respect to the direction of motion of the star, much of the angular momentum of the material cancels out, and hence it is captured by the star to eventually be accreted (Davies and Pringle, 1980).

The rate at which material is captured is given by

$$\dot{M}_{BH} = \mu n v \pi R_{BH}^2, \tag{38}$$

where v is the relative velocity between the star and the ISM, n is the number density of the ISM, and μ is the mean molecular weight (usually taken as $2.3 m_H$). The gravitational cross-section is given by πR_{BH}^2, where R_{BH} is the Bondi-Hoyle radius

$$R_{BH} = \frac{2GM_*}{v^2 + c_s^2}; \tag{39}$$

c_s is the sound-speed of the ISM, typically $0.3\,\mathrm{km\,s^{-1}}$. For a $1 M_\odot$ star moving at $1\mathrm{km\,s^{-1}}$, $R_{BH} \sim 1500$ au.

To explore the effect of this process in reconstituting discs around young stars, a simple Monte Carlo model is constructed to treat interactions between stars and

1 although these are systematically lower mass objects

Table 3: Parameters for Monte Carlo models

Parameter	Values	Parameter	Values
f_V	$10^{-2}, 10^{-3}, 10^{-4}, 10^{-5}$	c_s	0.3 km s^{-1}
N_{stars}	$10^5, 10^5, 10^6, 10^7$	σ_v	1 km s^{-1}
R_{cl}	0.1 pc	α	2.35
n_{cl}	10^4 cm^{-3}		

clumps with densities typical for molecular clouds. We assume a stationary clumpy molecular cloud, which we model as a collection of identical spherical clumps with radius R_{cl} and density n_{cl}. The density of clumps is parametrised through a volume filling factor of dense gas f_V. The model assumes a population of "old" young stars that has lost their primordial disc enters the cloud and moves through the clumpy medium. By randomly generating stars with masses between 0.7 $M_\odot$ and 3.2 $M_\odot$[2] from a Salpeter Initial Mass Function (IMF) ($M \propto M^{-\alpha}$ Salpeter, 1955) and velocities generated assuming a velocity dispersion of $\sigma_v = 1$ km s^{-1}, the parameters required in Eq. 39 are sampled from the values given in Table 3. The model simulates 10 Myr treated as a series of quasi-static time steps of length $t_{st} = 2R_{cl}/v_*$, assuming that each star is independent. For each star, we calculate R_{BH}, the volume swept out per time-step $V_{st} = v_* t_{st} \times \pi (R_{cl} + R_{BH})^2$, and hence the probability of encountering a dense clump

$$p = \frac{V_{st} \times f_V}{(4/3)\,\pi R_{cl}^3}. \tag{40}$$

In each time-step a uniform random number ζ is drawn, and the star encounters a clump when $\zeta \leqslant p$; the impact parameter b of the encounter is given by drawing a second random number ζ_2 from the same generator such that $b = (R_{cl} + R_{BH})\,\zeta_2^{1/2}$. We then determine the accretion rate (Eq. 38) and resolve the stellar accretion and the clump-mass depletion on a finer time-grid of 1000 sub-steps to accurately determine the accreted mass. Interactions where $R_{BH} > R_{cl}$ and grazing encounters are treated correctly by taking the projected area of intersection. By repeating this process for $> 10^5$ stars we build up meaningful statistics about the range of possible BH accretion histories and their probabilities. Note that each star is modelled independently, and mass accreted by a star does not influence the mass-budget available to later stars.

The accretion histories determined by this model are then passed to a viscous evolution model (Sect. 4.2.2) to estimate the rate at which material is accreted by the star.

The choice of f_V is based on a reanalysis of smoothed–particle hydrodynamics simulations of star-forming regions including feedback mechanisms presented in Dale et al. (2012, 2013) to determine the filling factor of gas at densities higher than 10^4 cm^{-3}. We find that for bound clouds of similar stellar mass to the regions ob-

2 Stars above ~ 3 $M_\odot$ have strong winds which make a simple model inappropriate, while observations of old accretors are incomplete for stars below 0.7-1 $M_\odot$ depending on the distance to the observed region.

served by Beccari et al. (2010); De Marchi et al. (2013b), $10^{-6} < f_V \lesssim 10^{-3}$ irrespective of whether feedback from massive stars is included.

While this provides a useful estimate of the amount of mass captured in this way, it somewhat overestimates the total as a number of physical processes are neglected. First, we neglect the motion of the clumps and assume that $v = v_*$ in Eq. 39. Correct treatment of the relative motions would in general reduce R_{BH} and hence the accretion rates. Second, stars above $2M_\odot$ have significant wind and radiation pressure that will depress the accretion rate (Edgar and Clarke, 2004). Similarly,the possible influence of the X-ray photoevaporation on the accretion is not treated, which may have an analagous effect for lower mass stars. The possible influence of magnetic fields is also not included, which recent studies (e.g. Lee et al., 2014) have shown may reduce accretion rates by a factor of a few. Likewise, structure on scales smaller than a single clump is neglected; such structure is required for a disc to form, and would reduce accretion rates relative to the homogeneous clump case treated here. Finally, we do not include binaries. However, the only influence of binarity in the context of Bondi-Hoyle accretion is to increase R_{BH}, since binaries behave as a single object of mass $M = M_1 + M_2$.

4.2.2 *Viscous evolution modelling*

Due to the angular momentum of the material accreted from the clump, which may be due to a density gradient within the clump or the rotation of the clump itself, accretion cannot proceed directly onto the star (Ruffert, 1997). Therefore, the formation of a thin accretion disc is expected as the result of the viscous spreading of a thin ring. Throop and Bally (2008) described the "buffering" effect of an accretion disc, but did not directly model it. The material accreted from the medium is assumed to circularise at a radius $r_0 = 0.1R_{BH}$. After a single impulse of accretion onto the disc, the surface density is described by $\Sigma(r) = M_0/(2\pi)\delta(r - r_0)$, where M_0 is the deposited mass. Under the influence of an effective viscosity ν that redistributes the angular momentum in the disc, the spreading ring solution (Lynden-Bell and Pringle, 1974) describes the evolution in time of this initial surface density,

$$\Sigma(r,t) = \frac{GM_*(rr_0)^{1/4}}{3\pi r^2 \nu\Omega} \exp\left[-\left(\frac{(r_0^{1/2} - r^{1/2})^2 r}{3t\nu}\right)\right] \exp(-\lambda) I_{1/2}(\lambda), \tag{41}$$

where ν is the kinematic viscosity of the gas, Ω the keplerian angular speed, $I_{1/2}$ the modified Bessel function of order 1/2, $\lambda = 2r^{3/2}/(3(GM_*)^{3/2}\nu t r_0)$, and we have specialized the expression for the $\nu \propto r$ case. From this analytical solution, it is possible to compute the mass accretion rate onto the star $\dot{M}_{kernel}$. To derive the mass–accretion rate of the star as a function of time, we convolve this function with the mass–accretion–rate history of the disc:

$$\dot{M}_*(t) = \int \dot{M}_{BH}(t')\dot{M}_{kernel}(t - t')dt'. \tag{42}$$

Given a stellar mass, the loading radius, and a law for viscosity, the evolution in time is now completely determined. The viscosity is fixed using the well-known Shakura and Sunyaev (1973b) prescription, $\nu = \alpha(h/r)^2 r^2 \Omega$, where α is the Shakura–Sunyaev parameter and h/r the aspect ratio of the disc, using typical values of $\alpha = 0.01$ and

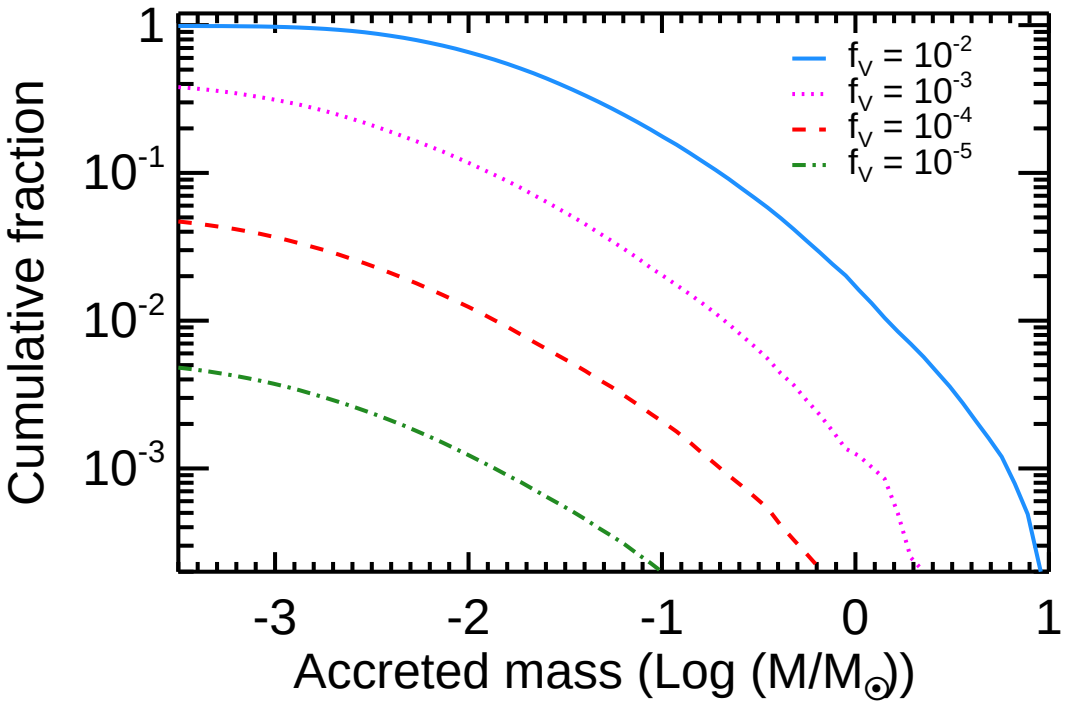

Figure 21: Cumulative fraction of the stellar population that has accreted mass as a function of total accreted mass. The solid blue line indicates a filling-factor of 10^{-2}, the dotted magenta line 10^{-3}, the dashed red line 10^{-4}, and the dot-dashed green line 10^{-5}.

$h/r = 0.05(r/1AU)^{1/4}$ (Armitage, 2011). Equation 41 is sampled numerically on a space and time grid. Integrating over the spatial extent yields the mass of the disc, and numerically differentiating the result provides the mass–accretion–rate kernel, which can be convolved with the Bondi-Hoyle history (Sect. 4.2.1).

4.3 RESULTS

The model indicates that a fraction of the population $\sim 40 - 50 \times f_V$ encounter dense regions and accrete more than $0.001\,M_\odot$ material by the end of the simulation (Fig. 21). The median accreted mass is typically $\sim 0.01\,M_\odot$, similar to the mass of discs around young pre-main-sequence stars, with strong dependence on the stellar mass. In extreme cases, however, more massive stars ($>2\,M_\odot$) with low v_* that encounter several clumps can capture $\geqslant M_\odot$. Our treatment of the disc formation and evolution is probably inadequate for these extreme cases.

Converting the Bondi-Hoyle accretion into stellar accretion rates, we find $\dot{M}_* \lesssim 10^{-6}\,M_\odot\ \mathrm{yr}^{-1}$ after the formation of the disc. Owing to the assumptions inherent in our model, this rate declines from the peak as a power law as in primordial discs.

By calculating the time each star spends accreting above a certain threshold accretion rate, one can derive a mean time per star as a function of the threshold and hence an estimate of the fraction of the population which one expects to observe accreting at a given time. As shown in Fig. 22, for a threshold rate of $10^{-8}\,M_\odot\,\mathrm{yr}^{-1}$ we typically find that the cumulative probability is $\sim 20 f_V$, i.e. the fraction of a stellar

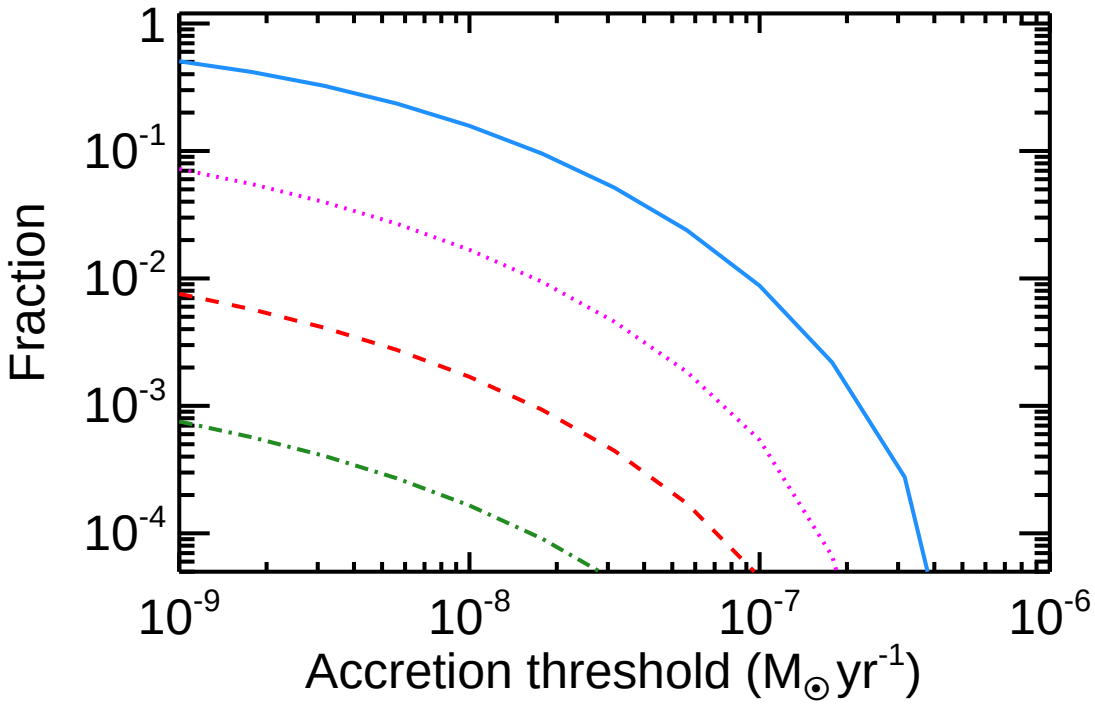

Figure 22: Fraction of the population that would be detected as an old accretor at a given time, plotted as a function of the instantaneous accretion rate. The models are indicated using the same colours and line-styles as Fig. 21.

population that one expects to observe as old accretors at a given time is an order of magnitude larger than the volume filling-factor of dense clumps.

4.4 DISCUSSION

The primary goal of this study is to assess whether the Bondi-Hoyle mechanism can contribute significantly to observations of old accretors in regions with ongoing star formation, under a number of simple assumptions. This involves stars from a previous star-formation episode, after their primordial discs have dispersed, interacting with a clumpy molecular cloud. The model indicates that up to several percent of the population passing through a region containing dense clumps may accrete more than 0.001 $M_\odot$ of material. Because of the factors indicated above (Sect. 4.2.1), the model is likely to overestimate the total accreted mass. However, since Bondi-Hoyle accretion is a well-understood process, the largest sources of uncertainty derive from the parameters assumed as input to the model, and in particular the clump geometry and filling factor, as well as the assumption that the accreted material will form a thin disc.

The initial choice of filling factor was based on a reanalysis of the simulations of Dale et al. (2012, 2013) for clouds similar to those observed to host old accretors. A further estimate can be obtained from the high-resolution sub-mm maps of the 30 Dor region from Indebetouw et al. (2013). These reveal a wealth of clumpy structures, similar in scale and density to the clumps in the Monte Carlo model used here. Assuming that the clumps are uniform spheres with an average radius $R_{cl} = 0.15$ pc

and distributed in a cube whose depth is equal to the projected size of the observed region ($10 \times 10 \times 10$ pc^3) yields a filling factor of $f_V = 1.5 \times 10^{-3}$, at the upper end of our parameter range.

The behaviour of the accretion disc depends strongly on the viscous timescale τ_ν, as parametrised in terms of r_0 and α. An order of magnitude change in τ_ν has little effect on the observable old-accretor fractions at low thresholds, but the fractions at high thresholds decline approximately in proportion to $1/\tau_\nu$. For larger changes in viscosity, this also affects the lowest thresholds explored in Sect. 4.3

Since we do not include stars down to the peak of IMF ($\sim$0.3 $M_\odot$) and Bondi-Hoyle accretion rates are $\propto M^2$, we may overestimate the total fraction of old accretors by a factor ~ 3 for the Salpeter IMF assumed here. However, Eq. 40 is dominated by R_{cl} for low-mass stars, so one would expect a similar fraction of old accretors when $\dot{M}$ is a factor of 4 lower.

Comparisons between our model and the observations of old accretors are difficult, as there are no firm constraints on the size of the old population (including non-accretors). Nevertheless, from Fig. 22 one can see that without an unrealistically large filling factor ($\gg 10^{-3}$) of dense clumps, the small, nearby star-forming regions are unlikely to produce more than one old accretor, as their typical mass is a few hundred $M_\odot$. As no old accretors have been identified in these regions, this is consistent with our model. From the recent identification of a large ($\sim 3 \times 10^3$ $M_\odot$) diffuse population with ages $\gtrsim$ 10 Myr toward Orion (Bouy et al., 2014) one expects a few tens of reformed discs, although it is unclear whether there is any overlap between this population and the Orion molecular clouds.

Observations of old accretors in large star-forming complexes typically detect up to several hundred such sources in each observed region. Given the formation efficiency we have computed and the assumed filling factors, this requires a total population at least of the order of 10^4 stars in the mass range of the observed old accretors, or $\sim 3 \times 10^4$ stars correcting for the IMF, which must have passed through the regions in which the clumps are distributed. In the case of NGC3603, which is inferred to have a population $\sim 10^{4.2} M_\odot$ (Rahman et al., 2013) and $\sim$ 100 old accretors, this implies either that the old population was significantly richer, or that f_V is or was very high. The 30 Doradus region, on the other hand, shows a similar total of old accretors, although the total population is likely $\sim$ 100 times larger than NGC3603. Only a small fraction (1%) of the stars in 30Dor need to pass through regions containing dense clumps to produce the observed numbers. In reality, f_V will evolve with time, and it is possible that the difference we observe between these regions may be due to 30Dor being more evolved, or having evolved more rapidly, than NGC3603.

In this model, a significant fraction (up to several tens of percent) of stars capture enough material to form a circumstellar disc of mass similar to primordial protoplanetary discs. This raises a number of interesting questions, such as whether a second epoch of planet formation is possible, and how the interaction between inflowing material and an existing planetary system might alter the accretion or the planetary evolution.

The answers to these queries depend strongly on how the inflowing material interacts with the existing system, which we have not treated. Nevertheless, Bondi-Hoyle accretion presents a mechanism by which a new reservoir of potentially planet-forming material may be built by up to a few percent of stars. This gives them a

second chance to form planets, from material that is potentially of different composition from the material that formed the star. Another possibility is that these stars are already surrounded by a planetary system formed out of the primordial disc. If they accrete new material, typically with an angular momentum different from that of the original planetary system, the interaction of the new material and the existing planets may have a range of outcomes. Understanding the range of possible outcomes will require detailed simulations of the accretion process and of the dynamical interactions with the planetary systems which are beyond the scope of the present work.

4.5 SUMMARY

This chapter has presented a model in which Bondi-Hoyle accretion by stars passing through dense clumps in the outer regions of their natal molecular cloud leads to the re-formation of a circumstellar disc. As a result, these stars may masquerade as pre-main-sequence objects due to ongoing accretion and the presence of infrared excess emission. A significant part of the observed populations of old accretors in large star-forming regions may be explained by this mechanism. As it may have wide-ranging consequences for the early evolution of planetary systems in rich stellar environments, further investigation of this mechanism is warranted.

5

UNDERSTANDING DISCS IN BINARY YSOS – DETAILED MODELLING OF VV CRA

Given that a majority of stars form in multiple systems, in order to fully understand the star- and planet-formation processes we must seek to understand them in multiple stellar systems. With this in mind, we present an analysis of the enigmatic binary T-Tauri system VV Corona Australis, in which both components host discs, but only one is visible at optical wavelengths. We seek to understand the peculiarities of this system by searching for a model for the binary which explains all the available continuum observations of the system. We present new mid-infrared interferometry and near-infrared spectroscopy along with archival sub-mm observations, which resolve the binary at 1.3 mm for the first time. We compute a grid of pre-main-sequence radiative transfer models and calculate their posterior probabilities given the observed spectral energy distributions and mid-infrared interferometric visibilities of the binary components, beginning with the assumption that the only differences between the two components are their inclination and position angles. Our best-fitting solution corresponds to a relatively low luminosity T-tauri binary, with each component's disc having a large scale height and viewed at moderate inclination ($\sim 50°$), with the infrared companion inclined by $\sim 5°$ degrees more than the primary. Comparing the results of our model to evolutionary models suggests stellar masses $\sim 1.7\,M_{\odot}$ and an age for the system of 3.5 Myr, towards the upper end of previous estimates. Combining these results with accretion indicators from near-IR spectroscopy, we determine an accretion rate of 4.0 $\times 10^{-8}\,M_{\odot}\,yr^{-1}$ for the primary. We suggest that future observations of VV CrA and similar systems should prioritise high angular resolution sub-mm and near-IR imaging of the discs and high resolution optical/NIR spectroscopy of the central stars.

Material in this chapter is adapted from:
P. Scicluna et al., in preparation for submission to MNRAS

5.1 INTRODUCTION

Stars form in turbulent molecular clouds, and as a result of turbulence, regions of the cloud condense to form cores, which may then continue to collapse under the influence of gravity (e.g. André et al., 2014). This may result in the formation of a single star, or the core may fragment and form many stars (Zinnecker, 1984). Angular momentum must be conserved during this collapse, inevitably resulting in any stars being surrounded by a disc of material, which may then be accreted by the star, ejected from the system, or potentially condense into a planetary system (Williams and Cieza, 2011). In the event that two or more stars form on gravitationally bound orbits, they will form a binary or multiple protostellar system (Zinnecker, 1984).

Protostellar and pre-main-sequence binaries provide unique insights into the star-formation process (Zinnecker, 1984; Kraus and Hillenbrand, 2009; Duchêne and Kraus, 2013). Although more complex, it is known that many young stars form as binary or multiple systems. The probability that a companion is present depends on the mass

of the primary and the environment in which the stars form (for details see Duchêne and Kraus, 2013, and references therein). So until they are studied in the same detail as single stars our understanding of star-forming processes will remain fundamentally incomplete. Thanks to their quasi-coeval nature, binary systems provide key tests for models of stellar evolution; pre-main sequence binaries are therefore crucial to the calibration of evolutionary models at these early stages (Kraus and Hillenbrand, 2009). Of particular interest are systems where one or both components still host protoplanetary discs, enabling tests of the evolution of the discs and the star-disc interaction, and in which the binary separation is large, so that the evolution is not complicated by binary interactions (Williams and Cieza, 2011). Furthermore, studying coeval systems could yield new constraints for models of planet formation.

VV Corona Australis (VV CrA) is a young binary system in the Corona Australis star-forming region. Situated approximately 20 arc minutes south east of the prominent Coronet cluster, it is the brightest component in what appears to be a smaller condensation of young stars (Sicilia-Aguilar et al., 2013a). Previously thought to be a single star, according to Reipurth and Zinnecker (1993), a companion was discovered approximately 2″ to the north east of the optical source by Frogel (unpublished) due to a displacement of the near-infrared peak from the optical coordinates. At the time, this companion dominated the near-infrared emission of the system despite being too extinguished to be visible at shorter wavelengths (Chelli et al., 1995). This infrared companion, now referred to as VV CrA NE, has since faded (Przygodda, 2004) such that the optical component (VV CrA SW) is presently the brighter source at all wavelengths at which the binary can be resolved (Kruger et al., 2011). Although the mass ratio of the binary is unknown, throughout this paper we follow Smith et al. (2009b) in referring to the optical component VV CrA SW as the primary.

The peculiarities of the binary have made it an intriguing observational target, however it remains enigmatic. The combination of high extinction and ongoing accretion makes the determination of the spectral types of the stars nearly impossible, since veiling fills in many of the photospheric lines (Herczeg and Hillenbrand, 2014). Nevertheless, many values have been published for the primary, ranging from K7 (Appenzeller et al., 1986) to K1 (Neuhäuser et al., 2000).

Furthermore, the origins of both the high obscuration and the variability of the secondary remain unknown, although two viable solutions have been proposed by Smith et al. (2009b). In one solution (their case B) VV CrA NE is inclined such that we view it through its own circumstellar disc, while the second (case A) requires that the disc of the primary is the source of the obscuration. In either case, the variability may be caused either by column density variations leading to changes in the extinction, or by an accretion outburst similar to that of FU Orionis (Smith et al., 2009b).

However, some progress has been made thanks to observations across a wide wavelength range. Both sources are variable in the infrared, although the variability of the primary is much weaker than that of the secondary. Both show emission in a variety of spectral lines (Prato et al., 2003) and appear to be driving outflows (Takami et al., 2003). Both components are bright in the (sub-)mm, and Lommen et al. (2010) used unresolved SMA data to determine a total dust mass of $3.9 \times 10^{-4}\,M_{\odot}$ for the binary, and a spectral index indicative of significant grain growth.

In this chapter, we present a selection of new observations along with a re-reduction of archival data, which are then used, along with data from the literature, to constrain

radiative transfer modelling. Section 5.2 gives a brief introduction to the Bayesian method used to find the best-fitting model. In section 5.3 new infrared interferometric and spectroscopic data are presented along with archival sub-millimetre observations. Section 5.4 gives an overview of the methods used for the radiative transfer calculations and to infer the best-fitting model, the results of which are discussed in section 5.5. Observational priorities that will enable future modelling efforts to improve upon our results are then discussed, before summarising the conclusions in section 5.6.

5.2 AN INTRODUCTION TO BAYESIAN INFERENCE

This discussion is based heavily on Hogg et al. (2010) and Andrae (2010), which the interested reader should peruse for a deeper understanding of the methods involved.

Suppose one has a set of data D which contains a number of observations, and wishes to identify which model M_i, drawn from a set of n models, fits these observations best. In a frequentist approach, one would seek to quantify the quality of the fit either by minimising the χ^2 statistic or by maximising the (logarithmic-)likelihood function $\mathcal{L} = P(D|M_i)$ i.e. by considering only how well the model reproduces the dataset.

However, this does not account for any previous knowledge about the object being modelled, whether from statistical, theoretical or literary considerations. Failing to include this information in the fitting process may lead one to prefer a model with slightly higher likelihood in spite of its intrinsically lower probability. To give an example appropriate to the main content of this article, consider a number of randomly oriented discs, where inclination $i = 0$ implies a face-on disc. For geometrical reasons, the probability of $\pi/3 \leqslant i \leqslant \pi/2$ is one half, and hence higher inclinations are intrinsically preferred. Therefore, if a low-inclination model has higher $\mathcal{L}$ in a particular case, the increased likelihood must outweigh the intrinsically lower probability of this configuration for the low-inclination model to be considered the better fit.

Such *a priori* information can be encoded as the distribution of the probabilities of the models $P(M_i)$ which is referred to as the *prior probability distribution* or more often simply the prior. Given that what one wishes to calculate is the probability of model i given the observations or $P(M_i|D)$ (the *posterior*) one quickly arrives at

$$P(M_i|D) = \frac{P(D|M_i)\,P(M_i)}{P(D)}, \tag{43}$$

which it can be clearly seen is Bayes theorum. Correct evaluation of the posterior therefore depends upon the correct choice of priors and likelihood functions, and their correct evaluation.

In the case of astronomical photometry, the statistical uncertainties are dominated by Poisson noise and are therefore nearly gaussian, and the choice of likelihood function is straightforward. If observation d_j belongs to our datased D, and consists of a flux F_j observed at wavelength λ_j with associated photometric uncertainty $\sigma_{F,j}$

and bandwidth $\sigma_{\lambda,j}$ and the covariances are zero[1], then provided that the modelled wavelengths agree with those observed the likelihood can be calculated from:

$$\mathcal{L}_{ij} = \frac{\sigma_{F,j}\sigma_{\lambda,j}}{2\pi} \exp\left(\frac{-\sigma^2_{\lambda,j}}{2\sigma^2_{\lambda,j}\sigma^2_{F,j}}\left(F_j - F_{M_i,j}\right)^2\right) \tag{44}$$

where $F_{M_i,j}$ and $\lambda_{M_i,j}$ are the wavelength and flux produced by model M_i that correspond with observation d_j.

Although the distribution of uncertainties for other astronomical observables are in general *not* gaussian (e.g. Rola and Pelat, 1994), in the absence of further information, the assumption of gaussianity is no worse than any other. Hence, it is common to apply Eq. 44 to all observables. For example, in the case of interferometric observations, the fluxes are replaced with the visibilities, and the bandwidth with the spectral resolution.

In the case of observables where two parameters must be fitted, equation 44 must be altered slightly. For example, in the case of a polarimetric observation, where both the polarisation fraction p and angle θ must be fitted, it becomes

$$\mathcal{L}_{ij} = \frac{\sigma_{p,j}\sigma_{\theta,j}}{2\pi} \exp\left(\frac{-1}{2\sigma^2_{\lambda,j}\sigma^2_{F,j}}\left(\sigma^2_{p,j}\left(p_j - p_{M_i,j}\right)^2 + \sigma^2_{\theta,j}\left(\theta_j - \theta_{M_i,j}\right)^2\right)\right). \tag{45}$$

To find the likelihood of model i, one must then calculate the product $\mathcal{L}_i = \prod_j \mathcal{L}_{ij}$

Once the posterior has been appropriately evaluated, the best fit can be extracted from the maximum of the distribution. However, one is usually more interested in the *credible interval* of each variable, usually taken as the 68.3% credible region (or *1–sigma region*). This is the region within which 68.3% of parameter estimates lie. To determine this, one must calculate the marginal distributions of the posteriors by integrating over all other variables i.e. for two variables a and b:

$$P(M_i|D,a) = \int_{b'} P(M_i|D,a,b)\,db', \tag{46}$$

which leaves one with a one-dimensional distribution of the posterior. From this, the 1–sigma region can be determined by integrating the distribution to find the region that contains 68.3% of the probability. This region is non-unique, so it is common to define it either as the narrowest region, as a region symmetrical about the median, or one symmetrical about the mean. The results above refer to the narrowest region.

5.3 OBSERVATIONS

5.3.1 *MIDI visibilities*

VV CrA was observed in June 2004, November 2004, and May 2005 (Tab. 4) with the MID-infrared Interferometer (MIDI) instrument (Leinert et al., 2003a,b; Morel et al.,

1 In all likelihood, this is not a very good assumption, since the effective wavelength of a filter during an observation depends upon the spectral shape of the emission being observed.

2004) at the Very Large Telescope Interferometer (VLTI). Both components of the binary were individually measured due to their comparatively large separation. The baselines UT1-UT3, UT2-UT3, and UT3-UT4 were used and the collected light was dispersed with the prism ($R \sim 30$).

The data were reduced with the MIA+EWS package[2]. MIA is based on the analysis of the power spectrum, while EWS implements a coherent analysis of the interferometric fringe signal (Jaffe et al., 2004). The visibilities used for the modelling have been derived with MIA and confirmed with EWS. All visibilities have been calibrated by all the calibrators taken in the same night. The stability of the transfer function is reflected by the errors shown together with the visibilities. Calibrators with peculiar visibilities have been ignored and are indicated in the journal of observations (Tab. 4).

For technical reasons, the single dish spectra derived from MIDI measurements vary over time in absolute calibration. Therefore, they are scaled to the better calibrated TIMMI2 spectra from Przygodda (2004)

Three older measurements previously obtained with MIDI in June 2003 are also included (Przygodda, 2004). These observations have been made with projected baseline lengths between 99.7 m and 102.2 m along position angles between 35.7° and 23.9°.

The resulting visibilities are plotted in Fig. 23. Two observations of VV CrA NE are excluded from the plot and from the model fitting (§ 5.4); these are flagged in Tab. 4 as *e*.

5.3.2 *CRIRES Spectra*

VV CrA SW was observed three times over the nights 22,23,24-AUG-2013 as part of programme ESO-091.C-0768(A) with the CRIRES instrument at the European Southern Observatory (ESO) Very Large Telescope (VLT) (Kaeufl et al., 2004).

The observations were performed with a central reference wavelength of 2170.573 nm and slit width of 0.4 " giving a spectral resolution of $\frac{\lambda}{\Delta\lambda} \sim 50{,}000$. In order to provide good sky subtraction, the star was nodded along the slit between individual exposures. Three sub-integrations of 30 seconds were taken for each observation. Standard reduction steps for infrared observations were performed using IRAF, including flat–fielding, bias–subtraction and spectral extraction. Nodding on the slit, produces two spectra from each observation block which were then median combined. These spectra were then corrected for telluric absorption using standards observed on the same night.

The wavelength range covered by these observations is ~ 2143 - 2195 nm. Unfortunately, no photospheric lines are detectable within the spectra, and so a spectral type derivation was not possible. However, the Br-γ emission line lies within this range, and is closely associated with accretion (Antoniucci et al., 2011); the section of the spectrum containing the Br-γ line is shown for each night's observations in Fig. 24. No significant variations in the equivalent width (EW) of this line were measured over the course of the three nights, with a mean measurement of 9 ± 0.7 Å.

Using the observed NIRC K-band flux of 1.63 Jy for this target (Koresko, priv. comm.), corrected for extinction using the redding law by Steeman & The (Steenman and The, 1991), we converted the Br-γ EW into a luminosity (taking the distance

2 http://www.strw.leidenuniv.nl/~nevec/MIDI/

Table 4: Journal of MIDI Observations. The length and position angle of the projected baseline has been determined from the fringe tracking sequence, the airmass from the photometric frames.

Date of Observation	Universal Time	Object	IRAS [Jy]	proj. Baseline [m]	[deg]	AM	Interferometric Frames	Photometric Frames	Flags
02-06-2004	00:33 - 00:55	HD 112213	10.8	45.4	40.8	1.1	8000×12 ms	2×1500×12 ms	s
02-06-2004	06:59 - 07:27	VV CrA SW		45.7	42.7	1.0	8000×15 ms	2×1500×15 ms	
02-06-2004	07:33 - 07:48	HD 178345	8.6	44.9	45.1	1.0	8000×15 ms	2×1500×15 ms	s
02-06-2004	07:57 - 08:40	VV CrA SW		43.0	51.0	1.1	8000×15 ms	2×1500×15 ms	
02-06-2004	10:14 - 10:31	HD 178345	8.6	35.2	61.3	1.4	8000×15 ms	2×1500×15 ms	s
04-11-2004	00:01 - 00:26	HD 178345	8.6	57.0	145.7	1.4	20000×12 ms	2×5000×12 ms	s
04-11-2004	01:07 - 01:31	VV CrA SW		52.7	164.8	2.0	12000×12 ms	2×3000×12 ms	
04-11-2004	01:31 - 02:10	VV CrA NE		51.9	175.9	2.6	12000×12 ms	2×3000×12 ms	e,v
04-11-2004	02:10 - 02:47	HD 188603	11.5	45.5	168.6	2.5	16000×12 ms	2×5000×12 ms	v
04-11-2004	02:47 - 03:54	HD 25604	5.1	60.7	117.1	1.7	16000×12 ms	2×5000×12 ms	
04-11-2004	05:04 - 05:29	HD 20644	14.7	59.1	101.5	1.7	12000×12 ms	2×3000×12 ms	
04-11-2004	07:18 - 07:36	HD 37160	6.5	61.0	107.4	1.2	8000×12 ms	2×2000×12 ms	s
04-11-2004	09:00 - 09:23	HD 50778	17.3	61.0	112.6	1.0	8000×12 ms	2×2000×12 ms	
29-05-2005	06:19 - 07:00	HD 139127	12.3	82.8	51.6	1.3	8000×18 ms	2×4000×18 ms	p,s
29-05-2005	07:28 - 07:56	HD 142198	6.3	92.0	41.8	1.6	8000×18 ms	2×4000×18 ms	
29-05-2005	08:54 - 09:17	HD 152820	7.6	77.7	49.7	1.7	8000×18 ms	2×4000×18 ms	
29-05-2005	09:17 - 09:56	VV CrA NE		88.8	47.5	1.2	8000×18 ms	2×4000×18 ms	
29-05-2005	09:56 - 10:19	VV CrA SW		85.7	49.1	1.3	8000×18 ms	2×4000×18 ms	
29-05-2005	10:19 - 10:53	HD 178345	8.6	81.6	51.4	1.4	8000×18 ms	2×4000×18 ms	p,s
30-05-2005	22:35 - 23:15	HD 102839	5.9	58.9	91.6	1.4	8000×18 ms	2×4000×18 ms	
30-05-2005	00:17 - 00:41	HD 102461	8.6	62.0	114.0	1.2	8000×18 ms	2×4000×18 ms	s,v
30-05-2005	01:24 - 01:56	HD 139127	12.3	54.1	88.7	1.2	8000×18 ms	2×4000×18 ms	p,s
30-05-2005	01:56 - 02:09	HD 139127	12.3	56.1	92.1	1.1	8000×18 ms	2×4000×18 ms	a,s,v
30-05-2005	03:18 - 03:45	HD 178345	8.6	41.6	73.1	1.5	8000×18 ms	2×4000×18 ms	s
30-05-2005	03:45 - 03:58	HD 178345	8.6	43.5	75.9	1.4	8000×18 ms	2×4000×18 ms	a,s
30-05-2005	03:58 - 04:29	VV CrA NE		48.7	84.8	1.3	8000×18 ms	2×4000×18 ms	
30-05-2005	04:29 - 04:42	VV CrA NE		50.4	87.0	1.2	8000×18 ms	2×4000×18 ms	a,e
30-05-2005	04:42 - 05:04	VV CrA SW		53.0	90.3	1.2	8000×18 ms	2×4000×18 ms	
30-05-2005	05:04 - 05:16	VV CrA SW		54.4	92.1	1.1	8000×18 ms	2×4000×18 ms	a
30-05-2005	05:16 - 05:28	VV CrA SW		55.7	93.9	1.1	8000×18 ms	2×4000×18 ms	a
30-05-2005	05:28 - 05:49	VV CrA NE		57.6	96.9	1.1	8000×18 ms	2×4000×18 ms	
30-05-2005	05:49 - 06:14	HD 133774	8.4	49.4	130.6	1.3	8000×18 ms	2×4000×18 ms	s
30-05-2005	07:01 - 07:35	HD 139127	12.3	57.6	149.7	1.5	8000×18 ms	2×4000×18 ms	p,s
30-05-2005	08:08 - 08:31	HD 152820	7.6	54.5	144.1	1.4	8000×18 ms	2×4000×18 ms	
30-05-2005	08:55 - 09:21	HD 164064	5.0	42.2	124.9	1.5	8000×18 ms	2×4000×18 ms	
30-05-2005	09:21 - 10:26	VV CrA NE		56.7	142.8	1.3	8000×18 ms	2×4000×18 ms	
30-05-2005	10:26 - 10:59	HD 178345	8.6	56.7	147.2	1.5	8000×18 ms	2×4000×18 ms	p,s,v

[a] no recentering of the beams performed
[e] excluded from fitting
[p] photometry of one or both beams repeated
[s] spectrophotometric calibrator
[v] peculiar instrumental visibility

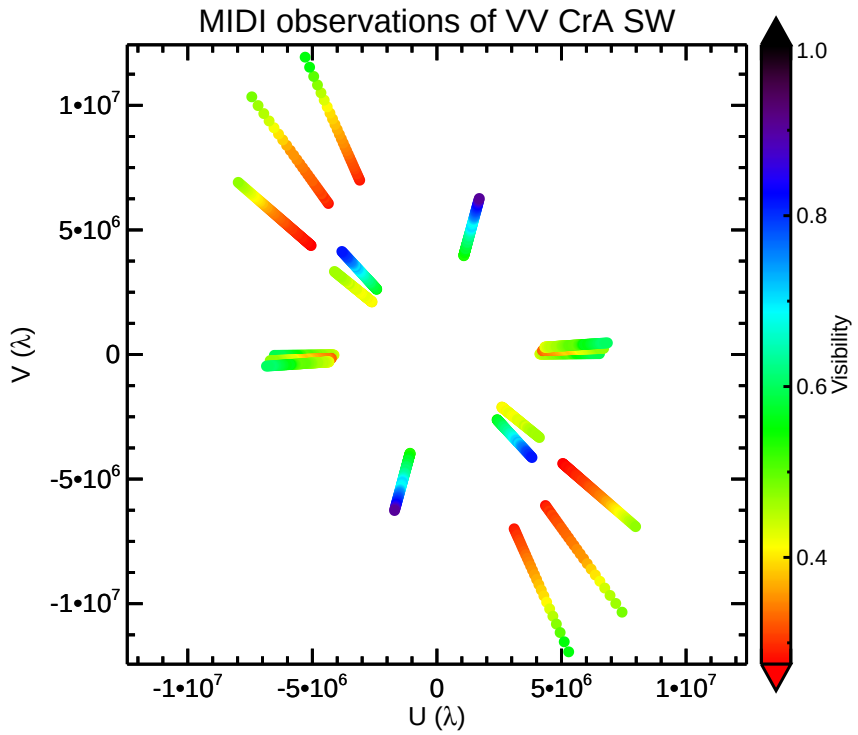

(a)

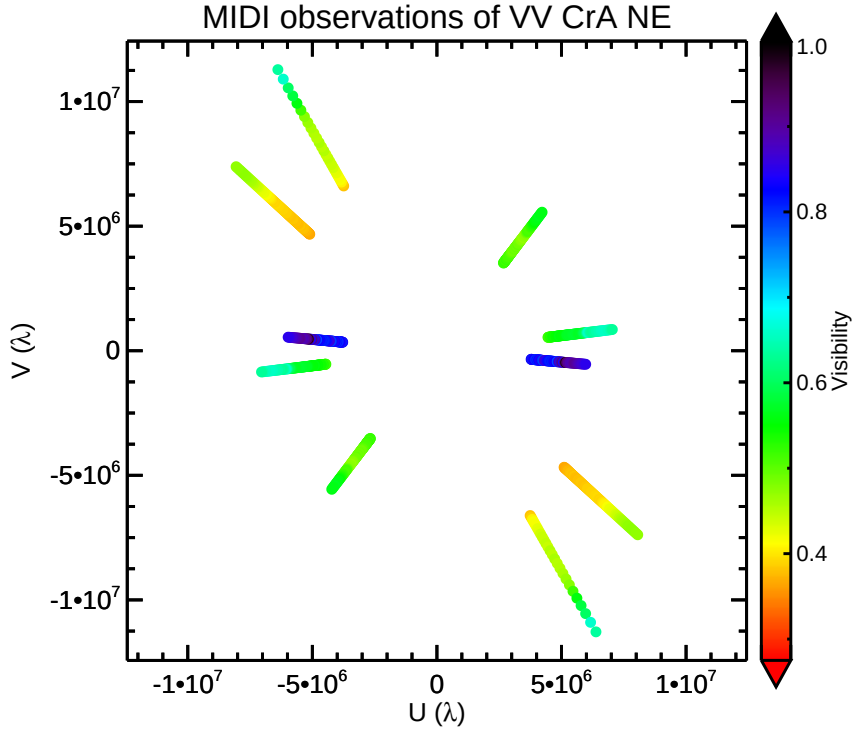

(b)

Figure 23: a) Wavelength-resolved visibilities plotted in the UV plane for the observations of VV CrA SW. b) As a) but for the 5 observations of VV CrA NE. UV distances are shown in units of the wavelength; as a result, each line has the longest wavelengths toward the centre and shortest wavelengths toward the edge of the plot.

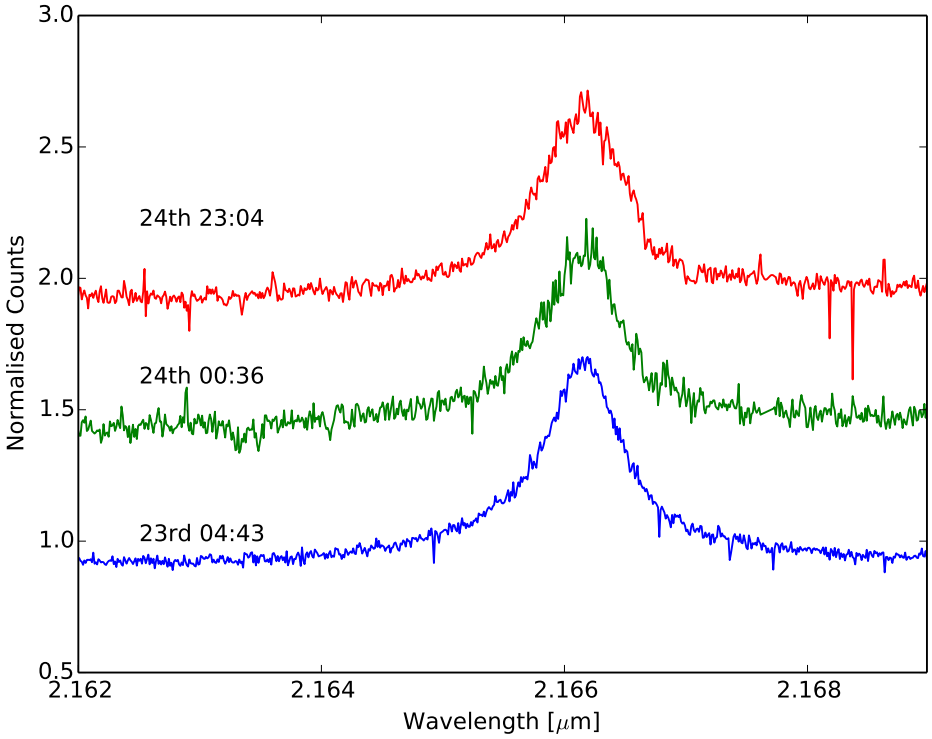

Figure 24: Median–combined CRIRES spectra from each observing night, showing the region of the spectra covering the Br-γ line.

to VV CrA SW to be 130 pc, Marraco and Rydgren 1981) which was found to be 7.2×10^{-4} $L_\odot$. Using the Alcalá et al. (2014) accretion luminosity relation for Br-γ, this then gives an accretion luminosity of 0.81 ± 0.8 $L_\odot$, where the spread comes from considering the spread in the measured EW over the course of the three days.

Following the methods of Sanchez-Bermudez et al. (2014) the presence of any extended emission from the Br-γ line was explored using spectro-astrometry. The original observations were not designed to probe the surrounding structure, and so only contained one position angle. The only conclusion that can be so derived from these observations is that there is no signal of extended emission at the 1-10 mas level in the Br-γ line in the north-south direction.

5.3.3 *SMA data*

In order to improve the constraints on the emission at long wavelengths, archival data taken using the Sub-Millimetre Array (SMA) at 1.3 mm were retrieved and reduced. VV CrA was observed on 01-Oct-2008 in Compact configuration with 6 antennae (previously published in Lommen et al., 2010) and on 12-Sept-2012 & 18-Sept-2012 in Extended configuration with 7 antennae (unpublished). Both datasets were reduced separately and in combination to explore the loss of flux on large scales.

The data reduction was performed using Common Astronomy Software Applications (CASA). After masking edge channels and checking for the presence of spectral lines, the data were imaged interactively using the *clean* routine using natural weighting. The final reduced image is shown in Fig 25. In order to extract continuum fluxes, 2D gaussians were fitted simultaneously to both components using the *imfit* routine with the literature positions of the two components as initial guesses. Images reconstructed using only the extended array observations resolve both components of the binary clearly, however more than 50% of the single-dish flux detected by Chini et al. (2003a) is missing. Folding in the observations taken in the compact configuration reduces this missing-flux problem somewhat, although there is still $\sim$ 25% missing flux. This suggests that either circumbinary structure or structure associated with the parent cloud are being filtered out; future observations using Atacama Large Millimetre/sub-millimetre Array (ALMA) including the compact array are required to identify the source of this emission.

Using these new resolved 1.3 mm fluxes and the 3 mm ATCA fluxes from Lommen et al. (2010) spectral indices were derived, with values α_{mm} of 2.15 ± 0.50 and 2.30 ± 0.60 for the primary and secondary, respectively. This indicates either substantial grain-growth, with a sizeable population of grains with radius > 1 mm, that the discs are very optically thick at mm-wavelengths, or a significant contribution from free-free emission at 3 mm.

5.4 MODELLING

5.4.1 *Radiative transfer modelling with* MC3D

MC3D (Wolf et al., 1999; Wolf, 2003) solves the radiative–transfer equation self consistently using Monte Carlo methods. Optimised for dusty circumstellar discs, it randomly propagates packets of radiative energy (photons) through the medium. Each

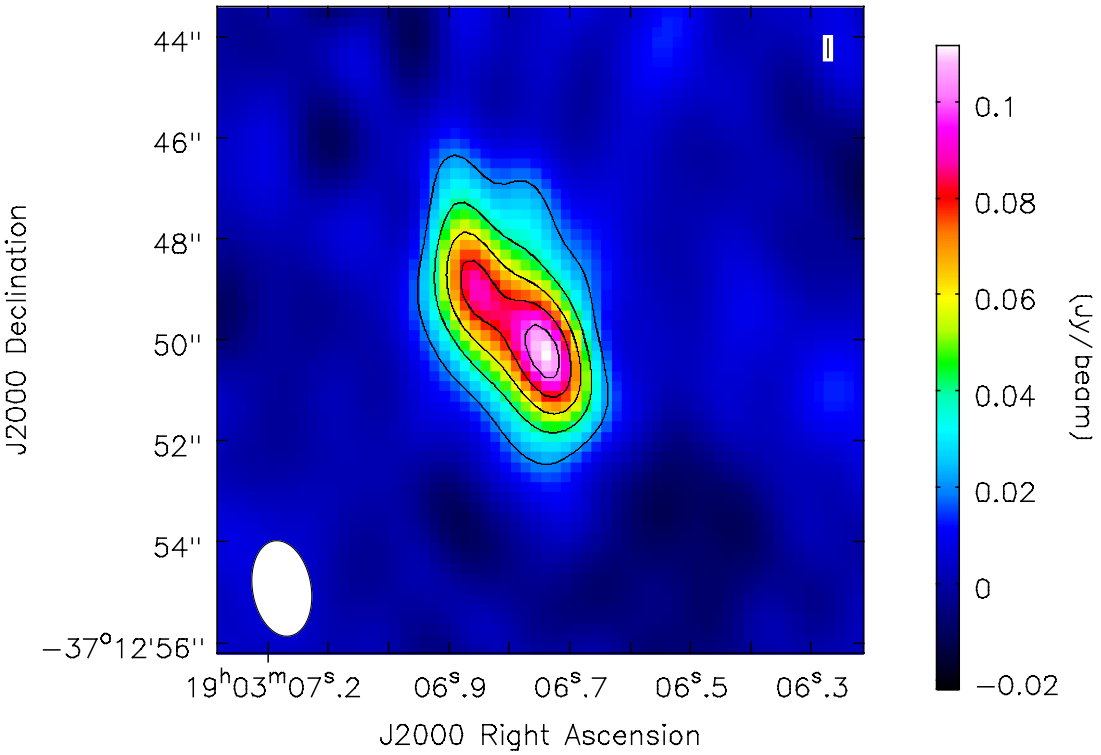

Figure 25: Final reduced continuum image reconstructed from the SMA observations at 1.3 mm. The white oval shows the size and shape of the synthesised beam.

packet is monochromatic and of fixed energy. Packets interact randomly with the medium, either through scattering events - in which only the direction and stokes vector of the photon change - or absorption & re-emission events - where the wavelength of the re-emitted photon is likely to change. For a given dust-density distribution, MC3D calculates the temperature distribution, and scattered and re-emitted fluxes.

The temperature distribution is calculated assuming that the dust is in local thermodynamical equilibrium (LTE) and that the dust is heated only by the central star. Once the dust–temperature distribution has been calculated, the spectrum of thermal re-emission can be calculated. For computational efficiency, this is done using ray–tracing techniques. Rays are generated ensuring that they sample all cells in the grid, stepped through the model grid to integrate the flux along each line of sight, and projected onto a detector. As this method only considers the contribution of thermal emission by dust, we also compute the contribution of the stellar radiation and scattered flux through monochromatic radiative transfer, in which the star launches radiation packets at each wavelength of interest, which are followed until they exit the model space. Images are computed using the same methods, with the results resolved into a number of pixels.

5.4.1.1 *Disc density distribution*

Although the radiative transfer is performed in 3 dimensions, to reduce the computational time only two dimensional, axi-symmetric disc density distributions are considered, which take the form

$$\rho(R,z) = \rho_0 \left(\frac{R}{R_0}\right)^{-\alpha} \exp\left(-\frac{1}{2}\left(\frac{z}{h(R)}\right)^2\right), \tag{47}$$

where the scale-height h is given by

$$h(R) = h_0 \left(\frac{R}{R_0}\right)^{\beta}, \tag{48}$$

where $R_0 = 100\text{AU}$, based on the α-viscosity disc of Shakura and Sunyaev (1973a). The above density distribution is defined in the range $R_{in} \leqslant R \leqslant R_{out}$, the inner and outer radii of the disc. For a gaseous disc in hydrostatic equilibirum $\alpha = 3(\beta - 0.5)$ (Shakura and Sunyaev, 1973a); given that only small grains are treated (see section 5.4.1.2) which should be dynamically coupled to the gas, the density distribution is only defined in terms of β. This distribution is then normalised to yield the desired total dust mass M_d. The disc is heated by a star whose spectrum is that of a blackbody $B(T_*)$ scaled to contain the required total stellar luminosity L_*.

5.4.1.2 *Dust model*

Although there are signs of grain-growth in millimetre-wave observations of VV CrA (Lommen et al. 2010 and section 5.3.3) only ISM-like dust grains are included in the models. The energy balance of the disc is primarily determined by the more numerous small grains which absorb the stellar radiation more efficiently (Dullemond et al., 2007; Testi et al., 2014). These grains therefore dominate the short–wavelength emission (and hence the MIDI observations) and the total energy absorbed by dust; this in turn determines the integrated energy of the SED. However, large ($\sim 1\,\text{mm}$) grains emit more efficiently at mm wavelengths, and therefore dominate the appearance of (sub–)mm images and the spectral index.

Theoretically, one expects that these larger dust grains should decouple from the gas density distribution, settling toward the mid-plane of the disc, while gas-drag would cause them to drift toward the inner regions of the disc (Dullemond and Dominik, 2004). In the absence of multi-wavelength, spatially-resolved observations at millimetre wavelengths it is impossible to quantify the distribution of these larger dust grains. Since the MIDI observations are sensitive only to the surface layers of the inner regions of the disc, which are expected to be populated by smaller grains, only grains with sizes between 5 nm and 250 nm are included with a power-law size distribution as in Mathis et al. (1977), consisting of 62.5% amorphous silicates and 37.5% graphite, using optical constants from Weingartner and Draine (2001), and are assumed to be compact spheres.

5.4.2 *The fitting process*

A suitable fit is sought by first building a database of $\sim 1.5 \times 10^6$ single-star+disc models, the parameter space for which is shown in Table 5. These models cover a

Table 5: Parameter space covered by radiative transfer models

Parameter	Range	Step	Prior
D (pc)	130	fixed	
L_* ($L_\odot$)	4 – 30	$\times 1.16$	Flat
T_* (K)	4000 – 5500	500	Flat
M_d ($M_\odot$)	$10^{-4.5}$ – 10^{-3}	$\times 10^{0.5}$	Flat
R_{in} (AU)	0.3 – 1.5	0.2	Flat
R_{out} (AU)	200	fixed	
h_{100} (AU)	10 – 35	5	Flat
β	1.0 – 1.3	0.05	Flat
i (°)	5 – 85	$\geqslant 2°$	$\sin i$
A_V (mag)	0.1 – 1.5	0.2	$\mathrm{HN}(\sigma = 0.3)$

range based on previous literature investigations of the system where possible (e.g. L_*, T_*, M_d) and a physically motivated range for the others.

For each of these models, MC3D returns output in the form of an SED from 0.3 to 3000 µm and images covering the wavelength range of the MIDI observations. From each image, synthetic interferometric visibilities corresponding to the baselines used in the MIDI observations are calculated using fast Fourier transforms. The real and imaginary parts of the synthetic visibilities are determined by linear interpolation between adjacent values in the Fourier plane.

To build models of the binary system, pairs of models are combined and compared the output to the MIDI visibilities and the SED of the system and its components. The fluxes used for the SED are given in Tab. 6; where possible, the most recent and robust photometry available have been selected. For each pair of models, the fluxes at wavelengths where no observations are available which resolve the binary are summed in order to robustly include the far-IR observations, while the resolved fluxes are compared to the respective member of the model pair. Due to the convergence of the resolved SEDs toward longer wavelengths through N & Q bands, and the similarity of the SMA fluxes, a subset of binary configurations are considered in which the two components differ only in inclination and position angles, and in which the NE component is obscured by its own disc.

These simulated data are then used to calculate posterior-probability distributions and their marginal distributions for representative binary configurations under certain assumptions, following the detailed description of the required calculations given in section 5.2. The likelihood for each datum is calculated using Eq. 44, and no additional weighting is applied to the data beyond that implied by their uncertainties and bandwidth, treating photometry and interferometry identically. As a result, the fitting process is naturally most sensitive to the most precise data which integrate over the narrowest wavelength range, which is in general those between 7–13 —m. The product of the likelihoods of all the data for a given model is then inserted into Eq. 43 along with the product of the priors of the model (see Tab. 5) to give the pos-

terior. The best-fitting model is the pair of single-star models which maximises the posterior.

5.5 DISCUSSION

5.5.1 *Best-fitting model & degeneracy*

Table 7 lists the parameters of the best-fitting models, and Fig. 26 shows a corner plot of the marginalised posterior distributions, illustrating degeneracies between different input parameters. In particular, R_{in} is degenerate with the inclinations of both discs. These are bimodal, with models with smaller $R_{in} \sim 0.3$ preferring solutions with inclinations $\sim 40-45°$ rather than the $\sim 50-55°$ solution of our best-fitting model. Otherwise, parameters are typically constrained to a small region near the value of the best-fitting model, or are upper or lower limits. Unfortunately, the grid resolution is not high enough to determine uncertainties from the marginalised distributions, however it is possible to derive certain robust constraints from Fig. 26. Our results indicate that models with relatively low luminosity stars with massive, unflared, geometrically thick discs seen at intermediate inclinations are strongly preferred. The luminosity is lower than suggested by some previous models (e.g. Wilking et al., 1992). This is a result of the extreme near-IR variability of the NE component, whose K-band flux has varied by 2 orders of magnitude over the last 3 decades (Kruger et al., 2011).

The SED of the best-fitting model is shown in Fig. 27. The best-fitting model reproduces the fluxes at short wavelengths ($\lambda \leqslant 30\mu m$) well, including the behaviour of the silicate feature in both cases, although the JHK-band fluxes are underpredicted. However, despite the very high dust mass, it does not reproduce the FIR–sub-mm fluxes. The grid does not include higher dust masses because, assuming a typical dust-to-gas ratio of ~ 100, the mass of the disc would then be comparable to that of the central object and self-gravity would begin to play a role (Lodato and Rice, 2004, 2005), and hence Eq. 47 would no longer adequately describe the density distribution. This cut-off coincides with an empirical upper limit to dust masses derived from sub-mm observations (Mohanty et al., 2013). Furthermore, the total dust mass of the binary implied by our model ($2 \times 10^{-3}\,M_\odot$) is 5 times larger than that determined by Lommen et al. (2010). As a result, further increases to the dust mass would not provide an acceptable solution.

Alternatively, increasing the maximum grain size would increase the sub-mm opacities, and hence increase the emergent flux at these wavelengths. As described in section 5.4.1.2, we lack the observational constraints required to justify the complexity that this would add to the model, and must therefore accept that a larger dust mass is required to reproduced the observed (sub-)mm emission. However, the compact nature of the 1.3 mm emission provides a further hint that grain-growth and settling processes should be included in future models. Figure 28 shows a simulation of the SMA observations computed using the best-fitting model as input to the *simobserve* & *simanalyze* tasks in CASA. As noted, the model does not reproduce the flux of the observations, being $\sim$ 2–3 times lower. However, the core of the emission of each disc appears more extended in the simulated image than the observation, suggesting a component of compact emission is missing from the model. A likely explanation is

Table 6: Data used for SED fitting

Effective wavelength[a] (μm)	Flux (Jy)			Ref.
	SW	NE	Unres	
0.36 ± 0.025	0.0042 ± 0.00014	$< 8\times10^{-5}$ [b]	**	1,2
0.43 ± 0.036	0.0081 ± 0.00067	< 0.00016 [b]	**	1,2
0.55 ± 0.038	0.0217 ± 0.0008	< 0.0004 [b]	**	1,2
0.7 ± 0.081	0.0510 ± 0.0007	< 0.001 [b]	**	1,2
0.9 ± 0.097	0.117 ± 0.003	< 0.002 [b]	**	1,2
1.25 ± 0.09	0.40 ± 0.06	0.014 ± 0.0098	**	3
1.65 ± 0.12	0.94 ± 0.13	0.153 ± 0.0211	**	3
2.16 ± 0.13	1.63 ± 0.23	0.846 ± 0.117	**	3
3.8 ± 0.22	1.88 ± 0.35	1.69 ± 0.311	**	3
4.80 ± 0.2	3.50 ± 0.65	2.6 ± 0.47	**	4
7.73 ± 0.245	13.7 ± 0.7	7.0 ± 0.4	**	2
8.74 ± 0.269	14.4 ± 0.2	4.5 ± 0.1	**	2
10.35 ± 0.357	15.0 ± 0.3	3.3 ± 0.1	**	2
12.33 ± 0.415	20.5 ± 0.7	8.7 ± 0.3	**	2
18.3 ± 0.527	28.4 ± 1.6	11.1 ± 0.8	**	2
24.56 ± 0.699	35 ± 18	25.1 ± 13.5	**	2
70 ± 8.84	**	**	55 ± 6	5
100 ± 14.3	**	**	80 ± 12	5
160 ± 31.4	**	**	66 ± 13	5
450 ± 16.8	**	**	12 ± 4	6
850 ± 27.7	**	**	2.0 ± 0.2	6
870 ± 54.2	**	**	1.66 ± 0.06	7
1200 ± 164	**	**	0.58 ± 0.06	8
1270 ± 117	**	**	0.469 ± 0.021	9
1340 ± 22	0.1999 ± 0.0074	0.1701 ± 0.0083	**	10

[a] Defined as the central wavelength of the filter ± half of the smallest interval, symmetrical about the central wavelength, that contains at least 68.3% of the area under the transmission curve.
[b] 3σ upper limits

References: (1) Marraco and Rydgren (1981); (2) Kruger et al. (2011) ; (3) Koresko (priv. comm.) ; (4) Ratzka et al. (2008); (5) Sicilia-Aguilar et al. (2013b); (6) Nutter et al. (2005); (7) Sicilia-Aguilar et al. (2011); (8) Henning et al. (1994); (9) Chini et al. (2003b); (10) this work

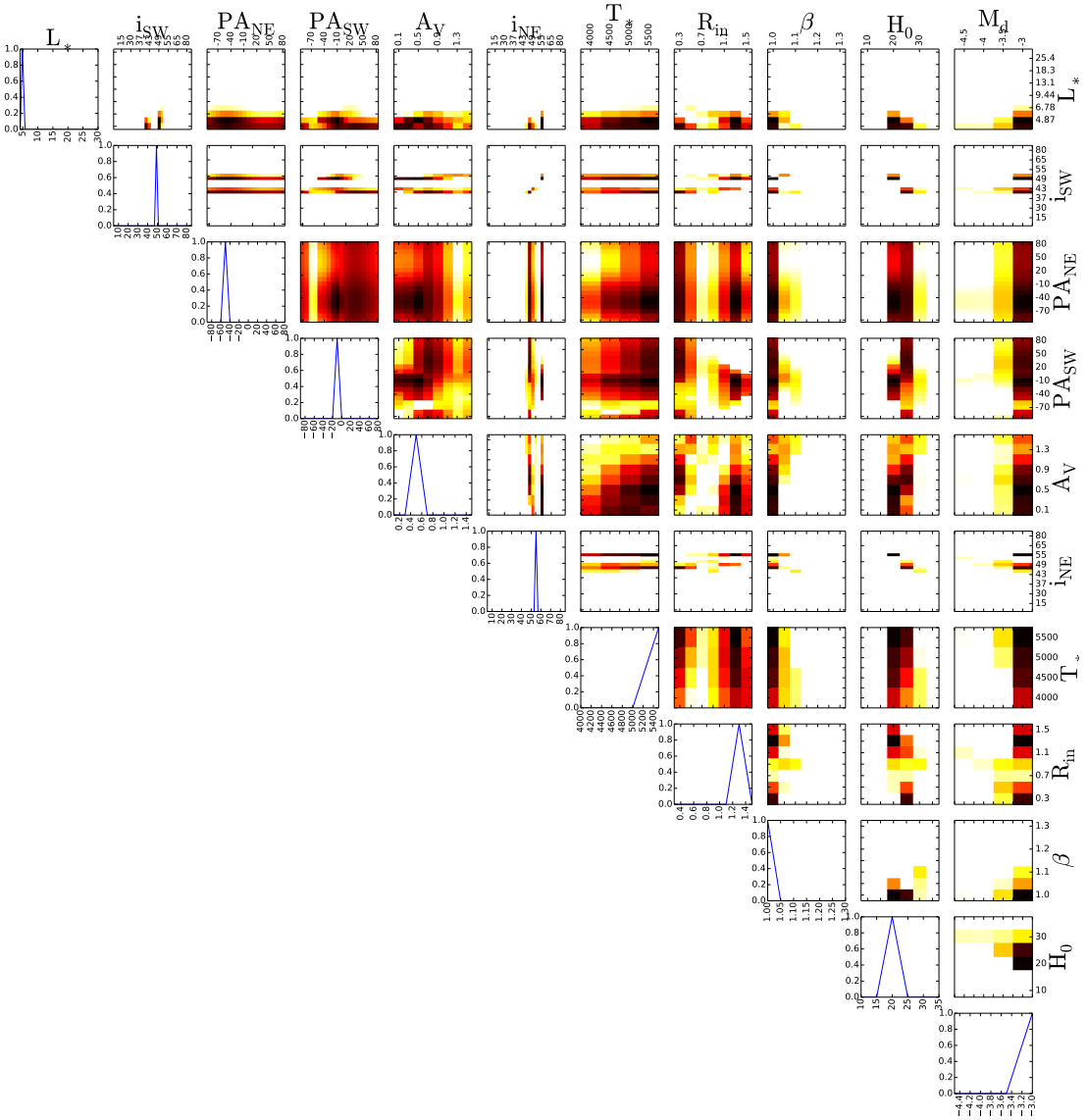

Figure 26: Cornerplot showing the degeneracies between the various free parameters in terms of the posterior-probabiltiy distribution marginalised over all other parameters, along with the marginal distributions of each free parameter. The colour scale is logarithmic, with each sub-plot separately normalised to its own maximum value; black indicates high probability and white low.

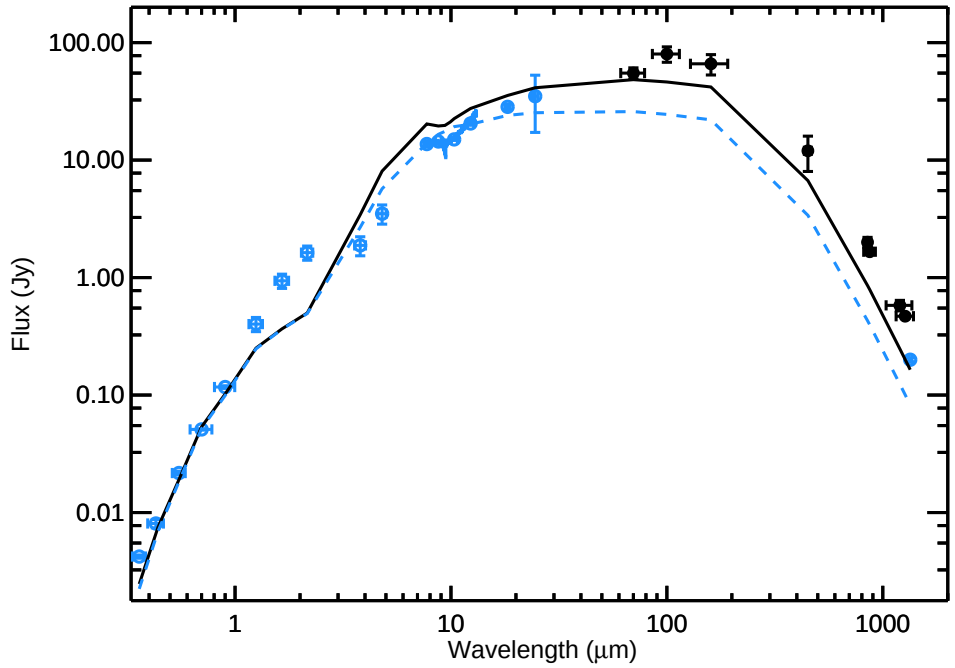

(a)

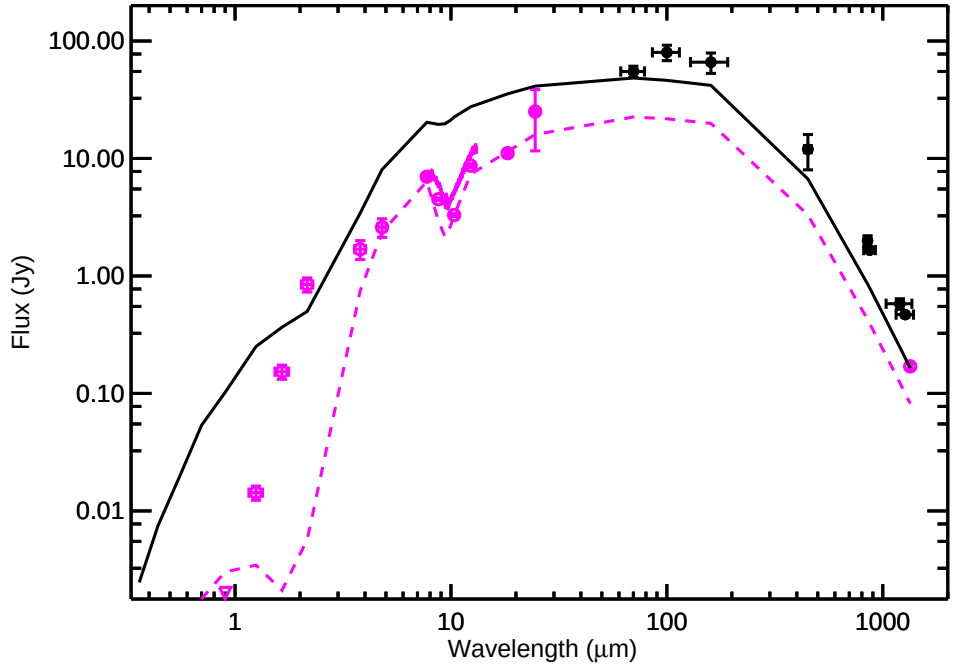

(b)

Figure 27: Simulated SEDs of the best-fitting model for the SW (*top*) and NE (*bottom*) components and the observed SEDs. In both cases, the solid black points correspond to photometry from observations which fail to resolve the two components of the binary (column *Unres* in Tab. 6), and the solid line corresponds to the sum of the model flux of both components. The coloured points correspond to resolved photometry, and the coloured dashed line indicates the best-fitting model's emission from each component separately. Triangles indicate observed 3-sigma upper limits.

Table 7: Best-fitting model parameters

Parameter	Best Fit
L_* ($L_\odot$)	4.9
T_* (K)	5500
M_d ($M_\odot$)	10^{-3}
R_{in} (AU)	1.3
R_{out} (AU)	200
h_{100} (AU)	20
β	1.00
i_{SW} (°)	49
i_{NE} (°)	55
A_V (mag)	0.5
PA (SW) (°)[a]	-10
PA (NE) (°)[a]	-50

[a] position angle east of north of the *minor* axis of the disc

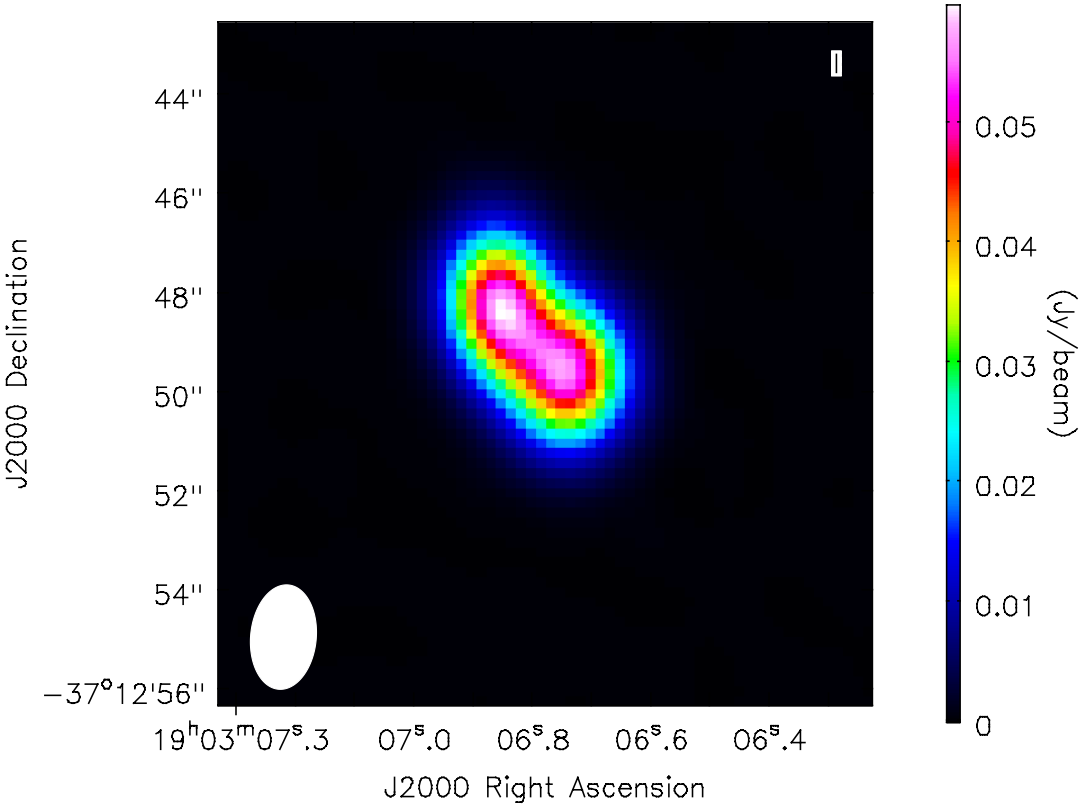

Figure 28: Simulated 1.3 mm image based on our best-fitting model. Produced using CASA *simobserve*, neglecting all sources of noise other than UV-coverage. The total flux is underpredicted, but the discs are also too extended compared to Fig. 25

the lack of large dust grains in this model; these grains should rapidly settle to the midplane and experience radial drift, making them more centrally concentrated. As large grains are more efficient mm-wave emitters than the ISM grains in our model, this would result in an additional component of compact emission, which may dominate the SMA observations. Furthermore, the poorly constrained contribution of free–free emission at these wavelengths would present an additional compact component. However, the data currently available are unable to constrain these processes at the level required for inclusion into these models.

Figures 29 and 30 compare the MIDI observations with the visibilities of our best-fitting model. In general, the model fits well, but tends to predict worsening resolution at longer wavelengths, in contrast to the observed visibilities, which tend to decrease with increasing wavelength. The emitting area of the disc as a function of wavelength must therefore increase faster compared to the size of the beam than our model assumes. One plausible explanation is an effect of the scattered flux; if $\sim 1\,\mu m$ dust grains are present at the disc surface as implied by infrared spectroscopy of sources in nearby star-forming regions (Furlan et al., 2006, 2009; Kessler-Silacci et al., 2006; McClure et al., 2010; Oliveira et al., 2010), these would efficiently scatter the radiation emitted by the disc, producing substantial additional extension. This effect would be strongest at wavelengths where the disc produces the most flux i.e. at longer wavelengths. This could plausibly be tested using the new generation of XAO imagers (e.g. SPHERE) to acquire near-infrared imaging polarimetry.

5.5.2 *Mass & evolutionary state*

An approximate stellar mass M and age t can be determined by comparing the temperature and luminosity of the best-fitting model to evolutionary tracks. Using the tracks of D'Antona and Mazzitelli (1997), interpolating functions are constructed for $T_*(M,t)$ and $L_*(M,t)$ from the isochrones, which are then solved simultaneously for M and t. A mass of $1.8\,M_\odot$ and an age of 3.0 Myr are thus determined; if the accretion luminosity determined in §5.3.2 is subtracted from the luminosity of the best-fitting model, one arrives at $1.7\,M_\odot$ and an age of 3.5 Myr. Both are inconsistent with previous estimates which inferred a very young T Tauri system based on the shape of the SED in the mid-infrared (e.g. Prato and Simon, 1997), but approximately consistent with the model of Koresko et al. (1997) for the primary. However, radiative-transfer-model fitting is only weakly sensitive to the stellar temperature, and relatively small variations imply significant changes in the mass and age. Only by improving spectral-type determinations can matters be improved.

The best-fitting model implies a stellar radius of $2.4\,R_\odot$ for the primary, which allows one to estimate an accretion rate from the accretion luminosity given in §5.3.2 as in Gullbring et al. (1998) and Schegerer et al. (2008). Assuming a mass of $1.7\,M_\odot$ as determined above and a truncation radius of $5\,R_*$ implies an accretion rate of $4.0 \times 10^{-8}\,M_\odot\,yr^{-1}$.

5.5.3 *Outlook*

As it is clear that a variety of questions remain concerning the state of VV CrA, we will now discuss which observations should be targeted to allow future modelling

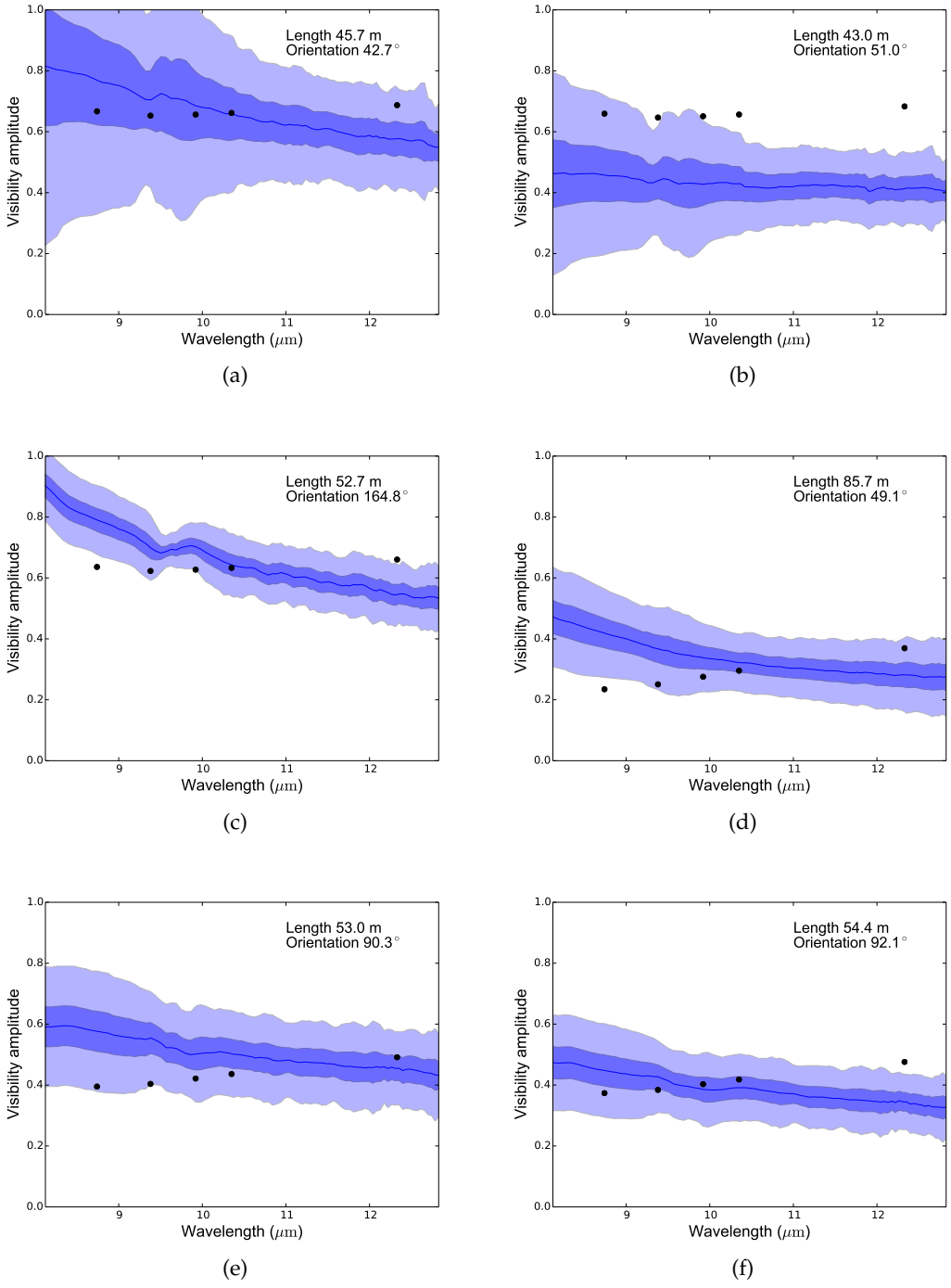

Figure 29: Comparison of observed visibilities and their counterparts in our best-fitting model showing all observations for the primary. The projected baseline length and orientation are given in the top-right corner of each plot. The full line indicates the observed visibility, the dark- and light-blue regions respectively indicate its 1- and 3-sigma regions, and the black points the simulated visibilities.

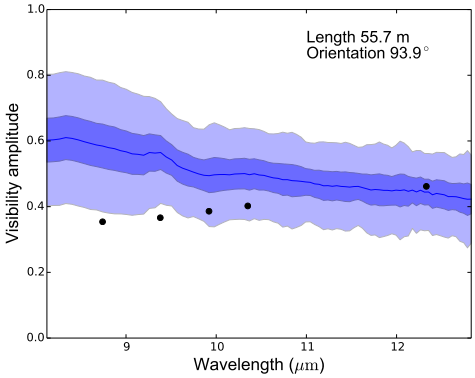

(g)

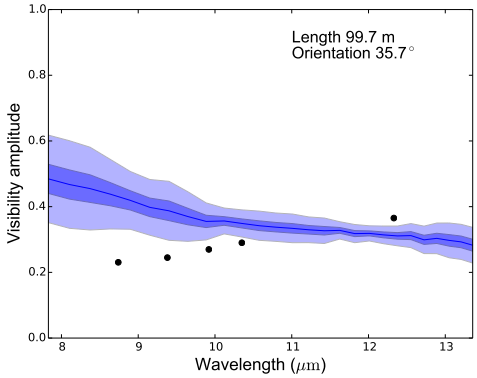

(h)

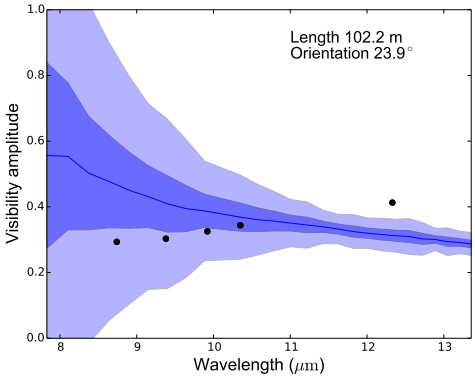

(i)

Figure 29: *cont.*

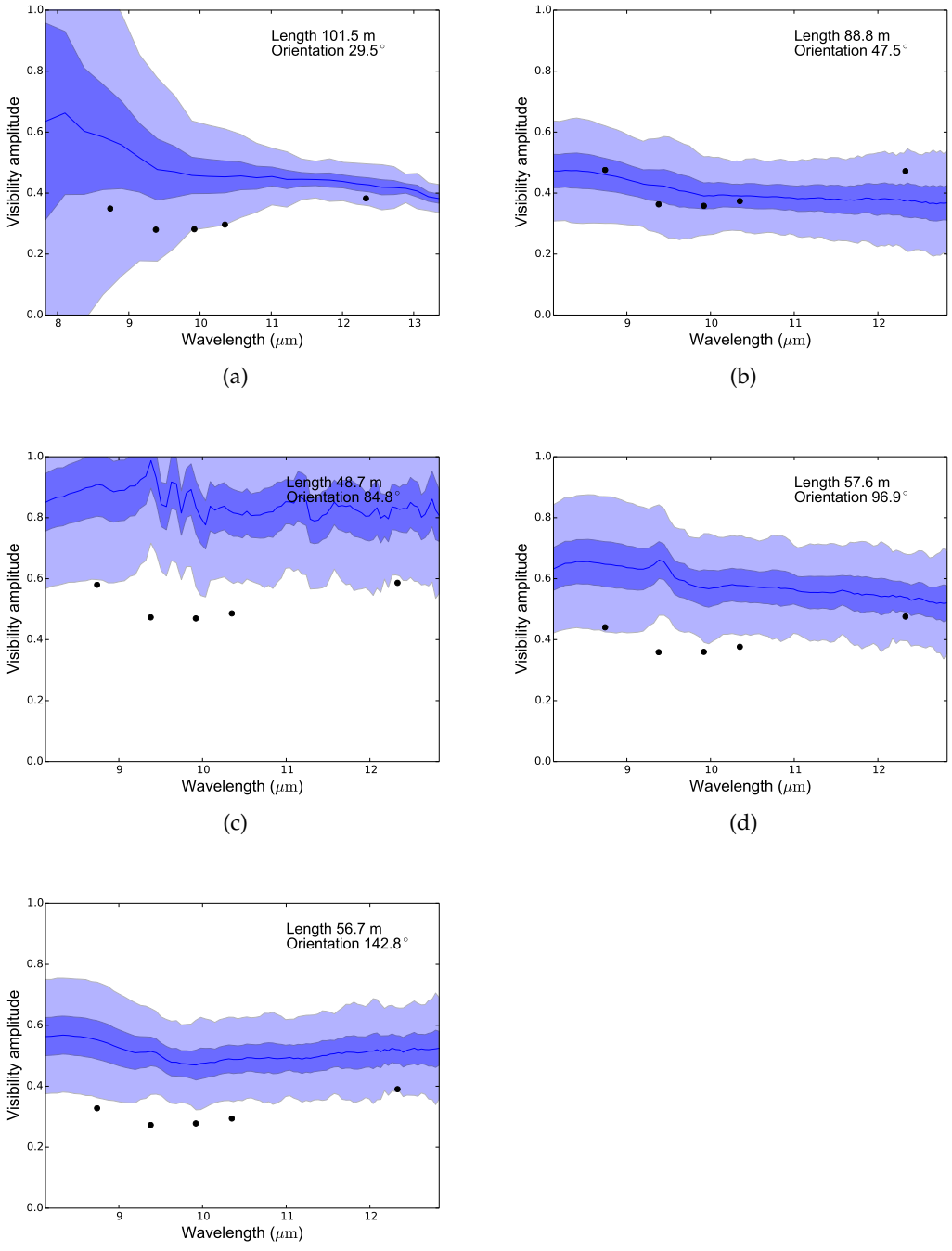

Figure 30: As Fig. 29, showing data for the secondary.

efforts to improve upon our limitations. As the major shortcoming of these models is the failure to consider larger dust grains, resolved observations in multiple ALMA bands should be considered a priority. Spatially resolved spectral-index maps of the two discs would allow a reasonable prescription of grain growth and settling to be incorporated in future models, giving more reasonable estimates of the dust masses. A by-product of such observations would be high-resolution molecular line data, allowing the disc inclinations and stellar masses of both components to be directly constrained. Knowing the masses of the stars would allow for a substantially improved age determination, while directly measured inclinations could conclusively differentiate between the two cases in Smith et al. (2009b).

Another aspect that would considerably enhance modelling efforts would be robust knowledge of the spectral types of the stars and their accretion rates. To date, this has proven nearly impossible due to the near-complete veiling of the photospheric lines in the primary, and the lack of flux from the secondary. The most promising course of action seems to be deep, high-resolution near-infrared spectroscopy covering a large range of wavelengths, or perhaps combined optical-NIR spectroscopy from instruments like XSHOOTER; observations of this kind would maximise the chances of resolving weak photospheric lines. Combining such data with a fitting method as in Manara et al. (2013) would allow the incorporation of the effect of veiling, improving the chances of finding a suitable solution.

As noted above, it is likely that there is a role for scattering by $\sim$ —m size grains in the disc surface. This can be probed by examining the wavelength-dependent morphology of the polarised flux at infrared wavelengths. The new generation of planet-hunting imagers (e.g. SPHERE, GPI, SCExAO) specifically exploit polarimetric imaging to improve contrast around bright stars, providing precisely the high-resolution capabilities required. This would probe the surface layers of the disc on 10-100 AU scales, providing short-wavelength data complementary to the aforementioned sub-mm observations. The polarimetric properties of dust grains are very sensitive to grain size; for grains somewhat larger than $\lambda/2\pi$, the polarisation fraction of the scattered radiation is relatively weak, and shows a number of sign changes as a function of angle, while significantly larger grains show strongly forward-peaked, highly polarised scattering. Both of these cases are easily distinguished from the Rayleigh-like scattering exhibited by small (ISM-like) dust grains in imaging polarimetry. Although VV CrA SW is rather faint compared to the AO limiting magnitudes of these imagers ($m_R \sim 12$, $m_I \sim 11$), Xu et al. (2015) have recently shown impressive performance with SPHERE for targets as faint as $m_R = 14$.

5.6 SUMMARY

A detailed study of the engimatic pre-main-sequence binary system VV CrA has been conducted. New near-infrared spectroscopy of the primary has derived an accretion luminosity of $0.81 \pm 0.8\ L_\odot$, and placed an upper limit on the extension of Br γ emission in the N–S direction of 10 mas. Archival SMA observations have been used to produce the first resolved image of the binary at 1.3 mm, and mid-infrared interferometry probes the inner regions of both discs.

Based on these observations and data from the literature, a model for VV CrA has been presented, showing that even a small misalignment of the discs is a plausible

explanation for the differences between the two components of the binary, with inclinations of 50–55°. This model suggests a lower luminosity for the central stars than previous work, most likely a result of the variability of the infrared companion. However, this model is unable to explain the sub-mm emission of the system, and hence it is suggested that future modelling efforts must include the effects of grain growth and settling. Based on our model, an age of 3.5 Myr and stellar masses of 1.7 $M_\odot$ was inferred; combining these results with the accretion luminosity yields an accretion rate of 4.0 $\times 10^{-8}\,M_\odot\,yr^{-1}$.

Observational priorities that may resolve outstanding questions have also been suggested. While resolved ALMA observations should be the priority to allow future models in include grain growth and settling, there is also a strong case for further near-infrared observations of both components. In particular, determination of at least two of mass, spectral type and luminosity for both components would provide a robust test of evolutionary models. Similar studies of other pre-main-sequence binaries should be conducted in order to build up a sample of coeval systems to constrain models of star & planet formation and evolution.

6

THE MASS-LOSS ENVELOPE OF VY CANIS MAJORIS

Massive stars live short lives and lose a large fraction of their initial mass through their stellar wind (Smith, 2014). Their mass is a key factor determining how and when they explode as supernovae, enriching the interstellar medium with heavy elements and dust (Smith, 2014). During the Red Supergiant phase, mass-loss rates increase prodigiously, but the driving mechanism for this has so far proven elusive (Woitke, 2006; Arroyo-Torres et al., 2015). This chapter presents high-contrast optical polarimetric-imaging observations of the extreme red supergiant VY Canis Majoris and its clumpy, dusty, mass-loss envelope. Using the new extreme-adaptive-optics instrument SPHERE at the VLT, the diffraction-limited resolution of an 8m-class telescope at visual wavelengths can be exploited for the first time (Beuzit et al., 2006). These data reveal an average grain radius of 475 nm, 50 times larger than in the diffuse ISM, large enough that the outflow is driven by photon scattering (Höfner, 2008), a mechanism known from oxygen-rich AGB stars, the lower-mass cousins of red supergiants (Norris et al., 2012). We find evidence for somewhat smaller grains in the clumps compared to those in the disc, supporting models of magnetic activity as a source of the clumps (Humphreys et al., 2007; Jones et al., 2007; Muller et al., 2007; Smith et al., 2009a; Richards et al., 2014; O'Gorman et al., 2015). Grains with 500 nm sizes are likely to survive the eventual explosion of VY Canis Majoris and hence make a meaningful contribution to the dust budget at high-redshift. Based on these observations, a survey program is being undertaken to constrain the mass–loss variations and grain sizes in a representative sample of red supergiants; this will robustly constrain the dust contribution of this population to the interstellar medium for the first time.

Material in this chapter is adapted from:
P. Scicluna, R. Siebenmorgen, J. Blommaert, M. Kasper, N.V. Voshchinnikov, R. Wesson & S. Wolf; submitted for publication in Nature

6.1 INTRODUCTION

When massive stars ($M_* \geqslant 8\,M_\odot$) approach the end of their lives, they may expand and cool to become Red Supergiants (RSGs), a phase characterised by prodigious mass loss and dust production. This mass loss is a key factor in determining the future evolution of massive stars, including what type of supernova they will result in (Georgy et al., 2012). Moreover, if a star explodes within a dense mass-loss envelope, the effect on the resulting supernova is dramatic; the interaction of the explosion with the envelope releases huge quantities of energy (e.g. Moriya et al., 2011). However, the mechanisms driving mass-loss in cool evolved massive stars remain poorly understood, and mass-loss rates in evolution models are highly uncertain (Georgy et al., 2012) with severe consequences for our understanding of late stellar evolution. The source of momentum for the wind remains unclear: the acceleration of dust grains by radiation pressure seems the most promising mechanism (**?**), but the formation

of grains is inhibited by the extreme luminosity of RSGs. The outer atmospheres of RSGs are ∼20% larger than expected and have high molecular abundances - this extension is likely to be caused by radiation pressure on molecular lines (Arroyo-Torres et al., 2015), but the dust species that can form at these distances ($< 3\,R_*$) are not abundant enough to supply the momentum required to drive the wind (Bladh and Höfner, 2012), while the iron-rich silicates that most efficiently absorb the star's radiation cannot form until $\sim 20\,R_*$ (Woitke, 2006). However, the acceleration of the wind to terminal velocity is observed to begin around $10\,R_*$ (Richards et al., 1998); the only abundant species that can form so close are Ca-Al or Mg rich silicates (e.g. melilite, $Ca_2Al_2SiO_7$, forsterite, Mg_2SiO_4), which are nearly transparent to the stellar radiation. If the acceleration is dominated by these species, they can only drive the wind if they are large enough to be highly efficient scatterers (Bladh and Höfner, 2012).

VY Canis Majoris (VY CMa) is a nearby (1.2 kpc (Zhang et al., 2012)) dust-enshrouded red supergiant (RSG), a rare class of objects of which it is the best studied example. It is one of the most intrinsically luminous stars in the sky ($L = 3 \times 10^5 L_\odot$ (Wittkowski et al., 2012)) and excluding solar-system bodies is the third brightest object in the sky at 10 µm (Joint Iras Science, 1994). It boasts a large optical reflection nebula visible through even small telescopes, created by its prodigious mass loss ($> 10^{-4} M_\odot\,yr^{-1}$). Despite decades of detailed study (Serkowski, 1969; Herbig, 1974; Kastner and Weintraub, 1998), it remains enigmatic, with frequent conflicts between different wavelength regimes (Smith et al., 2009a; O'Gorman et al., 2015). Due to its incredible brightness, VY CMa is key to revealing the properties and evolution of dust in the mass-loss envelopes of RSGs.

This chapter explores the possibility of determining grain sizes in the envelope of VY CMa using two different methods. First, a new, 3–dimensional radiative transfer model for the dusty envelope is presented in Sect 6.2, in which the SED is fitted based on literature findings of the global geometry of the envelope. Section 6.3 then presents new high–contrast near–infrared imaging and optical polarimetric imaging. In section 6.4, the optical polarimetry is used to constrain the distribution of dust grain sizes at various locations in the envelope. Then, section 6.5 discusses the wider implications of these findings for the mass–loss history of VY CMa and the injection of dust into the ISM by RSGs.

6.2 RADIATIVE TRANSFER MODELLING

To constrain the total dust mass of the envelope and explore the influence of grain size on the broadband behaviour of the emission, a fully three–dimensional radiative–transfer model of the ejecta was developed. Based on the stellar properties derived by Wittkowski et al. (2012, see Table 8), a MARCS model atmosphere as the input stellar spectrum (Gustafsson et al., 2008) was selected as the basis for the input spectrum. The ejecta model geometry is based on literature discussions (Humphreys et al., 2007; Jones et al., 2007; Muller et al., 2007; Smith et al., 2009a) that suggest a slow phase of steady, equatorially enhanced mass loss (hereafter the 'disc' or 'envelope') and randomly-directed, fast-moving clumps and arcs, each of which corresponds to a distinct mass-ejection event (see Fig. 31). Humphreys et al. (2007) provided 3-D locations for 10 of these clumps and arcs distributed mainly to the South and West of the star, all of which are included in our model. Each clump/arc is modelled as a sphere or

Table 8: Assumed stellar properties of VY CMa

Property	Unit	Value
L_*	$[L_\odot]$	2.7×10^5
R_*	[AU]	6
T_*	[K]	3500
log g		0.0
d	[kpc]	1.17

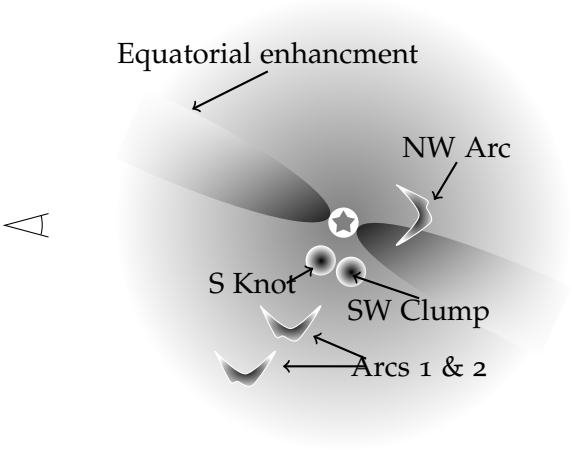

Figure 31: Cartoon diagram of the model geometry, including the brightest optical features. The dense equatorial mass loss is inclined such that we peer through part of it, with dense clumps and arcs to the SW. The observer is to the left, North is up and East is into the page.

filament with $\rho(r_s) \propto \exp\left(-\left(\frac{r_s}{200}\right)^2\right)$ where r_s is the distance, in AU, from the centre of the sphere/filament. The disc inclination and position angles are treated as free parameters, while the half-opening angle of the disc is fixed to 22°.5.The envelope has a density $\rho \propto r^{-p}$ with $1 \leqslant p \leqslant 2$, an outer radius of 7000 AU and the inner radius is set by dust formation radius, which we take as $5\,R_*$, where Mg-rich silicates condense (e.g. Gail and Sedlmayr, 2013).

This model is used in a three-dimensional dust radiative transfer code (Heymann and Siebenmorgen, 2012) to calculate the SED of the model; by treating the total dust mass, minimum and maximum dust grain sizes and the density structure of the disc as free parameters we attempt to fit the trends of the SED of VY CMa. We assume the dust grains to be compact spheres with number density $n(a) \propto a^{-3.5}$; the dust is separated into two components – Mg-rich, O-deficient silicates with optical constants from Ossenkopf et al. (1992), and metallic Iron from Fischera (2004).

The SED that best reproduces the observations from the optical to the sub-mm is shown in Fig. 32. Our model SED is most sensitive to the choice of dust mass, grain size and inclination, with other input parameters playing a marginal role. The model fits well from optical-NIR to sub-mm wavelengths, and reproduces the shape of the silicate emission features. The best-fitting model has an inclination of 60° and a position angle of the major axis of the disc is oriented 105° E of N to match Hubble

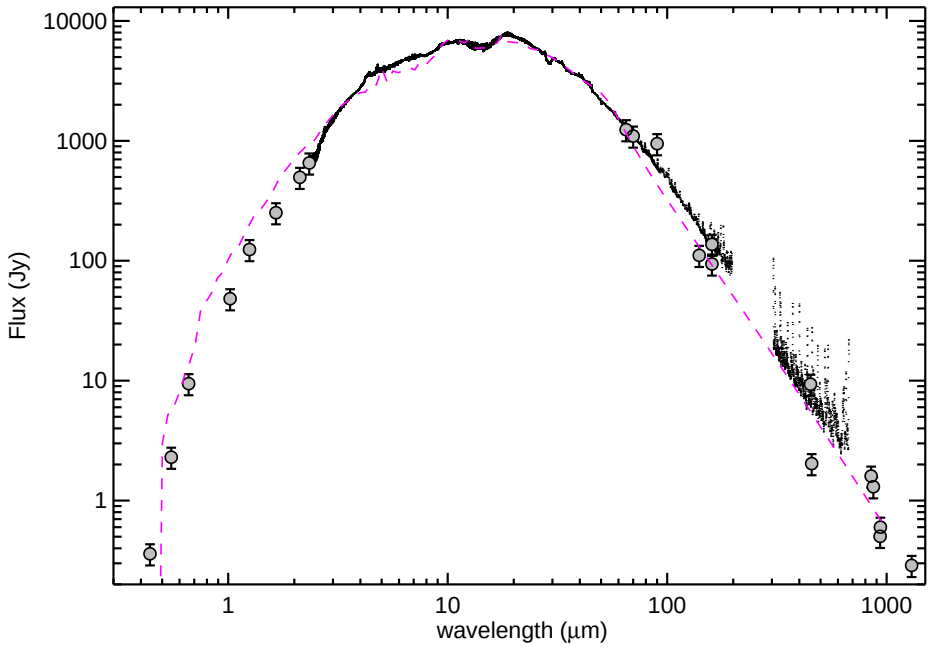

Figure 32: SED of model fit. Photometric data are indicated by grey circles. The black lines indicate spectra from ISO-SWS, ISO-LWS and Herschel-SPIRE. Aperture corrections were applied to the ISO-SWS spectra such that the continuum joins smoothly between the LWS and SWS spectra, and is smooth over the entire wavelength range covered by ISO. The dashed magenta line shows the SED of our model.

Space Telescope images (Smith et al., 2001). As a result, the region NE of the star is viewed through the high obscuration caused by the disc mid-plane. Altering the inclination would enhance the mid-IR emission by allowing a clearer view of the hottest dust, but would result in a dramatic over-prediction of the optical emission, as too much scattered flux would be visible. We find a best-fitting value of p=1.25, implying a decreasing mass-loss rate over the last thousand years, broadly consistent with and Smith et al. (2009a). However, this parameter is poorly constrained when attempting to fit the SED; future work will attempt to include the scattered light images in the fitting process to alleviate this problem.

In order to fit the steep rise in the continuum at $\lambda \sim 3-8\mu$m and the shapes of the silicate features in the mid-infrared, we are forced to use a grain-size distribution with $a_{max} = 8\,\mu$m, producing strong mid-infrared scattering and broad but weak silicate emission. Meanwhile the sub-mm spectral index is dominated by the behaviour of the smallest Fe grains, which allows us to constrain a_{min} to ~ 60 nm.

Based on this model, we infer a total dust mass of $6 \times 10^{-3}\,M_\odot$. This mass is likely to be lower than the true mass, as inhomogeneities will allow very dense regions to "hide" material. Approximately 10% of the dust mass is in the clumps and arcs given by Humphreys et al. (2007), and there are likely to be many more in regions that are not visible in the optical (Smith et al., 2009a). Our dust mass is a factor of 3 lower than that determined by the last major attempt to model the envelope (Harwit et al., 2001), but higher than that determined based on sub-mm interferometry (Muller et al., 2007), although interferometric observations are most sensitive to the compact,

central region of the ejecta. We find that at least 10% of the dust mass is contained in the optically visible clumps, knots and arcs, consistent with previous findings.

6.3 OBSERVATIONS WITH SPHERE

VY CMa was observed in December 2014 using the Spectro-Polarimetric High-contrast Exoplanet REsearch (SPHERE) instrument mounted on the ESO VLT Unit Telescope (UT) 3, as part of the instruments's Science Verification run. SPHERE's primary science goal is to observe Jupiter–like planets around nearby stars, and so is designed to provide extremely high contrast ($> 10^4$) imaging of small fields around bright stars (Beuzit et al., 2008). This is achieved by combining several techniques, including eXtreme Adaptive Optics (XAO), where a high-order deformable mirror is used to correct the effects of atmospheric turbulence (Fusco et al., 2006); coronagraphy, where pupil-plane optics are used to suppress the Point-Spread function (PSF) of the central star and correct any resulting aberations (Boccaletti et al., 2008, e.g.); and differential observing techniques, where different angular, spectral or polarimetric states[1] are subtracted to exploit the expected properties of the observational target (Vigan et al., 2010; Langlois et al., 2014, e.g.).

6.3.1 *Near-infrared imaging with* IRDIS

VY CMa was observed on the night of the 5th of December, 2014 with the InfraRed Dual-band Imager & Spectrograph (IRDIS) sub-instrument of SPHERE. IRDIS is designed to perform high-contrast imaging of young, massive planets in the near-infrared, using differential imaging techniques to achieve contrast as high as 10^6 at 0.5″ from the central star (Dohlen et al., 2008). This is achieved by projecting two beams onto a single 2048×1024 pixel detector, such that each takes up 1024×1024 pixels. In Classical Imaging (CI) mode, both beams are identical, however for improved contrast the beams may be different; for example, in Dual-Band Imaging mode, the two beams are offset in wavelength, so that one beam samples wavelengths where a spectral feature is expected, while the other probes the neighbouring continuum.

VY CMa was placed at the centre of the IRDIS $\sim 12'' \times 11''$ field of view, and used as the Adaptive Optics (AO) reference. The UTs are alt-azimult telescopes, meaning that the field of view rotates as the telescope tracks a target across the sky, and SPHERE is mounted at the Nasmyth platform, meaning that to ensure that the internal geometry of the instrument remains the same during the observations, a derotator must be used to track the orientation of the instrument's pupil[2] to maximise the stability of the PSF on the detector.

Data were taken in the Y- (central wavelength λ_{eff} 1.02 µm), J- (1.25 µm), H- (1.65 µm) and K_S- (2.12 µm) broadband filters, using a coronagraph in CI mode. In each filter, the detector was offset 4 times to positions with successive pixel shifts $\delta x = (0, 0, -1, 0)$ and $\delta y = (0, -1, 0, 1)$ to produce a 2×2 pattern; this process, known as

1 Or some combination of these

2 So-called "pupil–tracking mode". This is different from "field–tracking mode" which tracks the orientation of the field-of-view so that the same position on sky is placed at the same point on the detector. For a Nasmyth instrument, both the field and the pupil rotate differently as the telescope tracks.

dithering is used to correct for bad pixels. At each dither position, 10 frames were recorded, each with a Detector Integration Time (DIT) of 0.837 s, which is the minimum exposure time of the IRDIS detector. For the observations in H-band, the number of frames per dither position was increased to 40, but the DIT remained the same. A nearby patch of empty sky was observed immediately afterwards, with identical DIT but only a single frame in each filter.

These observations were then processed using the Interactive Data Language (IDL). First, the sky frame[3] was subtracted from each frame of VY CMa in the correct band to remove the contribution from background emission. Then, bad pixels were identified from a static bad–pixel map, and their values replaced with the median of all pixels within a 25×25 pixel window, and then with the median of all pixels within a 5×5 pixel window including the value of the bad pixel from the previous averaging step. Next, because pupil tracking allows the field-of-view to rotate on the detector, each frame must be derotated to a common position angle on sky, determined from the parallactic angle of the frame. Having been derotated, the frames at each dither position can be shifted to a common position and stacked to produce a datacube where the z–axis corresponds to the observing sequence. The parts of the cube corresponding to the two halves of the detector were then separated into two cubes, aligned so that the same position on sky has the same (x,y) position and stacked along their z–axes to produce a single $1024 \times 1024 \times 80$ datacube[4]. This cube was then collapsed along the z–axis by taking the median value of each set of frames to produce a single 1024×1024 pixel image in each filter.

Immediately after observing VY CMa, HD59235 was observed in an identical fashion to provide a reference coronagraphic PSF to be subtracted from the observations of VY CMa, enabling clearer identification of structure close to the coronagraph. These data were processed identically to those of VY CMa, and aligned so that the centre of the coronagraph is at the same pixel in both datasets. The resulting PSF frames were then scaled so that an annulus $20\lambda/d$ from the centre of the coronagraph contained equal flux, and the PSF reference images were then subtracted from the images of VY CMa, to produce our final, PSF-subtracted images. The resulting images are shown in Fig. 33.

These data clearly recover all structure seen in previous studies of VY CMa. As expected based on Smith et al. (2001), the nebulosity becomes more compact at longer wavelengths, with the outermost features undetected at K-band, but there is no indication of point–like features that might reveal a companion. This clearly demonstrates the capability of IRDIS to trace features associated with mass–loss variations in nearby RSGs.

6.3.2 *Optical polarimetry with* ZIMPOL

VY CMa was observed on the night of the 8th of December, 2014 with the Zurich IMaging POLarimeter (ZIMPOL) sub-instrument of SPHERE. ZIMPOL is designed to image old Jupiter–like planets at optical wavelengths by detecting the stellar flux scattered by the planet, and is the first imager to exploit XAO at optical wavelengths, potentially providing, for the first time, diffraction limited observations at visual

3 An observation of a region of the sky devoid of stars using the same DIT as the science observations.
4 $1024 \times 1024 \times 320$ in H-band

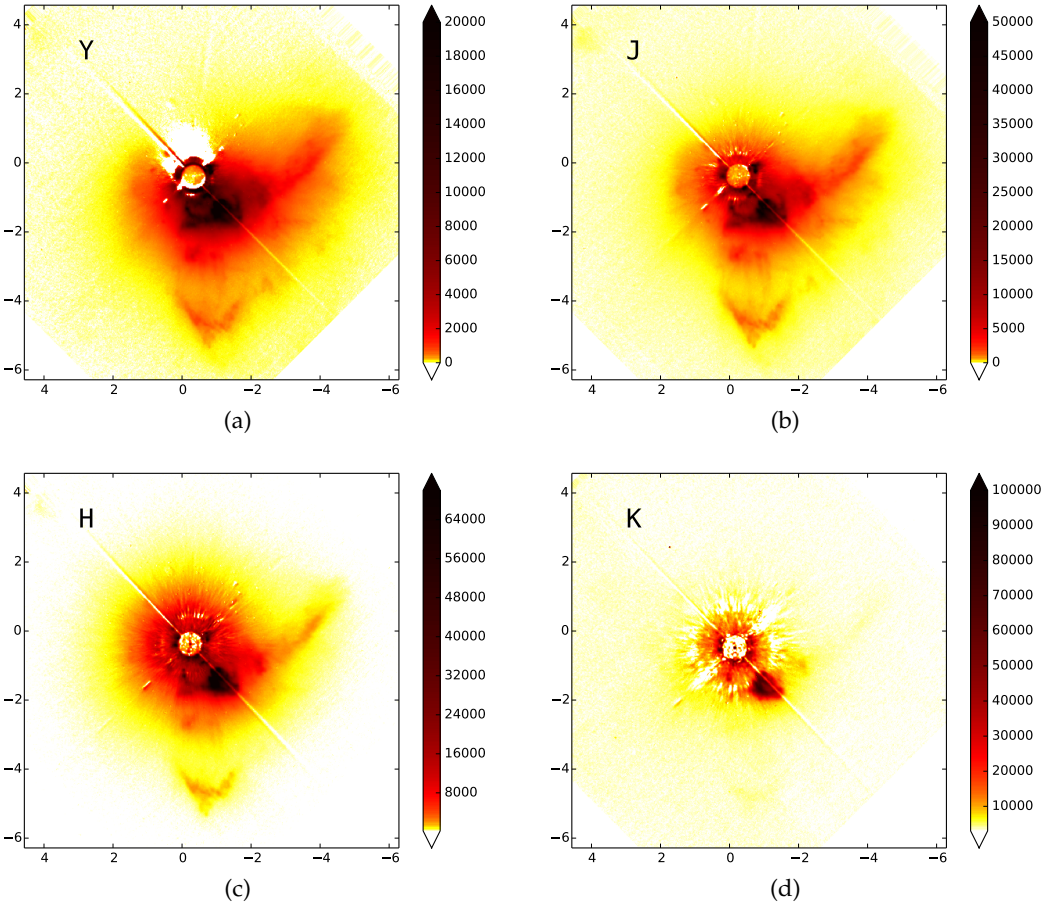

Figure 33: SPHERE Observations. All images are shown with asinh scaling to maximise dynamic range. *a–d*: Near infrared (YJHK) images of VY CMa taken with IRDIS. Colour scales show counts. Residual PSF-subtraction artefacts are visible in the Y- and K-band images. North is up, and East to the left.

wavelengths with a telescope with an 8m mirror (Thalmann et al., 2008). To efficiently separate the flux scattered by the planet from the halo of the stellar PSF, ZIMPOL exploits polarimetric imaging to suppress the unpolarised stellar emission; combined with coronagraphy, this allows contrasts of up to 10^9 at separations of (). To provide unparalleled polarimetric precision, ZIMPOL exploits high–frequency charge–shifting detectors and rapid polarisation modulation, so that the ordinary and extraordinary rays are imaged quasi-simultaneously on the same detector pixels having travelled the same light path. This negates noise relating to changes in ambient conditions, pixel response or optical paths. Furthermore, ZIMPOL images simultaneously on two identical detectors; the images from both can either be combined to improve the signal–to–noise ratio or can be used to remove detector effects.

VY CMa was observed in V-band ($\lambda_{\rm eff}$ 554 nm) and narrow I-band ($\lambda_{\rm eff}$ 816.8 nm) filters using a Classical Lyot Coronagraph (CLC) with diameter 155 mas to supress the stellar PSF. Both detectors were exposed in the same filter simultaneously so that the exposure time could be adjusted for optimal exposure in both filters. VY CMa is very bright ($m_V \sim 7$), so observations were taking with fast polarisation modulation (~1 kHz) to minimise atmospheric effects at the expense of sensitivity. The rotation of the instrument was compensated for using the active field derotation mode, in which an additional half-wave plate is used to ensure that the polarisation orientation remains constant, at the expense of increased instruental polarisation ($\sim$ 0.5% rather than $\sim$ 0.1%); this was deemed acceptable as previous polarimetric observations (Jones et al., 2007) of VY CMa have shown extremely high polarisation fractions such that any instrumental signal is negligible. To ensure the best possible calibration, the polarisation state was observed at 4 orientations, $0°, 45°, 90°, 135°$, corresponding to Stokes parameters +Q, +U, -Q, and -U, where a negative Stokes parameter is observed with a reference direction rotated by 90° and hence the reference directions of the O- and E-rays are switched.

The resulting data was reduced using the v 0.14 of the SPHERE pipeline. Bias and dark–current subtraction was performed, followed by intensity flat–fielding. The pipeline then reconstructs the positive and negative Q & U signals for each detector, along with the Stokes I signal for each observation. Then, an overall Q signal is derived from each detector using $Q = 0.5\,(+Q - -Q)$, and similarly for U. The resulting I, Q and U images from each detector were then co-added in python, before determining images of the polarised intensity, polarisation fraction and polarisation angle.

As with the IRDIS observations, a PSF reference star was observed immediately after the ZIMPOL observations of VY CMa. However, PSF subtraction was found to provide only minor benefits in the intensity images and no benefit in polarisation. As PSF subtraction can also introduce artefacts, further analysis is based on the unsubtracted images to avoid contamination at the expense of contrast within $\sim$ 300 mas of the star.

Figure 34 shows the images obtained in both polarised and unpolarised intensity. The polarisation images show a clear centro-symmetric pattern, indicating that the polarisation is caused by the scattering of light by dust grains. As a result, we can use the fractional polarisation and the intensity ratio to constrain the properties of the scattering dust, in particular the size distribution of the grains. The very high maximum polarisation degree ($\sim$ 0.5) indicates the presence of grains with radii similar to the wavelength of the observations ($\geqslant$100 nm), so we calculate the maximum

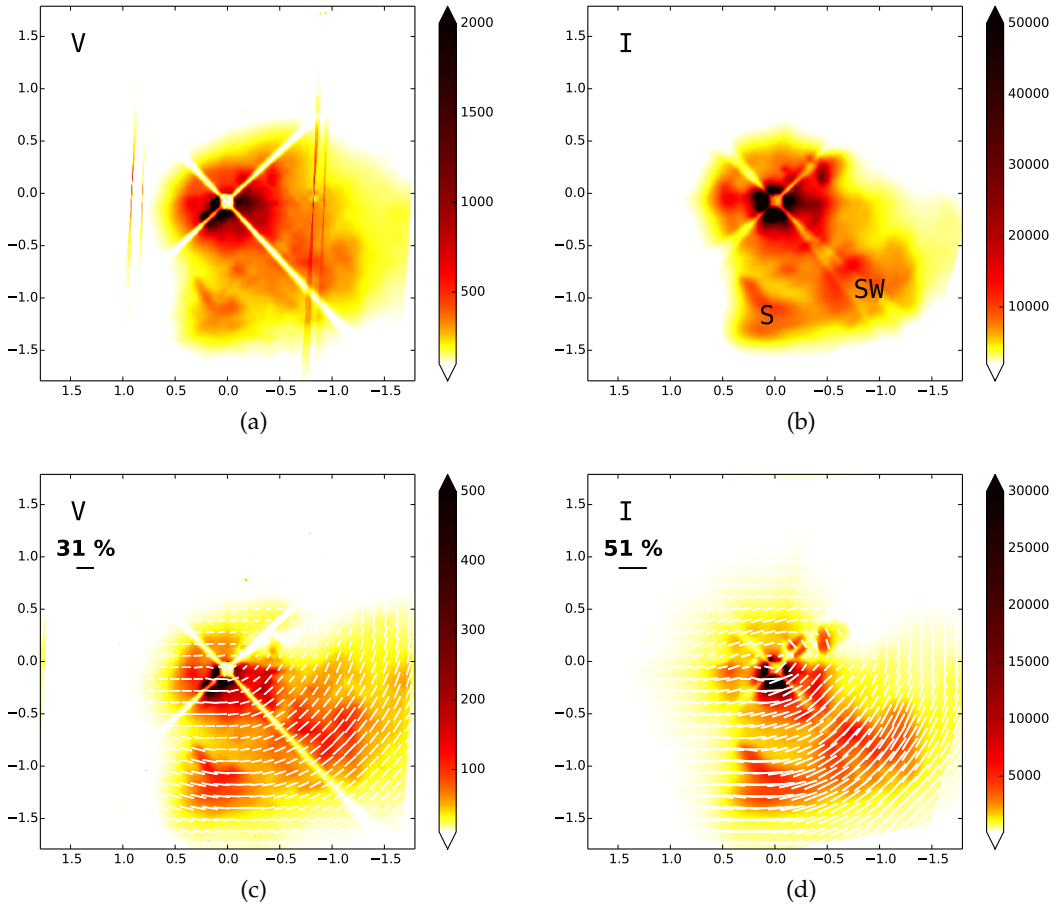

Figure 34: Coronagraphic imaging polarimetry of VY CMa. *Top:* Intensity observations. *Bottom:* Polarised intensity, with polarisation direction and fraction shown in the overlaid vector field. Offsets from the central star are shown in arcseconds, and the colour scale in arbitrary units, with the observing filter in the top-left corner. The contrast is noticeably higher in polarised intensity, as the stellar halo is only weakly polarised. This allows a clearer identification of circumstellar material, and separation into discrete structures. The positions of the South Knot (S) and Southwest Clump (SW) are indicated in the I band intensity image. One arcsecond corresponds to a projected distance of approximately 200 stellar radii. The low-intensity cross is produced by the suspended coronagraphic mask which obscures part of the image plane, while the stripe-like artefacts in the V-band image results from a detector bias effect which cancels out in the polarised signal.

likelihood values of the minimum (a_{min}) and maximum (a_{max}) radii for a grain size distribution, assuming oxygen-deficient silicates (Ossenkopf et al., 1992), which is described in the following section.

6.4 GRAIN-SIZE DISTRIBUTION FITTING

In order to calculate the maximum likelihood grain-size distribution, the scattering and polarising properties of a grid of dust models are calculated under the assumption of Mie scattering (Mie, 1908) by bare, compact spheres, which allows us to fit the observations under the assumption of single scattering. A grain size distribution of the form $n(a) \propto a^{-q}$ is assumed, where a is the grain radius and $n(a)$ is the number density of grains with radius a. The lower- (a_{min}) and upper- (a_{max}) size limits are free parameters, and the exponent of the grain size distribution is fixed to $q = -3.5$. For each size distribution, the scattering and absorption cross-sections, and the components of the Müller matrix at one degree intervals, are calculated for each wavelength for which the observations will be fitted.

The polarisation fraction at each wavelength is completely determined by the elements of the Müller matrix, such that $p(\lambda, \theta) = |M_{12}(\lambda, \theta)/M_{11}(\lambda, \theta)|$, where p is the polarisation fraction, λ is the wavelength of interest, θ is the scattering angle, and M_{ij} are the elements of the Müller matrix.

The ratio of the scattered intensities at any pair of wavelengths is determined by the scattering phase function, contained within M_{11}, and the ratio of the scattering efficiencies, i.e.

$$r_I(\theta) = I(\lambda_1, \theta)/I(\lambda_2, \theta) = (Q_{sca}(\lambda_1)/Q_{sca}(\lambda_2)) \times (M_{11}(\lambda_1, \theta)/M_{11}(\lambda_2, \theta)) \times (F_*(\lambda_1)/F_*(\lambda_2)),$$

where F_* is the flux emitted by the star and Q_{sca} are the scattering efficiencies.

For each grain-size distribution, we calculate the likelihood

$$\mathcal{L}(\Theta) = \prod L_i(\Theta, \Delta_i)$$

$$\mathcal{L}(\Theta) = \prod \frac{\sigma_{\Delta_i}}{2\pi} \exp\left(\frac{-1}{2\sigma^2_{\Delta,i}}(\Delta_i - M_i(\Theta))^2\right)$$

where Δ is a vector of observations such that Δ_i is the *i*th observation and σ_{Δ_i} its associated uncertainty, M_i is the output of the model associated with the *i*th observation, and Θ is a vector of model parameters (in our case $\Theta = (a_{min}, a_{max})$). The maximum-likelihood model is then defined to be the model with parameters Θ that maximises the value of $\mathcal{L}(\Theta)$, and Θ contains the information in which we are interested.

For the sake of efficiency, it is common to compute the log-likelihood

$$\mathrm{Log}(\mathcal{L}(\Theta)) = \sum \frac{-1}{2\sigma^2_{\Delta,i}}(\Delta_i - M_i(\Theta))^2$$

by taking only the exponent.

By calculating a grid of grain-size distributions with $5\,\mathrm{nm} < a_{min} \leqslant 1\,\mu\mathrm{m}$ and $100\,\mathrm{nm} < a_{max} \leqslant 50\,\mu\mathrm{m}$ the full range of grain sizes observed in the interstellar medium and in the circumstellar environments of evolved stars is covered.

The average size of the maximum-likelihood distribution is calculated simply from

$$\langle a \rangle = \int_{a_{min}}^{a_{max}} a n(a)\,da \Big/ \int_{a_{min}}^{a_{max}} n(a)\,da$$

$$\langle a \rangle = \int_{a_{min}}^{a_{max}} a^{q+1}\,da \Big/ \int_{a_{min}}^{a_{max}} a^{q}\,da,$$

which can be solved analytically.

Because the scattering properties are determined by the real part of the complex refractive index of the grain material, which is similar for all of the plausible choices, the final grain size distribution does not depend on the choice of grain composition.

Several regions within the ejecta are considered separately. Previous studies (Humphreys et al., 2007; Jones et al., 2007; Muller et al., 2007; Smith et al., 2009a) have shown that VY CMa's mass-loss envelope consists of a number of fast-moving, randomly-directed ejection events ("clumps") and slower, steady, equatorially-enhanced mass-loss (the "disc"); these studies have determined the 3-dimensional geometry of the envelope, which we exploit to determine grain sizes. The clumps are seen as distinct features in both intensity and polarisation, while the disc is seen via the diffuse, polarised flux surrounding the star.

Beginning with the disc, a scattering angle of 133° is assumed for the far side of the disc surface based on the inclination of the above radiative transfer model. The minimum grain radius shows a distinct region of increased likelihood between 0.1 and 1 μm, with a best-fitting value of 400 nm. Although the value of a_{max} is not as well constrained, it favours values around 1 μm, with a formal best-fit at 600 nm. This gives an average grain size of 475 nm, a factor of 50 larger than grains in the diffuse interstellar medium.

Two clumps are also examined, the South Knot and the Southwest Clump (see Fig 34). The angle joining the star, the South Knot and the observer is 117° (Humphreys et al., 2007), giving a scattering angle of 63°. The parameter space has two regions which produce good fits, one with $a_{max} \leqslant 300\,\mathrm{nm}$ and a_{min} unconstrained, and another with $200\,\mathrm{nm} \leqslant a_{min} \leqslant 1\,\mu\mathrm{m}$ and a_{max} unconstrained, while the maximum likelihood model has a narrow range of sizes between 300 nm and 350 nm. The Southwest Clump, with a scattering angle of 98° (Humphreys et al., 2007), shows similar behaviour, but with the maximum likelihood model ($a_{min} = 450\,\mathrm{nm}$, $a_{max} = 550\,\mathrm{nm}$) offset from the main region of increased likelihood at $a_{min} \sim 200\,\mathrm{nm}$, $a_{max} \sim 300\,\mathrm{nm}$. However, as these regions may be optically thick, multiple scattering may play a role, reducing the observed polarisation fraction in these regions, which implies that our grain sizes are lower limits. As such, while this indicates differences between the quiescent and clump phases, polarimetric observations in the near-infrared – where the clumps are optically thin – would provide confirmation.

6.4.1 *The role of multiple scattering*

Previous studies (Shenoy et al., 2013, 2015) have suggested that the clumps in the ejecta have optical depths that make the single-scattering approximation inappropri-

ate. This limit is typically set at $\tau_{sca} \sim 0.2$, where Poisson statistics show that 10% of scattered photons have been multiply scattered. However, as the alternative is computationally intensive Monte Carlo radiative transfer model fitting, the single scattering approximation is an acceptable solution, provided that the effects of multiple scattering are understood. In general, multiple scattering introduces depolarisation, reducing the observed degree of polarisation. In the case of forward scattering (e.g.the South Knot) p typically increases for larger grains, meaning that our size determination is a lower limit. However, for backward-scattering regions, depolarisation would imply the grains are in fact smaller. Therefore we can place robust constraints on the grain size distribution in all cases.

Moreover, given the very high observed polarisation fractions, any depolarising effect cannot be large (Shenoy et al., 2015). This further implies that, even if there is a significant fraction of multiply-scattered photons, the *observed* polarisation does not deviate significantly from single scattering. Hence, our size estimates remain robust.

Finally, the aforementioned works (Shenoy et al., 2013, 2015) assumed that all of the ejecta is illuminated by the same spectrum that we observe. However, given the probable geometry, the regions where we are attempting to measure the grain size are illuminated by a considerably stronger flux in the wavelength ranges used to measure their optical depth than one infers based on the observed spectrum. This means that significantly less material is required to produce the observed scattered flux, and hence the optical depths are lower than previously inferred, making the single-scattering approximation acceptable.

6.5 DISCUSSION

6.5.1 *Grain sizes*

The presence of large dust grains is inferred from two distinct methods, radiative-transfer-model fitting and by fitting the scattering and polarimetric properties of dust grains. Each method is most sensitive to grains with sizes close to the observing wavelength, and the fits to the optical polarimetry often do not constrain a_{max} well. As a result, RT modelling is more sensitive to grains $> 1\mu m$.

The presence of large dust grains indicates that radiative acceleration via scattering plays a significant role in driving the wind, as found for AGB stars (Norris et al., 2012). RSGs typically have small pulsation amplitudes, the regime in which this mechanism was found to be most effective for AGB stars (Norris et al., 2012), as the weak pulsations are less likely to levitate material to the large radii required for iron-rich silicates to form. This effect is likely to be strongest for grains with size $\sim 500\,nm$ (Höfner, 2008; Bladh and Höfner, 2012), which agrees closely with the best-fitting size we find in the 'disc' component. This indicates that grain-growth processes are equally efficient in RSG outflows as in their lower-mass cousins. However, the grains in the fast moving clumps, being smaller than those in the disc, would receive less radiation pressure. Their higher velocity therefore requires that they have received additional acceleration at or prior to dust formation. Previous studies (Humphreys et al., 2007; Jones et al., 2007; Muller et al., 2007; Smith et al., 2009a; Richards et al., 2014; O'Gorman et al., 2015) have inferred a role for magnetic fields in producing the clumps and their seemingly random distribution, analogous to our Sun's Coro-

nal Mass Ejections; energy liberated from the magnetic field that shaped them (e.g. via magnetic reconnection) therefore seems a natural source of kinetic energy for the clumps. The resulting increased velocity would therefore allow less time for grain growth in the clumps, and might encourage collisions, increasing the rate of grain destruction.

6.5.2 *Dust-to-gas ratio and mass-loss history*

The gas-to-dust ratio of the ejecta is poorly constrained for evolved stars, but assumed values generally lie in the range 200 – 500; this implies that the total mass of the ejecta is around 5 – 10% of the initial mass of the star, at between $1.2\,M_\odot$ and $3\,M_\odot$. Our observations are sensitive to the last $\sim$ 1000 yr of mass loss; such a high ejecta mass therefore requires a time-averaged mass-loss rate in excess of $10^{-3}\,M_\odot\,yr^{-1}$, substantially higher than many previous estimates, although similar to the 'quiescent' mass-loss rate found by O'Gorman et al. (2015). However if, as indicated by Smith et al. (2009a) and our best-fitting value for p, the mass-loss rate has been in decline for the past millenium, it is likely that the majority of this mass-loss is accounted for by the large outburst that is proposed to have occurred 1000–1500 years ago (Humphreys et al., 2007).

On the other hand, some of the lower estimates have come from sub-mm single-dish observations of CO lines. These have rather poor angular resolution, and hence, by integrating over a large beam, are sensitive to longer timescales and so have a large contribution from pre-outburst mass-loss. This reduces the average mass-loss rate.

Given the gradient of the density distribution of the radiative transfer model, one expects a time-dependent mass-loss rate, i.e. $\dot{M} \propto t^{-0.75}$ if the outflow velocity is assumed to be constant. Assuming that the model is sensitive to all the mass lost since the ouburst, that this outburst occurred exactly 1000 years ago and a gas-to-dust ratio of 200, this implies a present–day mass–loss rate of $3 \times 10^{-4}\,M_\odot\,yr^{-1}$, consistent with the lower determinations of VY CMa's mass-loss rate. The same assumptions imply that the mass-loss rate during the outburst may have been as high as $0.05\,M_\odot\,yr^{-1}$, comparable to the 1890 eruption of η Carina.

6.5.3 *VY CMa as a supernova progenitor*

At some point, VY CMa will explode as a supernova. When this occurs, the dust envelope has the potential to drastically alter the appearance of the explosion, depending on the evolution of both the star and the envelope between now and the explosion. However, VY CMa's initial mass is highly uncertain, with estimates covering the range 20–35 $M_\odot$ (Wittkowski et al., 2012), although previous estimates covered an even wider range (Smith et al., 2001; Massey et al., 2006). As a result, VY CMa may evolve into a Yellow Hypergiant similar to IRC +10420, followed by a Blue Supergiant, resulting in a type II-L supernova rather similar in appearance to SN 1987A if the disc structure is still present. This would be a relatively short process, with the evolution toward a supernova lasting roughly 10,000 yr (Smith et al., 2009a). Alternatively, if its mass lies toward the upper end of the range, it is more likely to evolve into a Wolf–Rayet star, with the fast wind then sweeping the existing envelope into a distant shell.

This uncertainty makes it difficult to determine the outcome of a supernova, and so several potential scenarios are outlined below.

If VY CMa were to explode now, the blast wave would collide with the mass–loss envelope almost immediately, and would take approximately 5 yr to traverse the ~ 6000 AU containing the last 1000 yr of mass loss, assuming a speed of $V_{SN} = 5000\,km\,s^{-1}$ for the blast wave. Following the formalism of Smith et al. (2009a) we can estimate the maximum luminosity of the interaction, beginning with the wind–density parameter at the base of the wind, which can be calculated using the present–day mass–loss rate derived above. This suggests that the initial rate of conversion of kinetic energy to radiation could liberate ~ 10^8 $L_\odot$ in the immediate aftermath of the explosion, similar to the peak luminosity of a SN II–P. Thanks to the shallow density exponent derived above, this would decay rather slowly over the following ~ 5 yr until the shock wave overran the outer edge of the last 1000 yr of mass loss. As suggested by Smith et al. (2009a), this would result in obvious signs of supernova shock interaction and a long-lasting supernova, but would not produce a superluminous supernova.

Assuming that VY CMa doesn't have further extreme mass–loss events before its explosion, then any other scenario will result in fainter Circumstellar Medium (CSM) interaction than above. In ~10,000 yr the present ejecta will be rather distant and diffuse, meaning that the interaction between the blast wave and the CSM would not occur for ~ 50 yr and would be orders of magnitude less luminous. Nevertheless, this would become visible, particularly in X-rays, similar to the rings of SN 1987A (Larsson et al., 2011). If VY CMa evolves into a Wolf–Rayet then the influence of the wind–swept shell may be even more difficult to detect, with an even longer delay between explosion and interaction.

The large grains we have observed are substantially more likely to survive the supernova explosion that will eventually consume VY CMa. These grains would survive sublimation by the supernova radiation ~ 50% closer to the star than ISM grains (Gall et al., 2014), substantially altering the amount of dust to survive the explosion. As discussed above, the future evolutionary path of VY CMa is highly uncertain, however if the explosion will not occur for at least 10,000 yr then all of the ~ 10^{-2} $M_\odot$ of dust formed so far (Harwit et al., 2001; Muller et al., 2007) will be injected into the ISM given the present outflow velocity. Although this is small compared to the dust mass in SN 1987A (Wesson et al., 2015), it is non-negligible compared to other supernova remenants (Gall et al., 2011). If VY CMa's dust is typical, pre-supernova mass-loss would make a meaningful contribution to the dust budget at high-redshift.

6.5.4 *The Nebulae and Ejecta of Massive Evolved Stars optical and Infrared Survey*

Based on their success in resolving structure in the ejecta and determining grain sizes, the observations presented in this chapter have been used as a blueprint for a larger programme of observations of RSGs. This programme has so far been awarded 56 hr of observing time on SPHERE, to observe a sample of bright southern and equatorial RSGs.

By conducting high–contrast imaging of such a sample, it will for the first time be possible to reliably locate similar clumpy or filamentary structures to VY CMa in the winds of other RSGs. This will reveal whether the magnetically–driven mass–loss

believed to be responsible for the structure around VY CMa is the normal mode of mass loss in RSGs or if VY CMa and objects like it are a distinct sub–class. Optical polarimetric imaging, on the other hand, will reveal grain sizes across the sample, allowing a thorough determination of the typical grain size in RSG winds.

Together, this will provide key insights into pre-supernova mass loss, and the survival of RSG dust in supernovae. This will make it possible to robustly constrain the dust contribution of RSGs to the ISM in a statistically relevant manner for the first time.

6.6 SUMMARY

We have presented a new radiative transfer model for the nearby RSG VY CMa along with new observations from the XAO imager SPHERE. These probe the last ~1000 yr of stellar mass loss through both the thermal emission and scattered radiation of the dusty circumstellar envelope.

Radiative transfer modelling reveals that the total dust mass of the ejecta is $\sim 6 \times 10^{-3}\,M_\odot$, suggesting a total ejecta mass $\gtrsim 1\,M_\odot$. It also concurs with previous results indicating that the mass-loss rate has been decreasing since a major outburst ~ 1000 yr ago.

Based on a combination of radiative transfer modelling and fits to the grain properties we have inferred the presence of dust grains $\gtrsim$ 50 times larger than those in the ISM. Such large grains would efficiently scatter the stellar radiation, even if the absorption efficiencies at the same wavelengths are negligible. As a result, a significant amount of radiation pressure would be exerted on the grains by scattering, potentially explaining puzzling observations of the wind acceleration. The somewhat smaller grain sizes determined for the dense clumps in the ejecta is consistent with models in which the shaping and ejection of these clumps is related to magnetic activity.

The chances of grains this large surviving the eventual explosion of VY CMa are significantly higher than for small ISM–like dust. If VY CMa's dust is typical of RSGs then each RSG may contribute up to a few $\times 10^{-2}\,M_\odot$ of dust to the ISM before their explosion. This is a significant fraction of the 0.1–1 $M_\odot$ per supernova required to explain large dust reservoirs in the early universe, indicating that pre-supernova mass loss may help to explain this puzzle.

We also explore whether the ejecta is sufficient to power a superluminous supernova in the event of VY CMa's explosion through the interaction of the supernova shock with the circumstellar nebulosity.

7

CONCLUDING REMARKS

7.1 SUMMARY

This thesis has presented four detailed studies on dusty environments. These studies have exploited numerical modelling, primarily radiative transfer, to interpret new and existing observations relating to the interstellar medium, star & planet formation and evolved stars.

In chapter 3 the influence of clumpiness on interstellar extinction is explored, confirming previous results that inhomogeneities result in the flattening of the extinction curve. Furthermore, the degree of flattening is shown to be correlated with the wavelength at which the clumps become optically thick, rather than the optical depth of the clumps as previously suggested. As well as changing the strength of extinction bumps, clumpiness is shown to alter the shape and location of features in the extinction curve; however, features produced purely by scattering are robust against the effects of clumpiness. On the other hand, the shape of the scattered continuum radiation is shown to change significantly, with the short-wavelength continuum becoming relatively weaker as the optical depth of the clumps increases, potentially offering an alternative explanation for observations of "coreshine". However, it is shown that these effects are only important for observations of embedded young or evolved stars or extragalactic sources where unresolved optically thick structure is within the observing beam; for observations of the galactic diffuse ISM these can be ignored.

Chapter 4 presents a novel model to explain observations of "old" pre-main-sequence stars with on going accretion and infrared excess characteristic of young stars. It is shown that, by passing through a dense clump within their parent molecular cloud, stars that have already lost their primordial disc may accrete enough material to form a new circumstellar disc with similar properties to primordial discs, and that the probability of such encounters is non–negligible. Such a scenario may have far–reaching consequences for the formation of planets and the evolution of young planetary systems. Disc reformation may allow for a second epoch of planet formation as the new disc evolves. Alternatively, existing planetary systems may be re-arranged or even destroyed by chaotic interactions with inflowing material.

The interpretation of high-resolution interferometric observations of the binary YSO VV CrA is explored in chapter 5. By comparing observations to a grid of 1.5 million radiative transfer models, we show that... By combining the results of the modelling with near-infrared spectroscopic observations, an accretion rate of $4 \times 10^{-8}\,\mathrm{M_\odot\,yr^{-1}}$ is determined.

The most detailed modelling and observations to date of the nearby extreme RSG VY CMa are presented in chapter 6. Detailed three-dimensional radiative transfer modelling of VY CMa's mass-loss envelope shows that it has produced $\sim 6 \times 10^{-3}\,\mathrm{M_\odot}$ of dust in the past 1000 yr alone, suggesting that, in the same period, it has ejected 5–10% of its initial stellar mass. High-contrast optical imaging polarimetry from the

novel XAO instrument SPHERE provide the clearest picture of the ejecta ever obtained. Based on these observations, the average size of dust in the envelope is inferred to be 50 times larger than dust in the interstellar medium. Grains of this sizes are significantly more likely to survive the supernova that will eventually consume VY CMa; as a result, VY CMa may inject $\sim 10^{-2}\,M_{\odot}$ of dust into the ISM, suggesting that RSGs may make a significant contribution to dust reservoirs in the early universe.

7.2 OUTLOOK

This is an exciting time in the study of cosmic dust, with cutting edge facilities producing a steady stream of new results and an array of future observatories on the horizon. Meanwhile, new models are being developed to explain these observations and provide the predictions required to target future observations.

A number of new observing facilities have recently become available that will continue to produce new insights over the coming decades. Chapter 6 has demonstrated the ability of XAO instruments to provide key constraints on the close environments of evolved stars, where a significant fraction of dust formation in the universe takes place. SPHERE and similar instruments are poised to reveal the properties of newly formed dust around a wide range of AGB and RSG stars, along with the influence of environment upon the dust–formation process. Simultaneously, the unparalleled resolution of ALMA allows it to produce complementary constraints at long wavelengths, where optical–depth effects can be neglected. These can be complemented with mid-infrared observations from current and future observatories (e.g. the James Webb Space Telescope) to detect changes in dust composition over time through the characteristic emission features around 10 & 20 μm.

Meanwhile, these suites of instruments will continue to cast new light on the star– and planet–formation processes. By probing the presence of both micron– and millimetre–sized grains in protoplanetary discs, it is now possible to follow the initial stages of the grain–growth processes required for planet formation. In the near future, the Square Kilometre Array will trace grains up to cm–m sizes, providing even stronger constraints on grain growth into the regime of pebbles, allowing the onset of planet formation to be traced directly. In parallel, 30m–class optical and infrared telescopes will allow observations of the formation regions of earth–like planets to be observed directly at short wavelengths.

However, as illustrated in chapter 4, it will also be important to understand the interaction of existing planetary systems with the accretion of new material onto the system. As chaotic systems, a substantial increase in the mass of the system could have a destabilising effect, triggering migration or multiple collisions. Understanding the outcomes of such interactions will require detailed N–body & hydrodynamical calculations, including the gravitational influence of the gas on the planets.

BIBLIOGRAPHY

J. M. Alcalá, A. Natta, C. F. Manara, L. Spezzi, B. Stelzer, A. Frasca, K. Biazzo, E. Covino, S. Randich, E. Rigliaco, L. Testi, F. Comerón, G. Cupani, and V. D'Elia. X-shooter spectroscopy of young stellar objects. IV. Accretion in low-mass stars and substellar objects in Lupus. *A&A*, 561:A2, January 2014. doi: 10.1051/0004-6361/201322254. (Cited on page 67.)

R. Andrae. Error estimation in astronomy: A guide. *ArXiv e-prints*, September 2010. (Cited on page 61.)

P. Andre, D. Ward-Thompson, and M. Barsony. Submillimeter continuum observations of Rho Ophiuchi A - The candidate protostar VLA 1623 and prestellar clumps. *ApJ*, 406:122–141, March 1993. doi: 10.1086/172425. (Cited on page 19.)

P. André, J. Di Francesco, D. Ward-Thompson, S.-I. Inutsuka, R. E. Pudritz, and J. E. Pineda. From Filamentary Networks to Dense Cores in Molecular Clouds: Toward a New Paradigm for Star Formation. *Protostars and Planets VI*, pages 27–51, 2014. doi: 10.2458/azu_uapress_9780816531240-ch002. (Cited on page 59.)

S. Antoniucci, R. García López, B. Nisini, T. Giannini, D. Lorenzetti, J. Eislöffel, F. Bacciotti, S. Cabrit, A. Caratti o Garatti, C. Dougados, and T. Ray. POISSON project. I. Emission lines as accretion tracers in young stellar objects: results from observations of Chamaeleon I and II sources. *A&A*, 534:A32, October 2011. doi: 10.1051/0004-6361/201117454. (Cited on page 63.)

A. Appel. Some techniques for shading machine renderings of solids. *AFIPS Conference Proc.*, 32:37–45, 1968. (Cited on page 35.)

I. Appenzeller, R. Jetter, and I. Jankovics. A high resolution atlas of two T Tauri stars. *A&AS*, 64:65–104, April 1986. (Cited on page 60.)

P. J. Armitage. *Astrophysics of Planet Formation*. 2010. (Cited on page 20.)

P. J. Armitage. Dynamics of Protoplanetary Disks. *ARA&A*, 49:195–236, September 2011. doi: 10.1146/annurev-astro-081710-102521. (Cited on pages 19 and 55.)

B. Arroyo-Torres, M. Wittkowski, A. Chiavassa, M. Scholz, B. Freytag, J. M. Marcaide, P. H. Hauschildt, P. R. Wood, and F. J. Abellan. What causes the large extensions of red supergiant atmospheres?. Comparisons of interferometric observations with 1D hydrostatic, 3D convection, and 1D pulsating model atmospheres. *A&A*, 575:A50, March 2015. doi: 10.1051/0004-6361/201425212. (Cited on pages 22, 83, and 84.)

G. Beccari, L. Spezzi, G. De Marchi, F. Paresce, E. Young, M. Andersen, N. Panagia, B. Balick, H. Bond, D. Calzetti, C. M. Carollo, M. J. Disney, M. A. Dopita, J. A. Frogel, D. N. B. Hall, J. A. Holtzman, R. A. Kimble, P. J. McCarthy, R. W. O'Connell, A. Saha, J. I. Silk, J. T. Trauger, A. R. Walker, B. C. Whitmore, and R. A. Windhorst.

Progressive Star Formation in the Young Galactic Super Star Cluster NGC 3603. *ApJ*, 720:1108–1117, September 2010. doi: 10.1088/0004-637X/720/2/1108. (Cited on pages 51 and 54.)

S. V. W. Beckwith, T. Henning, and Y. Nakagawa. Dust Properties and Assembly of Large Particles in Protoplanetary Disks. *Protostars and Planets IV*, page 533, May 2000. (Cited on page 21.)

C. P. M. Bell, T. Naylor, N. J. Mayne, R. D. Jeffries, and S. P. Littlefair. Pre-main-sequence isochrones - II. Revising star and planet formation time-scales. *MNRAS*, 434:806–831, September 2013. doi: 10.1093/mnras/stt1075. (Cited on page 51.)

J.-L. Beuzit, M. Feldt, K. Dohlen, D. Mouillet, P. Puget, J. Antichi, A. Baruffolo, P. Baudoz, A. Berton, A. Boccaletti, M. Carbillet, J. Charton, R. Claudi, M. Downing, P. Feautrier, E. Fedrigo, T. Fusco, R. Gratton, N. Hubin, M. Kasper, M. Langlois, C. Moutou, L. Mugnier, J. Pragt, P. Rabou, M. Saisse, H. M. Schmid, E. Stadler, M. Turrato, S. Udry, R. Waters, and F. Wildi. SPHERE: A 'Planet Finder' Instrument for the VLT. *The Messenger*, 125:29, September 2006. (Cited on page 83.)

J.-L. Beuzit, M. Feldt, K. Dohlen, D. Mouillet, P. Puget, F. Wildi, L. Abe, J. Antichi, A. Baruffolo, P. Baudoz, A. Boccaletti, M. Carbillet, J. Charton, R. Claudi, M. Downing, C. Fabron, P. Feautrier, E. Fedrigo, T. Fusco, J.-L. Gach, R. Gratton, T. Henning, N. Hubin, F. Joos, M. Kasper, M. Langlois, R. Lenzen, C. Moutou, A. Pavlov, C. Petit, J. Pragt, P. Rabou, F. Rigal, R. Roelfsema, G. Rousset, M. Saisse, H.-M. Schmid, E. Stadler, C. Thalmann, M. Turatto, S. Udry, F. Vakili, and R. Waters. SPHERE: a 'Planet Finder' instrument for the VLT. In *Society of Photo-Optical Instrumentation Engineers (SPIE) Conference Series*, volume 7014 of *Society of Photo-Optical Instrumentation Engineers (SPIE) Conference Series*, page 18, July 2008. doi: 10.1117/12.790120. (Cited on page 87.)

J. E. Bjorkman and K. Wood. Radiative Equilibrium and Temperature Correction in Monte Carlo Radiation Transfer. *ApJ*, 554:615–623, June 2001. doi: 10.1086/321336. (Cited on pages 12 and 31.)

S. Bladh and S. Höfner. Exploring wind-driving dust species in cool luminous giants. I. Basic criteria and dynamical models of M-type AGB stars. *A&A*, 546:A76, October 2012. doi: 10.1051/0004-6361/201219138. (Cited on pages 84 and 94.)

A. Boccaletti, L. Abe, J. Baudrand, J.-B. Daban, R. Douet, G. Guerri, S. Robbe-Dubois, P. Bendjoya, K. Dohlen, and D. Mawet. Prototyping coronagraphs for exoplanet characterization with SPHERE. In *Society of Photo-Optical Instrumentation Engineers (SPIE) Conference Series*, volume 7015 of *Society of Photo-Optical Instrumentation Engineers (SPIE) Conference Series*, page 1, July 2008. doi: 10.1117/12.789341. (Cited on page 87.)

C. F. Bohren and D. R. Huffman. *Absorption and scattering of light by small particles*. 1983. (Cited on pages 9 and 31.)

H. Bondi. On spherically symmetrical accretion. *MNRAS*, 112:195, 1952. (Cited on page 52.)

H. Bondi and F. Hoyle. On the mechanism of accretion by stars. *MNRAS*, 104:273, 1944. (Cited on page 52.)

J. Bouwman, G. Meeus, A. de Koter, S. Hony, C. Dominik, and L. B. F. M. Waters. Processing of silicate dust grains in Herbig Ae/Be systems. *A&A*, 375:950–962, September 2001. doi: 10.1051/0004-6361:20010878. (Cited on page 21.)

H. Bouy, J. Alves, E. Bertin, L. M. Sarro, and D. Barrado. Orion revisited. II. The foreground population to Orion A. *A&A*, 564:A29, April 2014. doi: 10.1051/0004-6361/201323191. (Cited on page 57.)

G. Bruzual A., G. Magris, and N. Calvet. A model for the effects of dust on the spectra of disk galaxies. I - General treatment. *ApJ*, 333:673–688, October 1988. doi: 10.1086/166776. (Cited on page 28.)

D. Calzetti, A. L. Kinney, and T. Storchi-Bergmann. Dust extinction of the stellar continua in starburst galaxies: The ultraviolet and optical extinction law. *ApJ*, 429: 582–601, July 1994. doi: 10.1086/174346. (Cited on pages 16 and 28.)

A. Chelli, I. Cruz-Gonzalez, and B. Reipurth. Near infrared observations of southern young multiple systems. *A&AS*, 114:135, November 1995. (Cited on page 60.)

R. Chini, K. Kämpgen, B. Reipurth, M. Albrecht, E. Kreysa, R. Lemke, M. Nielbock, L. A. Reichertz, A. Sievers, and R. Zylka. SIMBA observations of the R Corona Australis molecular cloud. *A&A*, 409:235–244, October 2003a. doi: 10.1051/0004-6361:20031115. (Cited on page 67.)

R. Chini, K. Kämpgen, B. Reipurth, M. Albrecht, E. Kreysa, R. Lemke, M. Nielbock, L. A. Reichertz, A. Sievers, and R. Zylka. SIMBA observations of the R Corona Australis molecular cloud. *A&A*, 409:235–244, October 2003b. doi: 10.1051/0004-6361:20031115. (Cited on page 72.)

J. E. Dale, B. Ercolano, and I. A. Bonnell. Ionizing feedback from massive stars in massive clusters - II. Disruption of bound clusters by photoionization. *MNRAS*, 424:377–392, July 2012. doi: 10.1111/j.1365-2966.2012.21205.x. (Cited on pages 19, 53, and 56.)

J. E. Dale, B. Ercolano, and I. A. Bonnell. Ionizing feedback from massive stars in massive clusters - III. Disruption of partially unbound clouds. *MNRAS*, 430:234–246, March 2013. doi: 10.1093/mnras/sts592. (Cited on pages 53 and 56.)

F. D'Antona and I. Mazzitelli. Evolution of low mass stars. *Mem. Soc. Astron. Italiana*, 68:807, 1997. (Cited on page 76.)

R. E. Davies and J. E. Pringle. On accretion from an inhomogeneous medium. *MNRAS*, 191:599–604, May 1980. (Cited on page 52.)

I. de Looze, M. Baes, J. Fritz, and J. Verstappen. Panchromatic radiative transfer modelling of stars and dust in the Sombrero galaxy. *MNRAS*, 419:895–903, January 2012. doi: 10.1111/j.1365-2966.2011.19759.x. (Cited on page 11.)

G. De Marchi, N. Panagia, M. Romaniello, E. Sabbi, M. Sirianni, P. G. Prada Moroni, and S. Degl'Innocenti. Photometric Determination of the Mass Accretion Rates of Pre-main-sequence Stars. II. NGC 346 in the Small Magellanic Cloud. *ApJ*, 740:11, October 2011a. doi: 10.1088/0004-637X/740/1/11. (Cited on page 52.)

G. De Marchi, N. Panagia, and E. Sabbi. Clues to the Star Formation in NGC 346 across Time and Space. *ApJ*, 740:10, October 2011b. doi: 10.1088/0004-637X/740/1/10. (Cited on page 52.)

G. De Marchi, F. Paresce, N. Panagia, G. Beccari, L. Spezzi, M. Sirianni, M. Andersen, M. Mutchler, B. Balick, M. A. Dopita, J. A. Frogel, B. C. Whitmore, H. Bond, D. Calzetti, C. M. Carollo, M. J. Disney, D. N. B. Hall, J. A. Holtzman, R. A. Kimble, P. J. McCarthy, R. W. O'Connell, A. Saha, J. I. Silk, J. T. Trauger, A. R. Walker, R. A. Windhorst, and E. T. Young. Star Formation in 30 Doradus. *ApJ*, 739:27, September 2011c. doi: 10.1088/0004-637X/739/1/27. (Cited on page 52.)

G. De Marchi, G. Beccari, and N. Panagia. Photometric Determination of the Mass Accretion Rates of Pre-main-sequence Stars. IV. Recent Star Formation in NGC 602. *ApJ*, 775:68, September 2013a. doi: 10.1088/0004-637X/775/1/68. (Cited on page 51.)

G. De Marchi, N. Panagia, M. G. Guarcello, and R. Bonito. Pre-main-sequence stars older than 8 Myr in the Eagle nebula. *MNRAS*, 435:3058–3070, November 2013b. doi: 10.1093/mnras/stt1499. (Cited on pages 52 and 54.)

H. DeVoe. Optical Properties of Molecular Aggregates. I. Classical Model of Electronic Absorption and Refraction. *J. Chem. Phys.*, 41:393–400, July 1964. doi: 10.1063/1.1725879. (Cited on page 9.)

K. Dohlen, M. Langlois, M. Saisse, L. Hill, A. Origne, M. Jacquet, C. Fabron, J.-C. Blanc, M. Llored, M. Carle, C. Moutou, A. Vigan, A. Boccaletti, M. Carbillet, D. Mouillet, and J.-L. Beuzit. The infra-red dual imaging and spectrograph for SPHERE: design and performance. In *Society of Photo-Optical Instrumentation Engineers (SPIE) Conference Series*, volume 7014 of *Society of Photo-Optical Instrumentation Engineers (SPIE) Conference Series*, page 3, July 2008. doi: 10.1117/12.789786. (Cited on page 87.)

B. T. Draine. Interstellar Dust Grains. *ARA&A*, 41:241–289, 2003a. doi: 10.1146/annurev.astro.41.011802.094840. (Cited on pages 15 and 29.)

B. T. Draine. Scattering by Interstellar Dust Grains. I. Optical and Ultraviolet. *ApJ*, 598:1017–1025, December 2003b. doi: 10.1086/379118. (Cited on page 34.)

G. Duchêne and A. Kraus. Stellar Multiplicity. *ARA&A*, 51:269–310, August 2013. doi: 10.1146/annurev-astro-081710-102602. (Cited on pages 59 and 60.)

C. P. Dullemond and C. Dominik. The effect of dust settling on the appearance of protoplanetary disks. *A&A*, 421:1075–1086, July 2004. doi: 10.1051/0004-6361:20040284. (Cited on page 69.)

C. P. Dullemond, D. Hollenbach, I. Kamp, and P. D'Alessio. Models of the Structure and Evolution of Protoplanetary Disks. *Protostars and Planets V*, pages 555–572, 2007. (Cited on pages 19, 51, and 69.)

R. Edgar and C. Clarke. The effect of radiative feedback on Bondi-Hoyle flow around a massive star. *MNRAS*, 349:678–686, April 2004. doi: 10.1111/j.1365-2966.2004.07533.x. (Cited on page 54.)

S. Ekström, C. Georgy, P. Eggenberger, G. Meynet, N. Mowlavi, A. Wyttenbach, A. Granada, T. Decressin, R. Hirschi, U. Frischknecht, C. Charbonnel, and A. Maeder. Grids of stellar models with rotation. I. Models from 0.8 to 120 $M_\odot$ at solar metallicity (Z = 0.014). *A&A*, 537:A146, January 2012. doi: 10.1051/0004-6361/201117751. (Cited on pages 22 and 23.)

B. Ercolano, M. J. Barlow, P. J. Storey, and X.-W. Liu. MOCASSIN: a fully three-dimensional Monte Carlo photoionization code. *MNRAS*, 340:1136–1152, April 2003. doi: 10.1046/j.1365-8711.2003.06371.x. (Cited on page 11.)

C. Espaillat, J. Muzerolle, J. Najita, S. Andrews, Z. Zhu, N. Calvet, S. Kraus, J. Hashimoto, A. Kraus, and P. D'Alessio. An Observational Perspective of Transitional Disks. *Protostars and Planets VI*, pages 497–520, 2014. doi: 10.2458/azu_uapress_9780816531240-ch022. (Cited on page 20.)

G. G. Fazio, J. L. Hora, L. E. Allen, M. L. N. Ashby, P. Barmby, L. K. Deutsch, J.-S. Huang, S. Kleiner, M. Marengo, S. T. Megeath, G. J. Melnick, M. A. Pahre, B. M. Patten, J. Polizotti, H. A. Smith, R. S. Taylor, Z. Wang, S. P. Willner, W. F. Hoffmann, J. L. Pipher, W. J. Forrest, C. W. McMurty, C. R. McCreight, M. E. McKelvey, R. E. McMurray, D. G. Koch, S. H. Moseley, R. G. Arendt, J. E. Mentzell, C. T. Marx, P. Losch, P. Mayman, W. Eichhorn, D. Krebs, M. Jhabvala, D. Y. Gezari, D. J. Fixsen, J. Flores, K. Shakoorzadeh, R. Jungo, C. Hakun, L. Workman, G. Karpati, R. Kichak, R. Whitley, S. Mann, E. V. Tollestrup, P. Eisenhardt, D. Stern, V. Gorjian, B. Bhattacharya, S. Carey, B. O. Nelson, W. J. Glaccum, M. Lacy, P. J. Lowrance, S. Laine, W. T. Reach, J. A. Stauffer, J. A. Surace, G. Wilson, E. L. Wright, A. Hoffman, G. Domingo, and M. Cohen. The Infrared Array Camera (IRAC) for the Spitzer Space Telescope. *ApJS*, 154:10–17, September 2004. doi: 10.1086/422843. (Cited on page 44.)

D. Fedele, M. E. van den Ancker, T. Henning, R. Jayawardhana, and J. M. Oliveira. Timescale of mass accretion in pre-main-sequence stars. *A&A*, 510:A72, February 2010. doi: 10.1051/0004-6361/200912810. (Cited on pages 21 and 51.)

J. Fischera. On the thermal behaviour of small iron grains. *A&A*, 428:99–108, December 2004. doi: 10.1051/0004-6361:20034137. (Cited on page 85.)

J. Fischera and M. Dopita. Attenuation Caused by a Distant Isothermal Turbulent Screen. *ApJ*, 619:340–356, January 2005. doi: 10.1086/426185. (Cited on pages 31 and 45.)

J. Fischera and M. Dopita. On the missing 2175 Å-bump in the Calzetti extinction curve. *A&A*, 533:A117, September 2011. doi: 10.1051/0004-6361/201116644. (Cited on page 45.)

E. L. Fitzpatrick and D. Massa. An analysis of the shapes of ultraviolet extinction curves. III - an atlas of ultraviolet extinction curves. *ApJS*, 72:163–189, January 1990. doi: 10.1086/191413. (Cited on page 27.)

E. L. Fitzpatrick and D. Massa. An Analysis of the Shapes of Interstellar Extinction Curves. V. The IR-through-UV Curve Morphology. *ApJ*, 663:320–341, July 2007. doi: 10.1086/518158. (Cited on pages xiii, xv, 16, 17, 27, and 48.)

E. Furlan, L. Hartmann, N. Calvet, P. D'Alessio, R. Franco-Hernández, W. J. Forrest, D. M. Watson, K. I. Uchida, B. Sargent, J. D. Green, L. D. Keller, and T. L. Herter. A Survey and Analysis of Spitzer Infrared Spectrograph Spectra of T Tauri Stars in Taurus. *ApJS*, 165:568–605, August 2006. doi: 10.1086/505468. (Cited on page 76.)

E. Furlan, D. M. Watson, M. K. McClure, P. Manoj, C. Espaillat, P. D'Alessio, N. Calvet, K. H. Kim, B. A. Sargent, W. J. Forrest, and L. Hartmann. Disk Evolution in the Three Nearby Star-forming Regions of Taurus, Chamaeleon, and Ophiuchus. *ApJ*, 703:1964–1983, October 2009. doi: 10.1088/0004-637X/703/2/1964. (Cited on page 76.)

T. Fusco, G. Rousset, J.-F. Sauvage, C. Petit, J.-L. Beuzit, K. Dohlen, D. Mouillet, J. Charton, M. Nicolle, M. Kasper, P. Baudoz, and P. Puget. High-order adaptive optics requirements for direct detection of extrasolar planets: Application to the SPHERE instrument. *Optics Express*, 14:7515, 2006. doi: 10.1364/OE.14.007515. (Cited on page 87.)

H.-P. Gail and E. Sedlmayr. *Physics and Chemistry of Circumstellar Dust Shells*. December 2013. (Cited on page 85.)

C. Gall, J. Hjorth, and A.C. Andersen. Production of dust by massive stars at high redshift. *The Astronomy and Astrophysics Review*, 19(1):43, 2011. ISSN 0935-4956. doi: 10.1007/s00159-011-0043-7. URL http://dx.doi.org/10.1007/s00159-011-0043-7. (Cited on pages 23 and 96.)

C. Gall, J. Hjorth, D. Watson, E. Dwek, J. R. Maund, O. Fox, G. Leloudas, D. Malesani, and A. C. Day-Jones. Rapid formation of large dust grains in the luminous supernova 2010jl. *Nature*, 511:326–329, July 2014. doi: 10.1038/nature13558. (Cited on pages 25 and 96.)

R. Gehrz. Sources of Stardust in the Galaxy. In L. J. Allamandola and A. G. G. M. Tielens, editors, *Interstellar Dust*, volume 135 of *IAU Symposium*, page 445, 1989. (Cited on page 23.)

C. Georgy, S. Ekström, G. Meynet, P. Massey, E. M. Levesque, R. Hirschi, P. Eggenberger, and A. Maeder. Grids of stellar models with rotation. II. WR populations and supernovae/GRB progenitors at Z = 0.014. *A&A*, 542:A29, June 2012. doi: 10.1051/0004-6361/201118340. (Cited on page 83.)

K. D. Gordon, K. A. Misselt, A. N. Witt, and G. C. Clayton. The DIRTY Model. I. Monte Carlo Radiative Transfer through Dust. *ApJ*, 551:269–276, April 2001. doi: 10.1086/320082. (Cited on page 15.)

E. Gullbring, L. Hartmann, C. Briceño, and N. Calvet. Disk Accretion Rates for T Tauri Stars. *ApJ*, 492:323–341, January 1998. doi: 10.1086/305032. (Cited on page 76.)

B. Gustafsson, B. Edvardsson, K. Eriksson, U. G. Jørgensen, Å. Nordlund, and B. Plez. A grid of MARCS model atmospheres for late-type stars. I. Methods and general

properties. *A&A*, 486:951–970, August 2008. doi: 10.1051/0004-6361:200809724. (Cited on page 84.)

T. J. Harries. Radiation-hydrodynamical simulations of massive star formation using Monte Carlo radiative transfer - I. Algorithms and numerical methods. *MNRAS*, 448:3156–3166, April 2015. doi: 10.1093/mnras/stv158. (Cited on page 11.)

L. Hartmann. *Accretion Processes in Star Formation: Second Edition*. Cambridge University Press, 2009. (Cited on pages 20 and 51.)

M. Harwit, K. Malfait, L. Decin, C. Waelkens, H. Feuchtgruber, and G. J. Melnick. The Infrared Continuum Spectrum of VY Canis Majoris. *ApJ*, 557:844–853, August 2001. doi: 10.1086/321684. (Cited on pages 86 and 96.)

T. Henning, R. Launhardt, J. Steinacker, and E. Thamm. Cold dust around southern Herbig Ae/Be stars. *A&A*, 291:546–556, November 1994. (Cited on page 72.)

L. G. Henyey and J. L. Greenstein. Diffuse radiation in the Galaxy. *ApJ*, 93:70–83, January 1941. doi: 10.1086/144246. (Cited on pages 12 and 31.)

G. H. Herbig. VY Canis Majoris. IV. The emission bands of ScO. *ApJ*, 188:533–538, March 1974. doi: 10.1086/152744. (Cited on page 84.)

G. J. Herczeg and L. A. Hillenbrand. An Optical Spectroscopic Study of T Tauri Stars. I. Photospheric Properties. *ApJ*, 786:97, May 2014. doi: 10.1088/0004-637X/786/2/97. (Cited on page 60.)

J. Hernández, L. Hartmann, T. Megeath, R. Gutermuth, J. Muzerolle, N. Calvet, A. K. Vivas, C. Briceño, L. Allen, J. Stauffer, E. Young, and G. Fazio. A Spitzer Space Telescope Study of Disks in the Young σ Orionis Cluster. *ApJ*, 662:1067–1081, June 2007. doi: 10.1086/513735. (Cited on page 51.)

F. Heymann and R. Siebenmorgen. GPU-based Monte Carlo Dust Radiative Transfer Scheme Applied to Active Galactic Nuclei. *ApJ*, 751:27, May 2012. doi: 10.1088/0004-637X/751/1/27. (Cited on pages 11, 31, 35, and 85.)

A. M. Hofmeister, K. M. Pitman, A. F. Goncharov, and A. K. Speck. Optical Constants of Silicon Carbide for Astrophysical Applications. II. Extending Optical Functions from Infrared to Ultraviolet Using Single-Crystal Absorption Spectra. *ApJ*, 696:1502–1516, May 2009. doi: 10.1088/0004-637X/696/2/1502. (Cited on page 43.)

S. Höfner. Winds of M-type AGB stars driven by micron-sized grains. *A&A*, 491:L1–L4, November 2008. doi: 10.1051/0004-6361:200810641. (Cited on pages 83 and 94.)

D. W. Hogg, J. Bovy, and D. Lang. Data analysis recipes: Fitting a model to data. *ArXiv e-prints*, August 2010. (Cited on page 61.)

S. Hony, A. G. G. M. Tielens, L. B. F. M. Waters, and A. de Koter. The circumstellar envelope of the C-rich post-AGB star HD 56126. *A&A*, 402:211–228, April 2003. doi: 10.1051/0004-6361:20030240. (Cited on pages xiii, 23, and 24.)

I. D. Howarth. LMC and galactic extinction. *MNRAS*, 203:301–304, April 1983. (Cited on pages 16 and 27.)

F. Hoyle and R. A. Lyttleton. The effect of interstellar matter on climatic variation. *Proceedings of the Cambridge Philosophical Society*, 35:405, 1939. doi: 10.1017/S0305004100021150. (Cited on page 52.)

R. M. Humphreys, L. A. Helton, and T. J. Jones. The Three-Dimensional Morphology of VY Canis Majoris. I. The Kinematics of the Ejecta. *AJ*, 133:2716–2729, June 2007. doi: 10.1086/517609. (Cited on pages 83, 84, 86, 93, 94, and 95.)

R. Indebetouw, B. A. Whitney, K. E. Johnson, and K. Wood. Three-dimensional Models of Embedded High-Mass Stars: Effects of a Clumpy Circumstellar Medium. *ApJ*, 636:362–380, January 2006. doi: 10.1086/497886. (Cited on pages 11 and 28.)

R. Indebetouw, C. Brogan, C.-H. R. Chen, A. Leroy, K. Johnson, E. Muller, S. Madden, D. Cormier, F. Galliano, A. Hughes, T. Hunter, A. Kawamura, A. Kepley, V. Lebouteiller, M. Meixner, J. M. Oliveira, T. Onishi, and T. Vasyunina. ALMA Resolves 30 Doradus: Sub-parsec Molecular Cloud Structure near the Closest Super Star Cluster. *ApJ*, 774:73, September 2013. doi: 10.1088/0004-637X/774/1/73. (Cited on page 56.)

A Isella. *Interferometric observations of pre-main sequence disks*. PhD thesis, Università degli Studi di Milano, 2006. (Cited on pages xiii and 20.)

W. G. Joint Iras Science. IRAS catalogue of Point Sources, Version 2.0 (IPAC 1986). *VizieR Online Data Catalog*, 2125:0, January 1994. (Cited on page 84.)

T. J. Jones, R. M. Humphreys, L. A. Helton, C. Gui, and X. Huang. The Three-Dimensional Morphology of VY Canis Majoris. II. Polarimetry and the Line-of-Sight Distribution of the Ejecta. *AJ*, 133:2730–2736, June 2007. doi: 10.1086/517610. (Cited on pages 83, 84, 90, 93, and 94.)

H.-U. Kaeufl, P. Ballester, P. Biereichel, B. Delabre, R. Donaldson, R. Dorn, E. Fedrigo, G. Finger, G. Fischer, F. Franza, D. Gojak, G. Huster, Y. Jung, J.-L. Lizon, L. Mehrgan, M. Meyer, A. Moorwood, J.-F. Pirard, J. Paufique, E. Pozna, R. Siebenmorgen, A. Silber, J. Stegmeier, and S. Wegerer. CRIRES: a high-resolution infrared spectrograph for ESO's VLT. In A. F. M. Moorwood and M. Iye, editors, *Ground-based Instrumentation for Astronomy*, volume 5492 of *Society of Photo-Optical Instrumentation Engineers (SPIE) Conference Series*, pages 1218–1227, September 2004. doi: 10.1117/12.551480. (Cited on page 63.)

J. H. Kastner and D. A. Weintraub. Hubble Space Telescope Imaging of the Mass-losing Supergiant VY Canis Majoris. *AJ*, 115:1592–1598, April 1998. doi: 10.1086/300297. (Cited on page 84.)

F. Kemper, F. J. Molster, C. Jäger, and L. B. F. M. Waters. The mineral composition and spatial distribution of the dust ejecta of NGC 6302. *A&A*, 394:679–690, November 2002. doi: 10.1051/0004-6361:20021119. (Cited on pages xiii and 24.)

F. Kerschbaum, D. Ladjal, R. Ottensamer, M. A. T. Groenewegen, M. Mecina, J. A. D. L. Blommaert, B. Baumann, L. Decin, B. Vandenbussche, C. Waelkens, T. Posch,

E. Huygen, W. De Meester, S. Regibo, P. Royer, K. Exter, and C. Jean. The detached dust shells of AQ Andromedae, U Antliae, and TT Cygni. *A&A*, 518:L140, July 2010. doi: 10.1051/0004-6361/201014633. (Cited on page 22.)

J. Kessler-Silacci, J.-C. Augereau, C. P. Dullemond, V. Geers, F. Lahuis, N. J. Evans, II, E. F. van Dishoeck, G. A. Blake, A. C. A. Boogert, J. Brown, J. K. Jørgensen, C. Knez, and K. M. Pontoppidan. c2d Spitzer IRS Spectra of Disks around T Tauri Stars. I. Silicate Emission and Grain Growth. *ApJ*, 639:275–291, March 2006. doi: 10.1086/499330. (Cited on page 76.)

C. D. Koresko, T. M. Herbst, and C. Leinert. The Infrared Companions of T Tauri Stars. *ApJ*, 480:741–753, May 1997. (Cited on page 76.)

A. L. Kraus and L. A. Hillenbrand. The Coevality of Young Binary Systems. *ApJ*, 704:531–547, October 2009. doi: 10.1088/0004-637X/704/1/531. (Cited on pages 59 and 60.)

E. Krügel. *An introduction to the physics of interstellar dust*. 2008. (Cited on pages 5, 9, 11, and 31.)

E. Krügel. The influence of scattering on the extinction of stars. *A&A*, 493:385–397, January 2009. doi: 10.1051/0004-6361:200809976. (Cited on pages 16, 28, 30, 31, 37, and 41.)

A. J. Kruger, M. J. Richter, J. S. Carr, J. R. Najita, G. W. Doppmann, and A. Seifahrt. Gas and Dust Toward DG Tau B and VV CrA. *ApJ*, 729:145, March 2011. doi: 10.1088/0004-637X/729/2/145. (Cited on pages 60, 71, and 72.)

C. J. Lada and B. A. Wilking. The nature of the embedded population in the Rho Ophiuchi dark cloud - Mid-infrared observations. *ApJ*, 287:610–621, December 1984. doi: 10.1086/162719. (Cited on page 19.)

M. Langlois, K. Dohlen, A. Vigan, A. Zurlo, C. Moutou, H. M. Schmid, J. Mili, J.-L. Beuzit, A. Boccaletti, M. Carle, A. Costille, R. Dorn, L. Gluck, N. Hubin, M. Feldt, M. Kasper, L. Lizon, F. Madec, D. Le Mignant, D. Mouillet, J.-P. Puget, J.-F. Sauvage, and F. Wildi. High contrast polarimetry in the infrared with SPHERE on the VLT. In *Society of Photo-Optical Instrumentation Engineers (SPIE) Conference Series*, volume 9147 of *Society of Photo-Optical Instrumentation Engineers (SPIE) Conference Series*, page 1, July 2014. doi: 10.1117/12.2055549. (Cited on page 87.)

J. Larsson, C. Fransson, G. Östlin, P. Gröningsson, A. Jerkstrand, C. Kozma, J. Sollerman, P. Challis, R. P. Kirshner, R. A. Chevalier, K. Heng, R. McCray, N. B. Suntzeff, P. Bouchet, A. Crotts, J. Danziger, E. Dwek, K. France, P. M. Garnavich, S. S. Lawrence, B. Leibundgut, P. Lundqvist, N. Panagia, C. S. J. Pun, N. Smith, G. Sonneborn, L. Wang, and J. C. Wheeler. X-ray illumination of the ejecta of supernova 1987A. *Nature*, 474:484–486, June 2011. doi: 10.1038/nature10090. (Cited on page 96.)

A. T. Lee, A. J. Cunningham, C. F. McKee, and R. I. Klein. Bondi-Hoyle Accretion in an Isothermal Magnetized Plasma. *ApJ*, 783:50, March 2014. doi: 10.1088/0004-637X/783/1/50. (Cited on page 54.)

C. Leinert, U. Graser, F. Przygodda, L. B. F. M. Waters, G. Perrin, W. Jaffe, B. Lopez, E. J. Bakker, A. Böhm, O. Chesneau, W. D. Cotton, S. Damstra, J. de Jong, A. W. Glazenborg-Kluttig, B. Grimm, H. Hanenburg, W. Laun, R. Lenzen, S. Ligori, R. J. Mathar, J. Meisner, S. Morel, W. Morr, U. Neumann, J.-W. Pel, P. Schuller, R.-R. Rohloff, B. Stecklum, C. Storz, O. von der Lühe, and K. Wagner. MIDI - the 10 \mum instrument on the VLTI. *Ap&SS*, 286:73–83, 2003a. doi: 10.1023/A:1026158127732. (Cited on page 62.)

C. Leinert, U. Graser, L. B. F. M. Waters, G. S. Perrin, W. Jaffe, B. Lopez, F. Przygodda, O. Chesneau, P. A. Schuller, A. W. Glazenborg-Kluttig, W. Laun, S. Ligori, J. A. Meisner, K. Wagner, E. J. Bakker, B. Cotton, J. de Jong, R. Mathar, U. Neumann, and C. Storz. Ten-micron instrument MIDI: getting ready for observations on the VLTI. In W. A. Traub, editor, *Interferometry for Optical Astronomy II*, volume 4838 of *Society of Photo-Optical Instrumentation Engineers (SPIE) Conference Series*, pages 893–904, February 2003b. (Cited on page 62.)

G. Lodato and W. K. M. Rice. Testing the locality of transport in self-gravitating accretion discs. *MNRAS*, 351:630–642, June 2004. doi: 10.1111/j.1365-2966.2004.07811.x. (Cited on page 71.)

G. Lodato and W. K. M. Rice. Testing the locality of transport in self-gravitating accretion discs - II. The massive disc case. *MNRAS*, 358:1489–1500, April 2005. doi: 10.1111/j.1365-2966.2005.08875.x. (Cited on page 71.)

D. J. P. Lommen, E. F. van Dishoeck, C. M. Wright, S. T. Maddison, M. Min, D. J. Wilner, D. M. Salter, H. J. van Langevelde, T. L. Bourke, R. F. J. van der Burg, and G. A. Blake. Grain growth across protoplanetary discs: 10 μm silicate feature versus millimetre slope. *A&A*, 515:A77, June 2010. doi: 10.1051/0004-6361/200913150. (Cited on pages 60, 67, 69, and 71.)

L. B. Lucy. Computing radiative equilibria with Monte Carlo techniques. *A&A*, 344:282–288, April 1999. (Cited on pages 12 and 31.)

D. Lynden-Bell and J. E. Pringle. The evolution of viscous discs and the origin of the nebular variables. *MNRAS*, 168:603–637, September 1974. (Cited on page 54.)

J. Lyu, L. Hao, and A. Li. Dust in Active Galactic Nuclei: Anomalous Silicate to Optical Extinction Ratios? *ApJ*, 792:L9, September 2014. doi: 10.1088/2041-8205/792/1/L9. (Cited on pages 16 and 44.)

R. Maiolino, A. Marconi, M. Salvati, G. Risaliti, P. Severgnini, E. Oliva, F. La Franca, and L. Vanzi. Dust in active nuclei. I. Evidence for "anomalous" properties. *A&A*, 365:28–36, January 2001. doi: 10.1051/0004-6361:20000177. (Cited on pages 16, 44, and 47.)

C. F. Manara, G. Beccari, N. Da Rio, G. De Marchi, A. Natta, L. Ricci, M. Robberto, and L. Testi. Accurate determination of accretion and photospheric parameters in young stellar objects: The case of two candidate old disks in the Orion Nebula Cluster. *A&A*, 558:A114, October 2013. doi: 10.1051/0004-6361/201321866. (Cited on pages 52 and 80.)

H. G. Marraco and A. E. Rydgren. On the distance and membership of the R CrA T association. *AJ*, 86:62–68, January 1981. doi: 10.1086/112856. (Cited on pages 67 and 72.)

P. Massey, E. M. Levesque, and B. Plez. Bringing VY Canis Majoris Down to Size: An Improved Determination of Its Effective Temperature. *ApJ*, 646:1203–1208, August 2006. doi: 10.1086/505025. (Cited on page 95.)

J. S. Mathis. Internal Dust in Nebulae. III. Nonisotropic Scattering. *ApJ*, 176:651, September 1972. doi: 10.1086/151667. (Cited on page 28.)

J. S. Mathis. Interstellar dust and extinction. *ARA&A*, 28:37–70, 1990. doi: 10.1146/annurev.aa.28.090190.000345. (Cited on page 18.)

J. S. Mathis, W. Rumpl, and K. H. Nordsieck. The size distribution of interstellar grains. *ApJ*, 217:425–433, October 1977. doi: 10.1086/155591. (Cited on pages 15, 34, and 69.)

M. Matsuura, M. J. Barlow, A. A. Zijlstra, P. A. Whitelock, M.-R. L. Cioni, M. A. T. Groenewegen, K. Volk, F. Kemper, T. Kodama, E. Lagadec, M. Meixner, G. C. Sloan, and S. Srinivasan. The global gas and dust budget of the Large Magellanic Cloud: AGB stars and supernovae, and the impact on the ISM evolution. *MNRAS*, 396: 918–934, June 2009. doi: 10.1111/j.1365-2966.2009.14743.x. (Cited on page 23.)

M. K. McClure, E. Furlan, P. Manoj, K. L. Luhman, D. M. Watson, W. J. Forrest, C. Espaillat, N. Calvet, P. D'Alessio, B. Sargent, J. J. Tobin, and H.-F. Chiang. The Evolutionary State of the Pre-main Sequence Population in Ophiuchus: A Large Infrared Spectrograph Survey. *ApJS*, 188:75–122, May 2010. doi: 10.1088/0067-0049/188/1/75. (Cited on page 76.)

G. Mie. Beiträge zur Optik trüber Medien, speziell kolloidaler Metallösungen. *Ann. Phys.*, 330:377–445, 1908. doi: 10.1002/andp.19083300302. (Cited on pages 9, 12, 31, and 92.)

N. Moeckel and H. B. Throop. Bondi-Hoyle-Lyttleton Accretion Onto a Protoplanetary Disk. *ApJ*, 707:268–277, December 2009. doi: 10.1088/0004-637X/707/1/268. (Cited on page 52.)

S. Mohanty, J. Greaves, D. Mortlock, I. Pascucci, A. Scholz, M. Thompson, D. Apai, G. Lodato, and D. Looper. Protoplanetary Disk Masses from Stars to Brown Dwarfs. *ApJ*, 773:168, August 2013. doi: 10.1088/0004-637X/773/2/168. (Cited on page 71.)

S. Morel, P. Ballester, B. Bauvir, P. Biereichel, J.-G. Cuby, E. Galliano, N. Haddad, N. Housen, C. A. Hummel, A. Kaufer, P. Kervella, I. Percheron, F. Puech, F. T. Rantakyro, A. Richichi, C. Sabet, M. Schoeller, J. Spyromilio, M. Vannier, A. Wallander, M. Wittkowski, C. Leinert, U. Graser, U. Neumann, W. J. Jaffe, and J. A. de Jong. Preparing MIDI science operation at VLTI. In W. A. Traub, editor, *New Frontiers in Stellar Interferometry*, volume 5491 of *Society of Photo-Optical Instrumentation Engineers (SPIE) Conference Series*, page 1666, October 2004. (Cited on page 62.)

T. Moriya, N. Tominaga, S. I. Blinnikov, P. V. Baklanov, and E. I. Sorokina. Supernovae from red supergiants with extensive mass loss. *MNRAS*, 415:199–213, July 2011. doi: 10.1111/j.1365-2966.2011.18689.x. (Cited on page 83.)

S. Muller, Dinh-V-Trung, J. Lim, N. Hirano, C. Muthu, and S. Kwok. The Molecular Envelope around the Red Supergiant VY CMa. *ApJ*, 656:1109–1120, February 2007. doi: 10.1086/510513. (Cited on pages 83, 84, 86, 93, 94, and 96.)

A. Natta and N. Panagia. Extinction in inhomogeneous clouds. *ApJ*, 287:228–237, December 1984. doi: 10.1086/162681. (Cited on pages 28, 37, 41, and 46.)

R. Neuhäuser, F. M. Walter, E. Covino, J. M. Alcalá, S. J. Wolk, S. Frink, P. Guillout, M. F. Sterzik, and F. Comerón. Search for young stars among ROSAT All-Sky Survey X-ray sources in and around the R CrA dark cloud. *A&AS*, 146:323–347, October 2000. doi: 10.1051/aas:2000272. (Cited on page 60.)

B. R. M. Norris, P. G. Tuthill, M. J. Ireland, S. Lacour, A. A. Zijlstra, F. Lykou, T. M. Evans, P. Stewart, and T. R. Bedding. A close halo of large transparent grains around extreme red giant stars. *Nature*, 484:220–222, April 2012. doi: 10.1038/nature10935. (Cited on pages 83 and 94.)

D. J. Nutter, D. Ward-Thompson, and P. André. The pre-stellar and protostellar population of R Coronae Australis. *MNRAS*, 357:975–982, March 2005. doi: 10.1111/j.1365-2966.2005.08711.x. (Cited on page 72.)

E. O'Gorman, W. Vlemmings, A. M. S. Richards, A. Baudry, E. De Beck, L. Decin, G. M. Harper, E. M. Humphreys, P. Kervella, T. Khouri, and S. Muller. ALMA observations of anisotropic dust mass loss in the inner circumstellar environment of the red supergiant VY Canis Majoris. *A&A*, 573:L1, January 2015. doi: 10.1051/0004-6361/201425101. (Cited on pages 83, 84, 94, and 95.)

I. Oliveira, K. M. Pontoppidan, B. Merín, E. F. van Dishoeck, F. Lahuis, V. C. Geers, J. K. Jørgensen, J. Olofsson, J.-C. Augereau, and J. M. Brown. A Spitzer Survey of Protoplanetary Disk Dust in the Young Serpens Cloud: How do Dust Characteristics Evolve with Time? *ApJ*, 714:778–798, May 2010. doi: 10.1088/0004-637X/714/1/778. (Cited on page 76.)

S. Olofsson and G. Olofsson. The mid-infrared extinction in molecular clouds. Case study of B 335. *A&A*, 534:A127, October 2011. doi: 10.1051/0004-6361/201015564. (Cited on page 19.)

V. Ossenkopf, T. Henning, and J. S. Mathis. Constraints on cosmic silicates. *A&A*, 261:567–578, August 1992. (Cited on pages 85 and 92.)

P. Padoan, B. J. T. Jones, and A. P. Nordlund. Supersonic Turbulence in the Interstellar Medium: Stellar Extinction Determinations as Probes of the Structure and Dynamics of Dark Clouds. *ApJ*, 474:730, January 1997. doi: 10.1086/303482. (Cited on pages 19 and 44.)

P. Padoan, A. Kritsuk, M. L. Norman, and Å. Nordlund. A Solution to the Pre-Main-Sequence Accretion Problem. *ApJ*, 622:L61–L64, March 2005. doi: 10.1086/429562. (Cited on page 52.)

R. J. Panek. Ultraviolet flux distributions of stars in the Orion Nebula cluster. *ApJ*, 270:169–179, July 1983. doi: 10.1086/161108. (Cited on page 46.)

T. Passot and E. Vázquez-Semadeni. Density probability distribution in one-dimensional polytropic gas dynamics. *Phys. Rev. E*, 58:4501–4510, October 1998. doi: 10.1103/PhysRevE.58.4501. (Cited on page 44.)

L. Prato and M. Simon. Are Both Stars in a Classic T Tauri Binary Classic T Tauri Stars? *ApJ*, 474:455–463, January 1997. (Cited on page 76.)

L. Prato, T. P. Greene, and M. Simon. Astrophysics of Young Star Binaries. *ApJ*, 584: 853–874, February 2003. doi: 10.1086/345828. (Cited on page 60.)

M. L. Prevot, J. Lequeux, L. Prevot, E. Maurice, and B. Rocca-Volmerange. The typical interstellar extinction in the Small Magellanic Cloud. *A&A*, 132:389–392, March 1984. (Cited on pages 16 and 27.)

F. Przygodda. *Spektroskopische und interferometrische Untersuchungen an T Tauri-Sternen im mittleren Infrarotbereich*. PhD thesis, Max-Planck Institute of Astronomy, Heidelberg, 2004. (Cited on pages 60 and 63.)

M. Rahman, C. D. Matzner, and D.-S. Moon. OB Associations at the Upper End of the Milky Way Luminosity Function. *ApJ*, 766:135, April 2013. doi: 10.1088/0004-637X/766/2/135. (Cited on page 57.)

T. Ratzka, C. Leinert, F. Przygodda, and S. Wolf. VV CrA - The Dusty Environment of an Infrared Companion. In A. Richichi, F. Delplancke, F. Paresce, and A. Chelli, editors, *The Power of Optical/IR Interferometry: Recent Scientific Results and 2nd Generation*, page 519, 2008. doi: 10.1007/978-3-540-74256-2_74. (Cited on page 72.)

B. Reipurth and H. Zinnecker. Visual binaries among pre-main sequence stars. *A&A*, 278:81–108, October 1993. (Cited on page 60.)

L. Ricci, L. Testi, A. Natta, and K. J. Brooks. Dust grain growth in ρ-Ophiuchi protoplanetary disks. *A&A*, 521:A66, October 2010. doi: 10.1051/0004-6361/201015039. (Cited on page 21.)

A. M. S. Richards, J. A. Yates, and R. J. Cohen. MERLIN observations of water maser proper motions in VY Canis Majoris. *MNRAS*, 299:319–331, September 1998. doi: 10.1046/j.1365-8711.1998.01386.x. (Cited on page 84.)

A. M. S. Richards, C. M. V. Impellizzeri, E. M. Humphreys, C. Vlahakis, W. Vlemmings, A. Baudry, E. De Beck, L. Decin, S. Etoka, M. D. Gray, G. M. Harper, T. R. Hunter, P. Kervella, F. Kerschbaum, I. McDonald, G. Melnick, S. Muller, D. Neufeld, E. O'Gorman, S. Y. Parfenov, A. B. Peck, H. Shinnaga, A. M. Sobolev, L. Testi, L. Uscanga, A. Wootten, J. A. Yates, and A. Zijlstra. ALMA sub-mm maser and dust distribution of VY Canis Majoris. *A&A*, 572:L9, December 2014. doi: 10.1051/0004-6361/201425024. (Cited on pages 83 and 94.)

J. Rodmann, T. Henning, C. J. Chandler, L. G. Mundy, and D. J. Wilner. Large dust particles in disks around T Tauri stars. *A&A*, 446:211–221, January 2006. doi: 10.1051/0004-6361:20054038. (Cited on page 21.)

C. Rola and D. Pelat. On the estimation of intensity for low S/N ratio narrow emission lines. *A&A*, 287:676–684, July 1994. (Cited on page 62.)

K. Rowlands, H. L. Gomez, L. Dunne, A. Aragón-Salamanca, S. Dye, S. Maddox, E. da Cunha, and P. van der Werf. The dust budget crisis in high-redshift submillimetre galaxies. *MNRAS*, 441:1040–1058, June 2014. doi: 10.1093/mnras/stu605. (Cited on page 25.)

M. Ruffert. Non-axisymmetric wind-accretion simulations. I. Velocity gradients of 3% and 20% over one accretion radius. *A&A*, 317:793–814, February 1997. (Cited on page 54.)

E. E. Salpeter. The Luminosity Function and Stellar Evolution. *ApJ*, 121:161, January 1955. doi: 10.1086/145971. (Cited on page 53.)

J. Sanchez-Bermudez, C. A. Hummel, P. Tuthill, A. Alberdi, R. Schödel, and S. Lacour. Unveiling the near-infrared structure of the massive-young stellar object NGC 3603 IRS 9A with sparse aperture masking and spectroastrometry. *ArXiv e-prints*, September 2014. (Cited on page 67.)

A. A. Schegerer, S. Wolf, T. Ratzka, and C. Leinert. The T Tauri star RY Tauri as a case study of the inner regions of circumstellar dust disks. *A&A*, 478:779–793, February 2008. doi: 10.1051/0004-6361:20077049. (Cited on page 76.)

K. Serkowski. Large Optical Polarization of the OH Emission Source VY Canis Majoris. *ApJ*, 156:L139, June 1969. doi: 10.1086/180366. (Cited on page 84.)

N. I. Shakura and R. A. Sunyaev. Black holes in binary systems. Observational appearance. *A&A*, 24:337–355, 1973a. (Cited on page 69.)

N. I. Shakura and R. A. Sunyaev. Black holes in binary systems. Observational appearance. *A&A*, 24:337–355, 1973b. (Cited on page 54.)

D. P. Shenoy, T. J. Jones, R. M. Humphreys, M. Marengo, J. M. Leisenring, M. J. Nelson, J. C. Wilson, M. F. Skrutskie, P. M. Hinz, W. F. Hoffmann, V. Bailey, A. Skemer, T. Rodigas, and V. Vaitheeswaran. Adaptive Optics Imaging of VY Canis Majoris at 2-5 μm with LBT/LMIRCam. *AJ*, 146:90, October 2013. doi: 10.1088/0004-6256/146/4/90. (Cited on pages 93 and 94.)

D. P. Shenoy, T. J. Jones, C. Packham, and E. Lopez-Rodriguez. Probing Hypergiant Mass Loss with Adaptive Optics Imaging & Polarimetry in the Infrared: MMT-Pol and LMIRCam observations of IRC +10420 & VY Canis Majoris. *ArXiv e-prints*, May 2015. (Cited on pages 93 and 94.)

F. H. Shu, F. C. Adams, and S. Lizano. Star formation in molecular clouds - Observation and theory. *ARA&A*, 25:23–81, 1987. doi: 10.1146/annurev.aa.25.090187.000323. (Cited on pages 19 and 51.)

A. Sicilia-Aguilar, T. Henning, J. Kainulainen, and V. Roccatagliata. Protostars and Stars in the Coronet Cluster: Age, Evolution, and Cluster Structure. *ApJ*, 736:137, August 2011. doi: 10.1088/0004-637X/736/2/137. (Cited on page 72.)

A. Sicilia-Aguilar, T. Henning, H. Linz, P. André, A. Stutz, C. Eiroa, and G. J. White. Protostars, multiplicity, and disk evolution in the Corona Australis region: a Herschel Gould Belt Study. *A&A*, 551:A34, March 2013a. doi: 10.1051/0004-6361/201220170. (Cited on page 60.)

A. Sicilia-Aguilar, T. Henning, H. Linz, P. André, A. Stutz, C. Eiroa, and G. J. White. Protostars, multiplicity, and disk evolution in the Corona Australis region: a Herschel Gould Belt Study. *A&A*, 551:A34, March 2013b. doi: 10.1051/0004-6361/201220170. (Cited on page 72.)

R. Siebenmorgen and F. Heymann. Shadows, gaps, and ring-like structures in protoplanetary disks. *A&A*, 539:A20, March 2012. doi: 10.1051/0004-6361/201118493. (Cited on page 31.)

R. Siebenmorgen, N. V. Voshchinnikov, and S. Bagnulo. Dust in the diffuse interstellar medium. Extinction, emission, linear and circular polarisation. *A&A*, 561:A82, January 2014. doi: 10.1051/0004-6361/201321716. (Cited on pages 15 and 29.)

R. Siebenmorgen, F. Heymann, and A. Efstathiou. Self-consistent dust radiative transfer models of AGN. *A&A*, subm. (Cited on page 44.)

N. Smith. Mass Loss: Its Effect on the Evolution and Fate of High-Mass Stars. *ARA&A*, 52:487–528, August 2014. doi: 10.1146/annurev-astro-081913-040025. (Cited on page 83.)

N. Smith, R. M. Humphreys, K. Davidson, R. D. Gehrz, M. T. Schuster, and J. Krautter. The Asymmetric Nebula Surrounding the Extreme Red Supergiant Vy Canis Majoris. *AJ*, 121:1111–1125, February 2001. doi: 10.1086/318748. (Cited on pages 86, 88, and 95.)

N. Smith, K. H. Hinkle, and N. Ryde. Red Supergiants as Potential Type IIn Supernova Progenitors: Spatially Resolved 4.6 μm CO Emission Around VY CMa and Betelgeuse. *AJ*, 137:3558–3573, March 2009a. doi: 10.1088/0004-6256/137/3/3558. (Cited on pages 83, 84, 86, 93, 94, 95, and 96.)

R. L. Smith, K. M. Pontoppidan, E. D. Young, M. R. Morris, and E. F. van Dishoeck. High-Precision $C^{17}O$, $C^{18}O$, and $C^{16}O$ Measurements in Young Stellar Objects: Analogues for Co Self-shielding in the Early Solar System. *ApJ*, 701:163–175, August 2009b. doi: 10.1088/0004-637X/701/1/163. (Cited on pages 60 and 80.)

H. Steenman and P. S. The. The anomalous extinction law. II - The effect of changing the lower size cutoff of the particle size distribution. *Ap&SS*, 184:9–30, October 1991. doi: 10.1007/BF00644862. (Cited on page 63.)

J. Steinacker, L. Pagani, A. Bacmann, and S. Guieu. Direct evidence of dust growth in L183 from mid-infrared light scattering. *A&A*, 511:A9, February 2010. doi: 10.1051/0004-6361/200912835. (Cited on page 43.)

M. Takami, J. Bailey, and A. Chrysostomou. A spectro-astrometric study of southern pre-main sequence stars. Binaries, outflows, and disc structure down to AU scales. *A&A*, 397:675–691, January 2003. doi: 10.1051/0004-6361:20021544. (Cited on page 60.)

L. Testi, T. Birnstiel, L. Ricci, S. Andrews, J. Blum, J. Carpenter, C. Dominik, A. Isella, A. Natta, J. P. Williams, and D. J. Wilner. Dust Evolution in Protoplanetary Disks. *Protostars and Planets VI*, pages 339–361, 2014. doi: 10.2458/azu_uapress_9780816531240-ch015. (Cited on pages 21 and 69.)

C. Thalmann, H. M. Schmid, A. Boccaletti, D. Mouillet, K. Dohlen, R. Roelfsema, M. Carbillet, D. Gisler, J.-L. Beuzit, M. Feldt, R. Gratton, F. Joos, C. U. Keller, J. Kragt, II, J. H. Pragt, P. Puget, F. Rigal, F. Snik, R. Waters, and F. Wildi. SPHERE ZIMPOL: overview and performance simulation. In *Society of Photo-Optical Instrumentation Engineers (SPIE) Conference Series*, volume 7014 of *Society of Photo-Optical Instrumentation Engineers (SPIE) Conference Series*, page 3, July 2008. doi: 10.1117/12.789158. (Cited on page 90.)

H. B. Throop and J. Bally. Tail-End Bondi-Hoyle Accretion in Young Star Clusters: Implications for Disks, Planets, and Stars. *AJ*, 135:2380–2397, June 2008. doi: 10.1088/0004-6256/135/6/2380. (Cited on pages 52 and 54.)

R. J. Trumpler. Absorption of Light in the Galactic System. *PASP*, 42:214, August 1930. doi: 10.1086/124039. (Cited on page 15.)

R. van Boekel, M. Min, C. Leinert, L. B. F. M. Waters, A. Richichi, O. Chesneau, C. Dominik, W. Jaffe, A. Dutrey, U. Graser, T. Henning, J. de Jong, R. Köhler, A. de Koter, B. Lopez, F. Malbet, S. Morel, F. Paresce, G. Perrin, T. Preibisch, F. Przygodda, M. Schöller, and M. Wittkowski. The building blocks of planets within the 'terrestrial' region of protoplanetary disks. *Nature*, 432:479–482, November 2004. doi: 10.1038/nature03088. (Cited on page 21.)

J. T. van Loon, M.-R. L. Cioni, A. A. Zijlstra, and C. Loup. An empirical formula for the mass-loss rates of dust-enshrouded red supergiants and oxygen-rich Asymptotic Giant Branch stars. *A&A*, 438:273–289, July 2005. doi: 10.1051/0004-6361:20042555. (Cited on page 22.)

E. Vazquez-Semadeni. Hierarchical Structure in Nearly Pressureless Flows as a Consequence of Self-similar Statistics. *ApJ*, 423:681, March 1994. doi: 10.1086/173847. (Cited on page 44.)

T. Verhoelst, N. van der Zypen, S. Hony, L. Decin, J. Cami, and K. Eriksson. The dust condensation sequence in red supergiant stars. *A&A*, 498:127–138, April 2009. doi: 10.1051/0004-6361/20079063. (Cited on pages xiii, 22, 23, and 24.)

A. Vigan, C. Moutou, M. Langlois, F. Allard, A. Boccaletti, M. Carbillet, D. Mouillet, and I. Smith. Photometric characterization of exoplanets using angular and spectral differential imaging. *MNRAS*, 407:71–82, September 2010. doi: 10.1111/j.1365-2966.2010.16916.x. (Cited on page 87.)

A. Villaume, C. Conroy, and B. D. Johnson. Circumstellar Dust around AGB Stars and Implications for Infrared Emission from Galaxies. *ApJ*, 806:82, June 2015. doi: 10.1088/0004-637X/806/1/82. (Cited on page 23.)

N. V. Voshchinnikov. In the Kitchen of Dust Modeling. In G. Videen and M. Kocifaj, editors, *Optics of Cosmic Dust*, page 1, 2002. (Cited on page 29.)

N. V. Voshchinnikov. Optics of cosmic dust I. *Astrophysics and Space Physics Reviews*, 12:1, 2004. (Cited on pages 5, 15, and 29.)

N. V. Voshchinnikov. Interstellar extinction and interstellar polarization: Old and new models. *J. Quant. Spec. Radiat. Transf.*, 113:2334–2350, December 2012. doi: 10.1016/j.jqsrt.2012.06.013. (Cited on pages 15 and 29.)

N. V. Voshchinnikov, F. J. Molster, and P. S. The. Circumstellar extinction of pre-main-sequence stars. *A&A*, 312:243–255, August 1996. (Cited on page 28.)

F. M. Walter, A. Brown, R. D. Mathieu, P. C. Myers, and F. J. Vrba. X-ray sources in regions of star formation. III - Naked T Tauri stars associated with the Taurus-Auriga complex. *AJ*, 96:297–325, July 1988. doi: 10.1086/114809. (Cited on page 20.)

L. B. F. M. Waters, F. J. Molster, T. de Jong, D. A. Beintema, C. Waelkens, A. C. A. Boogert, D. R. Boxhoorn, T. de Graauw, S. Drapatz, H. Feuchtgruber, R. Genzel, F. P. Helmich, A. M. Heras, R. Huygen, H. Izumiura, K. Justtanont, D. J. M. Kester, D. Kunze, F. Lahuis, H. J. G. L. M. Lamers, K. J. Leech, C. Loup, D. Lutz, P. W. Morris, S. D. Price, P. R. Roelfsema, A. Salama, S. G. Schaeidt, A. G. G. M. Tielens, N. R. Trams, E. A. Valentijn, B. Vandenbussche, M. E. van den Ancker, E. F. van Dishoeck, H. Van Winckel, P. R. Wesselius, and E. T. Young. Mineralogy of oxygen-rich dust shells. *A&A*, 315:L361–L364, November 1996. (Cited on page 23.)

E. Waxman and B. T. Draine. Dust Sublimation by Gamma-ray Bursts and Its Implications. *ApJ*, 537:796–802, July 2000. doi: 10.1086/309053. (Cited on page 25.)

J. C. Weingartner and B. T. Draine. Dust Grain-Size Distributions and Extinction in the Milky Way, Large Magellanic Cloud, and Small Magellanic Cloud. *ApJ*, 548: 296–309, February 2001. doi: 10.1086/318651. (Cited on pages 15, 29, and 69.)

R. Wesson, M. J. Barlow, M. Matsuura, and B. Ercolano. The timing and location of dust formation in the remnant of SN 1987A. *MNRAS*, 446:2089–2101, January 2015. doi: 10.1093/mnras/stu2250. (Cited on pages 23 and 96.)

B. A. Whitney. Monte Carlo radiative transfer. *Bulletin of the Astronomical Society of India*, 39:101–127, March 2011. (Cited on pages 11 and 12.)

B. A. Wilking, T. P. Greene, C. J. Lada, M. R. Meyer, and E. T. Young. IRAS observations of young stellar objects in the Corona Australis dark cloud. *ApJ*, 397:520–533, October 1992. doi: 10.1086/171808. (Cited on page 71.)

J. P. Williams and L. A. Cieza. Protoplanetary Disks and Their Evolution. *ARA&A*, 49:67–117, September 2011. doi: 10.1146/annurev-astro-081710-102548. (Cited on pages 59 and 60.)

A. N. Witt and K. D. Gordon. Multiple Scattering in Clumpy Media. I. Escape of Stellar Radiation from a Clumpy Scattering Environment. *ApJ*, 463:681, June 1996. doi: 10.1086/177282. (Cited on page 31.)

A. N. Witt and K. D. Gordon. Multiple Scattering in Clumpy Media. II. Galactic Environments. *ApJ*, 528:799–816, January 2000. doi: 10.1086/308197. (Cited on pages 28 and 31.)

M. Wittkowski, P. H. Hauschildt, B. Arroyo-Torres, and J. M. Marcaide. Fundamental properties and atmospheric structure of the red supergiant VY Canis Majoris based on VLTI/AMBER spectro-interferometry. *A&A*, 540:L12, April 2012. doi: 10.1051/0004-6361/201219126. (Cited on pages 84 and 95.)

P. Woitke. Too little radiation pressure on dust in the winds of oxygen-rich AGB stars. *A&A*, 460:L9–L12, December 2006. doi: 10.1051/0004-6361:20066322. (Cited on pages 11, 22, 83, and 84.)

S. Wolf. MC3D-3D continuum radiative transfer, Version 2. *Computer Physics Communications*, 150:99–115, February 2003. doi: 10.1016/S0010-4655(02)00675-6. (Cited on page 67.)

S. Wolf, O. Fischer, and W. Pfau. Radiative transfer in the clumpy environment of young stellar objects. *A&A*, 340:103–116, December 1998. (Cited on pages 28, 31, 36, 37, and 41.)

S. Wolf, T. Henning, and B. Stecklum. Multidimensional self-consistent radiative transfer simulations based on the Monte-Carlo method. *A&A*, 349:839–850, September 1999. (Cited on pages 11 and 67.)

M. G. Wolfire, C. F. McKee, D. Hollenbach, and A. G. G. M. Tielens. Neutral Atomic Phases of the Interstellar Medium in the Galaxy. *ApJ*, 587:278–311, April 2003. doi: 10.1086/368016. (Cited on page 45.)

S. Xu, S. Ertel, Z. Wahhaj, J. Milli, P. Scicluna, and G. H.-M. Bertrang. An Extreme-AO Search for Giant Planets around a White Dwarf –VLT/SPHERE performance on a faint target GD 50. *ArXiv e-prints*, June 2015. (Cited on page 80.)

F. Yusef-Zadeh, M. Morris, and R. L. White. Bipolar reflection nebulae - Monte Carlo simulations. *ApJ*, 278:186–194, March 1984. doi: 10.1086/161780. (Cited on pages 14 and 35.)

T. Zafar, D. Watson, J. P. U. Fynbo, D. Malesani, P. Jakobsson, and A. de Ugarte Postigo. The extinction curves of star-forming regions from z = 0.1 to 6.7 using GRB afterglow spectroscopy. *A&A*, 532:A143, August 2011. doi: 10.1051/0004-6361/201116663. (Cited on page 47.)

B. Zhang, M. J. Reid, K. M. Menten, and X. W. Zheng. Distance and Kinematics of the Red Hypergiant VY CMa: Very Long Baseline Array and Very Large Array Astrometry. *ApJ*, 744:23, January 2012. doi: 10.1088/0004-637X/744/1/23. (Cited on page 84.)

H. Zinnecker. Binary statistics and star formation. *Ap&SS*, 99:41–70, February 1984. doi: 10.1007/BF00650229. (Cited on page 59.)

V. G. Zubko, V. Mennella, L. Colangeli, and E. Bussoletti. Optical constants of cosmic carbon analogue grains - I. Simulation of clustering by a modified continuous distribution of ellipsoids. *MNRAS*, 282:1321–1329, October 1996. (Cited on page 34.)

ACKNOWLEDGMENTS

Firstly, I wish to thank both my supervisors, Sebastian Wolf and Ralf Siebenmorgen, for their insights, support and patience for the duration of this work. Needless to say, they made this all possible.

Furthermore, I would also like to thank ...

... Kristin Fischer, for being there, and for proof–reading;

... Leonardo Testi, for unstinting advice, help, and even supervision, when he already had enough students of his own;

... the rest of the OoPS! team, Giovanni and Jim, for turning a crazy idea into reality;

... everyone at accretion coffee, for welcoming a theorist;

... Eric Emsellem, for helping to make the *Office for Science, Garching* as welcoming as possible;

... Frank Heymann, for easing me in to the *very* basics of MCRT;

... Tim Davis, for help with everything from career choices to referee reports;

... the ESO boardgamers, for occasionally letting me win;

... Markus Kasper, for answering stupid questions about SPHERE;

... Gesa Bertrang, for sharing the pain;

... Florian Ober, for helping to find (and sometimes even fix) bugs;

... the NEAT team, for making sure there's always a *productive* distraction;

... Pippa and Felix (may he rest in peace), for purring at all the right times;

... Manuel Jung, for helping to translate the abstract into German;

... Jan-Torge Schindler, for proof–reading and statistical discussions;

... and a multitude of others, including but not limited to: Joris Blommaert, Robert Brauer, Rober Brunngraber, Grainne Costigan, Steve Ertel, Stephan Geier, Neale Gibson, Josef Hron, Izaskun Jiminez-Serra, Uli Kauefl, Ciska Kemper, Florian Kirchschager, Rainer Koehler, Endrik Kruegel, Carlo Manara, Antonella Natta, Thorsten Ratzka, Jan-Phillipp Ruge, Nikolai Voshchinnikov, Siyi Xu, and, of course, my family.

DECLARATION

I hereby declare that the present doctoral thesis is, with the exception of my supervisors' guidance, in content and design my own work, unless otherwise attributed in the text,

that this work has not been submitted, either in whole or in part, to any doctoral examination proceedure elsewhere,

that parts of this work are published in Scicluna et al., (2014), or will be published or submitted for publication in Scicluna & Siebenmorgen (2015, accepted), Scicluna et al., (2015, submitted), and Scicluna et al., (2015, in prep.),

and that this work has been prepared under the Rules of Good Scientific Practice of the German Research Foundation.

Kiel, 2015

Peter Scicluna